iScience

CellPress
OPEN ACCESS

Article

cGAS and DDX41-STING mediated intrinsic immunity spreads intercellularly to promote neuroinflammation in SOD1 ALS model

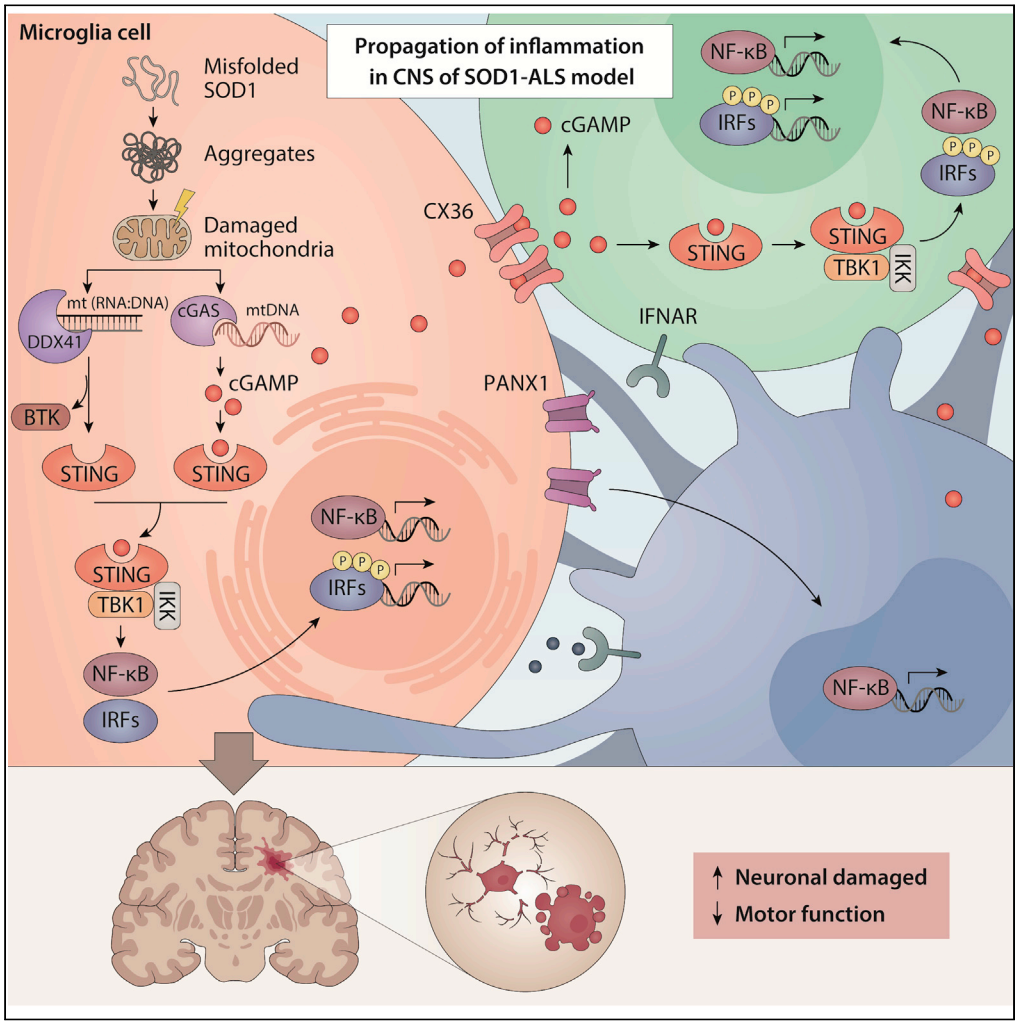

Hong Yien Tan, Yean Kong Yong, Yuan Chao Xue, Huitao Liu, Tomomi Furihata, Esaki Muthu Shankar, Chen Seng Ng

chenseng.ng@xmu.edu.my

Highlights

Constitutive basal activation of IFN-I was found in the SOD1-ALS animal model

SOD1-ALS damaged mitochondria to release mtDNA and RNA:DNA to activate the STING-pathway

Blocking cGAS and STING diminishes neurodegeneration *in vivo* in the SOD1-ALS model

Connexin and pannexin channels are required to propagate neuroinflammation in SOD1-ALS

Tan et al., iScience *25*, 104404
June 17, 2022 © 2022
https://doi.org/10.1016/j.isci.2022.104404

iScience

CellPress
OPEN ACCESS

Article

cGAS and DDX41-STING mediated intrinsic immunity spreads intercellularly to promote neuroinflammation in SOD1 ALS model

Hong Yien Tan,[1,2] Yean Kong Yong,[1] Yuan Chao Xue,[3,4,5] Huitao Liu,[3,5] Tomomi Furihata,[6] Esaki Muthu Shankar,[7] and Chen Seng Ng[8,9,*]

SUMMARY

Neuroinflammation exacerbates the progression of SOD1-driven amyotrophic lateral sclerosis (ALS), although the underlying mechanisms remain largely unknown. Herein, we demonstrate that misfolded SOD1 ($SOD1^{Mut}$)-causing ALS results in mitochondrial damage, thus triggering the release of mtDNA and an RNA:DNA hybrid into the cytosol in an mPTP-independent manner to activate IRF3- and IFNAR-dependent type I interferon (IFN-I) and interferon-stimulating genes. The neuronal hyper-IFN-I and pro-inflammatory responses triggered in ALS-$SOD1^{Mut}$ were sufficiently robust to cause a strong physiological outcome *in vitro* and *in vivo*. cGAS/DDX41-STING-signaling is amplified in bystander cells through inter-neuronal gap junctions. Our results highlight the importance of a common DNA-sensing pathway between SOD1 and TDP-43 in influencing the progression of ALS.

INTRODUCTION

Amyotrophic lateral sclerosis (ALS) is a devastating, rapidly progressing paralytic neurodegenerative disease (ND) characterized by severe upper and lower motor neuronal (MN) loss in the brainstem and spinal cord of humans. ALS has a prevalence of 5.4 per 100,000 individuals (Chiò et al., 2013). In certain regions, especially Guam, the Kii Peninsula in Japan, and Guinea, the prevalence is estimated to be ~50–100 times higher than the rest of the world (Pablo et al., 2009). Typically, older adults and men represent a high-risk group for being diagnosed with ALS (Wijesekera and Leigh, 2009). Patients will succumb to the disease within 2–5 years of clinical onset because of the development of severe muscular atrophy and paralysis. The hallmark of the disease is the loss of muscle control that occurs when signal transduction between the brain and muscles lacks coordination leading to eventual loss of voluntary movements, muscle fasciculation, and skeletal muscle atrophy. Subsequently, paralysis of voluntary muscles occurs slowly culminating in death owing to respiratory failure. Unlike for other diseases, there is a paucity of universal consensus on the parameters that trigger the onset of ALS in humans or in preclinical investigations employing ALS mice models. Furthermore, specific stimuli always lead to the same endpoint in this disease. Several genes and pathophysiological pathways play a paramount role in ALS disease pathophysiology. At the same time, there is an ongoing debate about whether the pathological, clinical, and phenotypic heterogeneity observed in ALS should be treated as a single entity or if it requires categorization based on specific molecular signals that are only partially responsible because of their complexity (Turner and Swash, 2015). ALS has become a multisystemic condition with diverse clinical manifestations and multiple etiologies responsible for its pathogenesis. Conversely, specific etiological factors such as viral infections, autoimmune responses, oxidative stress, glutamate excitotoxicity, defective axonal transport, glial cell impairment, impaired DNA and RNA metabolism, metabolic impairment, heavy metal toxicity, apoptosis, proteinopathies, and proteome homeostasis have been implicated in the degenerative processes (Hardiman et al., 2017; Saberi et al., 2015; Taylor et al., 2016). Available evidence suggests that ALS is a multi-step disease with different phases that vary across patient groups, although in individuals with underlying genetic abnormalities the number of stages in the disease course are fewer than those without (Chiò et al., 2018; Vucic et al., 2019).

In general, over 95% of all ALS patients are classified as sporadic, defined as having no known familial history of the disease. The remaining 5% of the patients are classified as familial and typically appear to

[1]Laboratory Centre, Xiamen University Malaysia, Sepang, Selangor, Malaysia

[2]School of Traditional Chinese Medicine, Xiamen University Malaysia, Sepang, Selangor, Malaysia

[3]Centre for Heart Lung Innovation, St Paul's Hospital, University of British Columbia, Vancouver, BC, Canada

[4]Department of Pathology and Laboratory of Medicine, Faculty of Medicine, University of British Columbia, Vancouver, BC, Canada

[5]Department of Medicine, Faculty of Medicine, University of British Columbia, Vancouver, BC, Canada

[6]Laboratory of Clinical Pharmacy and Experimental Therapeutics, School of Pharmacy, Tokyo University of Pharmacy and Life Sciences, Tokyo, Japan

[7]Infection Biology, Department of Life Sciences, Central University of Tamil Nadu, Thiruvarur, India

[8]China-ASEAN College of Marine Sciences, Xiamen University Malaysia, Sepang, Selangor, Malaysia

[9]Lead contact

*Correspondence: chenseng.ng@xmu.edu.my

https://doi.org/10.1016/j.isci.2022.104404

have inherited the trait in an autosomal dominant fashion. Mutations in the *SOD1* gene, encoding superoxide dismutase 1, were the first to be identified as genetic factors associated with aggressive ALS progression (Bruijn et al., 1997, 1998; Rosen et al., 1993). *SOD1* mutations represent the second most common genetic cause of ALS to date, with approximately 20% of familial cases, and with more than 100 different reported gene mutations (Chen et al., 2013; Mejzini et al., 2019). Elegant studies using transgenic rodent models carrying mutant forms of *SOD1* have shown that non-neuronal cells also play a crucial role in the development of ALS, contributing to MN death by non-cell-autonomous mechanisms. Similarly, in *in vitro* studies murine SOD1 mutant astrocytes and microglia, as well as human astrocytes from sporadic and familial ALS patients can induce MN death. This suggests that ALS is a deadly convergence of insults developed across multiple cell types and stages that culminated in neuromuscular failure. However, the precise mechanisms through which each neuronal cell type contributes to ALS disease progression remains ambiguous.

One of the most striking hallmarks of misfolded SOD1 (SOD1 mutants, $SOD1^{Mut}$)-driven ALS shared by familial and sporadic patients, as well as by rodent models, is neuroinflammation, characterized by microglia and astrocyte activation, T lymphocyte infiltration, and excessive production of pro-inflammatory cytokines and chemokines (Endo et al., 2016; Ringer et al., 2017; Yoshihara et al., 2002). These phenomena have been demonstrated in association with MN degeneration in both animal and human tissues, even during the pre-symptomatic phase of $SOD1^{Mut}$-ALS. Accumulating evidence from preclinical work has suggested that immune cells either exert deleterious or protective effects on MN survival depending on the state of activation and disease stage; however, the underlying mechanisms are far from being fully elucidated.

Microglia are the most prominent immune cells within the central nervous system (CNS) and represent a specialized subset of macrophages accounting for ~10–15% of the cells found in the brain. These cells survey the surrounding environment and respond to infections, abnormal or misfolded proteins, antigen complexes, and "danger signals"—more commonly known as alarmins or "danger-associated molecular patterns" produced by apoptotic tissues within the CNS. In response to these stimuli, "resting" microglia will become "activated" and produce reactive oxygen species, cytokines, and other toxic molecules, leading to the acceleration of neuronal dysfunction and death (Hanisch and Kettenmann, 2007; Liao et al., 2012). Previous studies have shown that activated microglia are widely present in the CNS of ALS patients, with a significant correlation between the intensity of microglia activation in the brain cortex region and the severity of clinico-neurological impairment (Turner et al., 2004). Studies using $SOD1^{Mut}$ transgenic mice further revealed that the replacement of $SOD1^{Mut}$ microglia with wild-type (WT) microglia through transplantation leads to neuroprotection by delaying neuronal cell death and improving the median lifespan of neurons (Beers et al., 2006; Boillée et al., 2006). Moreover, neutralizing microglia-derived superoxide also significantly increases the lifespan of $SOD1^{Mut}$ mice (Harraz et al., 2008). $SOD1^{Mut}$ astrocytes, a subtype of glial cells, also exhibit increased expression of many pro-inflammatory and chemokine genes, accelerating MN death through necroptosis by enhancing microglia activation, supporting the likely role of astrocytes in regulating microglia activation (Yamanaka et al., 2008). Similarly, transplantation of WT to replace $SOD1^{Mut}$ astrocytes appears to attenuate astrocyte-mediated toxicity and neuronal loss (Papadeas et al., 2011). Hence, the role of astrocytes should not be undervalued. Despite all these efforts, genetic approaches to eliminate specific inflammatory genes in ALS murine models have largely remained unsuccessful, highlighting the complexity of neuroinflammation in ALS. For these reasons, a successful therapeutic approach is likely to derive from a better understanding of the intricate molecular mechanisms driving the inflammatory response throughout the course of the disease.

Currently, riluzole and edaravone are the only approved drugs available to treat ALS, even though the drugs only confer modest benefits to patients. Because the mechanism of neuroinflammation in SOD1-causing ALS remains unclear, we sought to revisit this topic and investigate the underlying rationale of different neuronal and non-neuronal cells that mediate MN death in ALS, with a primary focus on microglia. In the present study, we investigated two extensively characterized *SOD1* mutations, i.e., G93A and G85R; the former inducing impaired in zinc-binding loops and associated with a more aggressive disease progression; whereas the latter is characterized by a normal zinc-binding loop, but greater susceptibility to disulfide and metal chelating agents, associated with a slower disease progression in mice (Tiwari et al., 2005; Yamashita and Ando, 2015). Here, we demonstrated that $SOD1^{Mut}$ leads to constitutive basal activation of type I interferon (IFN-I) and interferon-stimulating genes (ISGs), which in turn amplify other

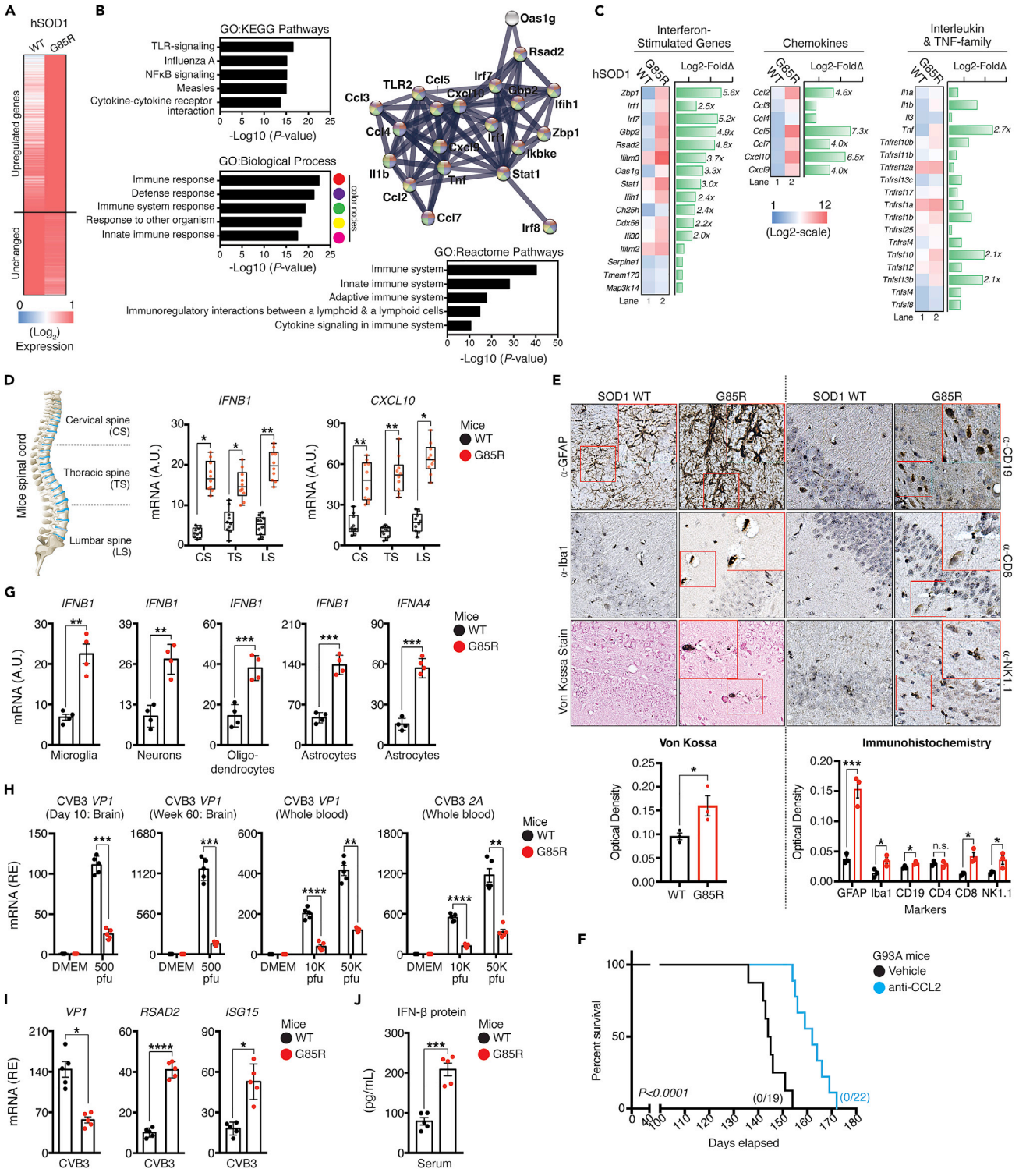

Figure 1. Basal activation of pro-inflammatory cytokines, chemokines, and IFN-I response in the SOD1-G85R *in vivo* model

(A) Whole brain tissues were isolated from WT and G85R mice at day-10 after birth. Purified whole RNA was subjected to NanoString multiplex gene analysis using the murine neuroinflammation panel that consists of 770 genes. Heat-map representation of differentially expressed genes with upregulated related genes (fold-change >2.0 as the cut-off threshold) by G85R expressed as fold changes relative to WT controls.

(B) The upregulated genes from (A) were subjected to unbiased protein network and enrichment analysis via the STRING-CytoScape.

(C) Representative heatmap of upregulated immune mediator profile (fold-change ≥2.0) in G85R mice after clustering into their respective families.

Figure 1. *Continued*

(D) Spinal cord from WT or G85R mouse models were isolated and dissected into three sections as depicted (*left*). RNA from each section were harvested and subjected to analysis of the indicated mRNA (*right*).

(E) Von Kossa and immunohistochemistry staining of brain tissue from WT or G85R mice with the indicated antibodies. Quantification of staining was performed via optical density determination.

(F) Kaplan-Meier survival plots of age-matched G93A mice challenged either with vehicle or MCP-1 neutralizing antibody (500 μg/week). Number of mice that survived at the endpoint are indicated.

(G) Primary cells were isolated from the brain of WT or G85R mice at day-10 after birth through immunopanning procedures. RNA was purified and subjected to RT-qPCR analysis.

(H) Newborn WT or G85R mice were intracranially injected with vehicle (DMEM), 500, 10,000, or 50,000 plaque-forming units (pfus) of CVB3 at day-8. The brain and the entire blood was harvested at two time-points (Day 10, and Week 60), respectively. *Vp1* and *2A* mRNA were quantified via RT-qPCR.

(I) C20 cells were first pre-treated with serum harvested from WT or G85R mice, followed by infection with CVB3 (MOI = 1.0). *Vp1*, *Rsad2*, and *Isg15* mRNA were measured via RT-qPCR.

(J) Serum collected from endpoint WT or G85R mice (week-60) were subjected to ELISA analysis for IFN-β protein. All RT-qPCR assays are normalized to β-actin. Data represent the mean of at least three independent experiments with n = 3 biological replicates (mean ± SEM). Number of dots = number of mice/biological replicates. *p< 0.05, **p< 0.01, ***p< 0.001, ****p< 0.0001; (D, E, and G–J: unpaired Student's *t* test; F: Log rank Mantel-Cox test). A.U. = arbitrary units. See also Figure S1.

pro-inflammatory signaling cascades to promote neuroinflammation and neuronal death. These processes are achieved by damaging mitochondria and the release of mitochondria DNA (mtDNA) and mt(RNA:DNA) hybrid structures into the cytoplasm, to activate cGAS/DDX41-STING pathway for IFN-I induction. Furthermore, we found that neuronal connexin 36 and pannexin 1 were critical for extending the immune responses to bystander cells. Together, these data indicate that activation of the cGAS/DDX41-STING pathway in microglia is a novel molecular mechanism underlying MN death in SOD1-driven ALS. Moreover, our findings also identified a new therapeutic regimen suggesting a strategy for early intervention against the rapid progression of ALS and possibly other NDs in which stimulator of interferon genes (STING) activation could also play a likely role.

RESULTS

Prevalence of IFN-I, chemokine, and pro-inflammatory cytokine activation in ALS-SOD1 models

To better characterize the neuroinflammatory state in ALS-SOD1-relevant models, we pursued an unbiased approach to identify a transcriptomic signature associated with *SOD1*-mutations. We first isolated the whole brain and performed genome-wide transcriptomic profiling on tissue samples obtained during the disease progression in a murine model that carried the G85R mutation. In the absence of any treatment, the unsupervised transcriptomic analysis revealed that, of the 770 annotated Refseq genes, ~73 genes exhibited markedly (mean FC≥2-fold) increased expression, and ~697 genes remained unchanged in SOD1-G85R whole brain samples when compared to the WT counterpart (Figure 1A). We subsequently conducted a systematic unbiased analysis to characterize the functional protein-protein correlation network. To this end, we performed gene ontology annotation of the modules with the STRING package with the addition of terms from the Kyoto Encyclopedia of Genes and Genomes database and the Geneset Enrichment Analysis databases evaluated using the Fisher exact test (Benjamini–Hochberg false discovery rate [FDR] < 0.05). Using this high-confidence network as baseline, we identified significantly enriched in genes encoding products associated with Toll-like receptors, NF-κB-associated signaling, and host defense responses, which showed the highest enrichment among the upregulated genes (Figures 1B and S1A), with ~22% (16 of 73) genes corresponding to ISGs, including *Irf1, Irf7, Rsad2, Ifih1*, *Ddx58*, *Gbp2*, *Oas1*, *Stat1,* and *Ifits*. Further, we also detected significantly elevated expression of the pro-inflammatory cytokine gene, *Tnf*, as well as a panel of well-known chemokines genes, with some of them, also specifically induced by IFN-I, including *Ccl2, Ccl5, Ccl7, Cxcl9,* and *Cxcl10* (Figure 1C). Furthermore, we also observed similar results after re-performing an unbiased analysis using the public transcriptome sequencing dataset of microglia isolated from another well-known ALS murine model SOD1-G93A (Krasemann et al., 2017).

Next, we sought to determine whether the hyper-expression of inflammation-associated genes can be recapitulated in other organs *in vivo*. We isolated the spinal cord, a region crucial for the transmission of nerve signals from the motor cortex to the whole body, and further dissected it into three sections: namely cervical spine (CS), thoracic spine (TS), and lumbar spine (LS). We then examined the basal mRNA expression of *Ifnb1*, *Tnf, Il6, Il1b,* and *Cxcl10* for each section by RT-qPCR, and found a significantly increased

expression of all genes (Figures 1D and S1B). We also purified the RNA extracted from the spleen, liver, and lungs of both WT and SOD1-G85R mice and measured the gene expression. Our analysis identified elevated expression of the genes in all examined organs, including *Ccl5*, and *Rsad2*, a putative chemokine and ISGs (Figures S1C–S1E). Von Kossa staining showed a marked increase of calcium deposition within the brain, which is a sign of persistent inflammation. Immunohistochemical examination further revealed a significant increase in signal intensity of GFAP by ~4-fold ($p < 0.01$), infiltration of immune cells in the brain tissues of SOD1-G85R, with a modest but statistically significant number of microglia ($Iba1^+$), NK cells ($NK1.1^+$), T-lymphocytes ($CD8^+$), and B-lymphocytes ($CD19^+$) (Figure 1E), indicating that neuronal astrogliosis and microgliosis are increased in G85R mice compared to age-matched controls. Chemokines genes were shown to play crucial role in the development of several neuroinflammatory diseases, including but not limited to tau pathology, and brain abscesses (Kielian et al., 2001; Semple et al., 2010). Overall, CCL/CXCL-family genes accounted for the largest mean fold-change in our NanoString profiling study; thus, we sought to investigate whether the constitutive activation of basal chemokines could contribute to SOD1-related pathologies. SOD1-G93A mice, another well-characterized transgenic rodent of ALS (Van Den Bosch, 2011),] received either vehicle, or anti-MCP-1 neutralizing antibody to abrogate the function of the critical chemoattractant molecule: MCP-1 (encoded by the *Ccl2* gene). By comparing the viability of the anti-MCP-1 with vehicle-treated mutant mice, the abrogated functions of MCP-1 offered significant protection and prolonged survival (Figure 1F). Collectively, our results indicated that the IFN-I pathway is activated concurrently with the ongoing neuroinflammation to promote the pathogenesis in the ALS-SOD1-mutant model.

IFN-I plays a crucial role in host immune responses as a pleiotropic modulator critical for determining the cellular susceptibility to viral infections, cellular growth, and immune cells activation. In the quiescent state, IFN-I is constitutively produced at low levels and exerts profound physiological effects on homeostasis through coordinated tonic signaling. Accumulating evidence suggests that exaggerated production of IFN-I could have a profound negative impact on the host (Stetson et al., 2008; Stetson and Medzhitov, 2006). Furthermore, *Ccl2* has previously been reported as an interferon-α/β Receptor (IFNAR)-dependent gene. Limited *Ccl2* expression, and thus, reduced production of MCP-1 protein was observed in IFNAR-deficient macrophages and tissue homogenates *in vivo* as measured using enzyme-linked immunosorbent assay (ELISA) (Lehmann et al., 2016; Palomino-Segura et al., 2019). These led us to hypothesize that IFN-I mis-regulation is the key to promoting the neuroinflammatory phenotype in the ALS-SOD1-G85R model. To test hypothesis, we isolated and cultured several key primary neuronal and non-neuronal cells from SOD1-G85R mice through immunopanning procedures. The identity of each respective cell type was verified via the mRNA expression of well-known markers (Figure S2). As shown in Figure 1G, both *Ifnb1*, and *Ifna4* mRNA expression were markedly induced at baseline in all tested primary cells, including murine microglia, motor neurons, oligodendrocytes, and astrocytes. Comparable results were obtained for other chemokines and pro-inflammatory genes, including *Cxcl10, Tnf,* and *Il6* (Figure S1F). Interestingly, we also detected a significant upregulation of microglia-specific ISGs, including *Axls*, *B2m*, and *Aif1* in SOD1-G85R primary microglia (Figure S1G), which defined the microglial neurodegenerative phenotype (MGnD) gene signature. These observations prompted us to confirm the presence of IFN-I within the animal bloodstream using two bioassays. First, we assayed viral replication *in vivo* by infecting mice with coxsackievirus-B3 (CVB3), a neurotropic RNA virus via bilateral intracerebroventricular stereotaxic injection. The results indicated that there was a substantially decreased level of CVB3 replication (as indicated by *Vp1* and *2A* mRNA) within the whole brain and blood from day 10 and at week 60 when SOD1-G85R mice were compared to WT mice (Figure 1H). Second, we assayed viral replication and gene expression when serum-treated cells were infected with CVB3. We observed that SIM-A9, a murine brain-resident macrophage pre-treated with SOD1-G85R serum, displayed remarkably increased resistance to CVB3 infection. RT-qPCR analysis also indicated that there was a significant decrease in CVB3 replication (*Vp1*), followed by a substantial increase in the expression of ISGs (*Rsad2* and *Isg15*) in human microglia (C20) that were pre-conditioned with serum from SOD1-G85R but not from serum from WT animals (Figure 1I). Quantitative ELISA further confirmed that the basal proteins levels of IFN-β were significantly elevated in the blood serum of SOD1-G85R-mutated model animals (Figure 1J). Aberrant expression of IFN-I is the cause of several autoimmune disorders (Crowl et al., 2017; Lee-Kirsch, 2017). In our assays, both ALS-$SOD1^{Mut}$-mice models further displayed a significant increase in total serum immunoglobulin or in anti-nuclear antibody levels, two diagnostic markers of autoimmune diseases (Figure S1H). Taken together, these results indicate that the ALS-$SOD1^{Mut}$-*in vivo* model produces substantially elevated levels of biologically active IFN-I, which may contribute to the development of an autoimmune-like phenotype in ALS.

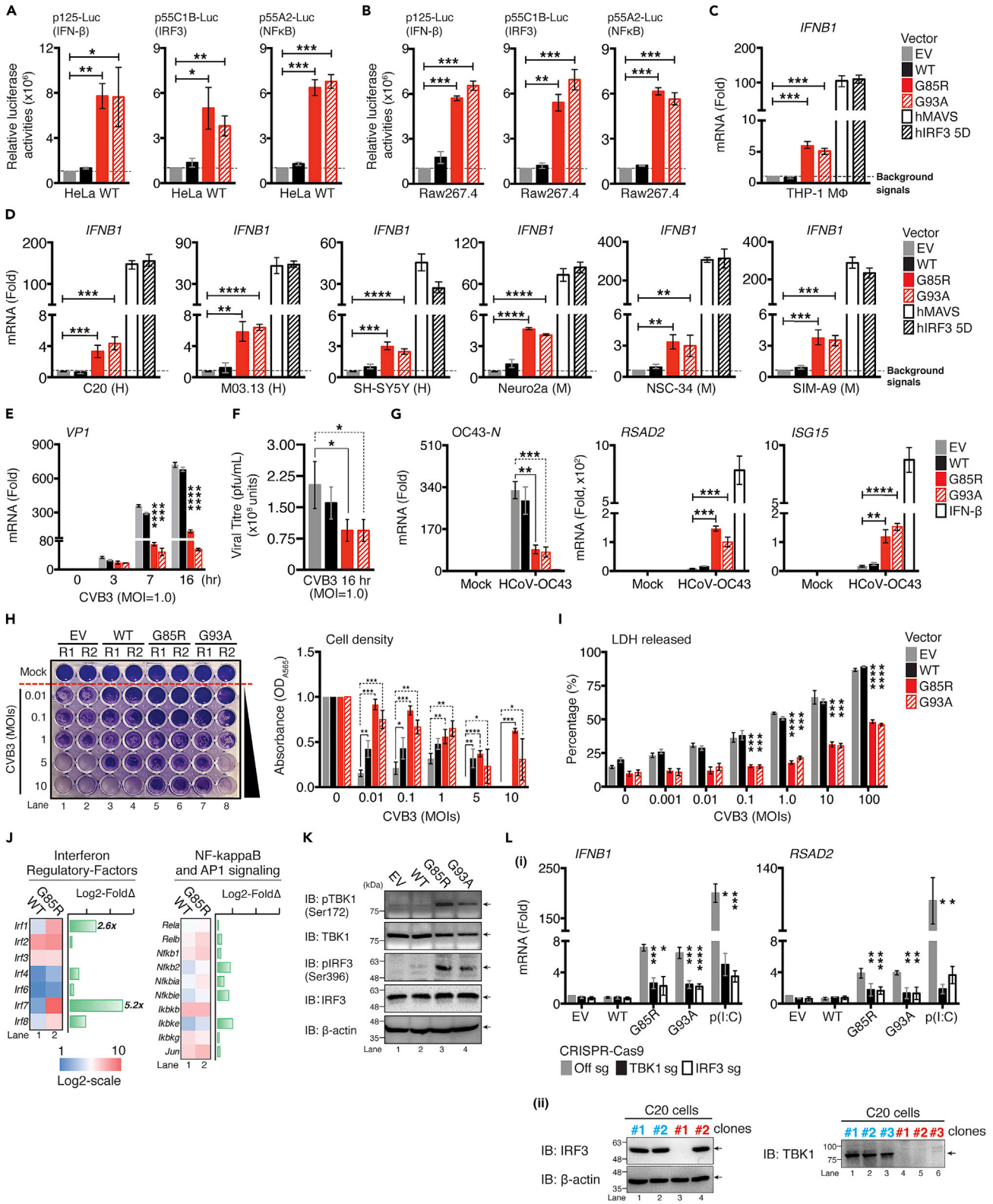

Figure 2. Overexpression of ALS SOD1-mutants activate IFN-I response *in vitro* and confer resistance to viral infection

(A and B) HeLa WT or murine RAW264.7 cells expressing indicated reporter were co-transfected with plasmids encoding EGFP-, human SOD1-WT,-G85R, or-G93A mutants. 36 h after transfection, cell lysates were collected and analyzed for luciferase activity.

Figure 2. *Continued*

(C) THP-1-derived MΦ cells were transfected with 0.01 μg of indicated plasmids for 36 h, indicated mRNA levels were assessed via RT-qPCR.

(D) Similar conditions in panel (C) were performed in an indicated neuronal cell lineage (H: Human; M: Murine).

(E) C20 cells were transfected with indicated plasmids, followed by CVB3 (MOI = 1.0) infection at indicated time-points. CVB3 *Vp1* mRNA was measured via RT-qPCR.

(F) Supernatant from panel E were collected and subjected to the plaque assay to measure the release of viral particles.

(G) Newly seeded C20 cells were pre-treated with supernatant collected from C20 cells expressing the indicated plasmids for 24 h. Cells were then infected with HCoV-OC43 (MOI = 1.0) for 72 h. In a parallel experiment, C20 cells were treated with 100 ng/mL of IFN-β proteins for 24 h as positive control. HCoV-OC43 nucleocapsid RNA, *Isg15*, and *Rsad2* mRNAs were measured using RT-qPCR.

(H and I) C20 cells transfected with the indicated plasmid were infected with the indicated MOI of CVB3 and assessed 24 h later for cell viability with crystal violet staining and the LDH released assay.

(J) NanoString analysis for gene expression of indicated family of transcription factors comparing whole brain of WT and SOD1-G85R mice (n = 3 for each genotype).

(K) Immunoblot analysis of phosphorylated or total TBK1 and IRF3 or β-actin in C20 cells after transfection with the indicated plasmids.

(L) (1) TBK1, or IRF3-deficient C20 cells using CRISPR/Cas9 system expressing the indicated plasmids for 36 h. *Ifnb1* and *Rsad2* mRNA measured via RT-qPCR. Transfected poly(I:C) [p(I:C), 0.1 μg] served as positive control. (2) Knockout efficiency of the positive clones was confirmed by western blotting. Clone#1 of two lineage were selected for subsequent studies. Data represent the mean of three independent experiments with n = 3 biological replicates (mean ± SEM). *p< 0.05, **p< 0.01, ***p< 0.001, ****p< 0.0001; (A–I, and L: two-tailed, unpaired Student's *t* test). See also Figure S3.

Cell-type specific involvement in ALS-SOD1^{Mut}-mediated IFN-I response

The basal gene expression in the *in vivo* model (Figure 1) is primed and subject to numerous feedforward and feedback loops; thus, we sought to address the potential cell-type specificity of hyper-responsive IFN-I associated gene expression in SOD1-driven ALS pathogenesis. We analyzed the activation of the IFN-I signaling pathway and its associated changes in gene expression upon SOD1^{Mut} expression in various cell types. Both HeLa and HEK293T cells, the two most widely used human somatic cell lines in biological research, were co-transfected with either (1) p125-luc, a reporter plasmid containing the full-length IFN-β promoter; (2) p55C1B-luc, a reporter plasmid containing repetitive activated IRF3-binding sites of the IFN-β gene promoter; or (3) p55A2-luc, an NF-κB driven reporter plasmid comprising three repeats of the PRDII domain of the IFN-β promoter, and each of the SOD1^{Mut} plasmids. Approximately 36 h later, the cells were assayed for luciferase activity. The results indicated that the relative luciferase activity from all three reporter plasmids in both SOD1^{Mut}-transfected cell lysates were robustly induced (≥2-fold) as compared to both empty vector (EV) and SOD1-WT cells (Figure 2A). Further analysis indicated that the SOD1^{Mut} activated all three promoter activities in a dose-dependent manner (Figure S3A). We also found that both SOD1^{Mut} upregulated the expression of *Ifnb1* mRNA at 12 h post-transfection, with its expression remaining persistently elevated and continued to peak and plateau over a 24-h period but started to decrease after 48 h (Figure S3B). Strikingly, none of the above observations were reproducible in HEK293T cells (Figure S3C).

Next, we pursued the same question in a more physiologically relevant cellular context. The brain contains two sets of monocyte-macrophage cells—blood-borne monocytes-derived macrophages (BBMΦ), and brain-resident macrophages (microglia). BBMΦ, primarily located within the perivascular spaces, the leptomeninges, and the choroid plexus, serve as the main antigen-presenting cells of the CNS and have recently emerged as an essential component of the disease-associated microenvironment in the brain and have been described as playing critical roles in the progression of ND. We tested whether the observation-mentioned for HeLa cells could be recapitulated in BBMΦ by co-transfecting each reporter with indicated SOD1^{Mut} constructs into RAW264.7, a murine BBMΦ-lineage cell line. As shown in Figure 2B, all three reporters were robustly activated in RAW264.7 expressing either of the SOD1^{Mut} proteins. Moreover, ectopic expression of G85R, G93A, MAVS, or IRF3 5D (a constitutively active phosphomimetic IRF3 mutant) also resulted in robust induction of *Ifnb1* mRNA not only in phorbol-12-myristate-13-acetate (PMA)-differentiated THP-1 macrophages (a human monocytic leukemia cell line) (Figure 2C), but also in several other popular *in vitro* neuronal cell lines. These include SIM-A9 and C20 (murine and human microglia) (Garcia-Mesa et al., 2017), M03.13 (human oligodendrocytes) (McLaurin et al., 1995), HASTR/ci35 (human astrocytes) (Furihata et al., 2016; Kitamura et al., 2018), Neuro2a and SH-SY5Y (murine and human neuroblastoma), and NSC-34 (murine motor neuron-like cells) (Figures 2D and S3D). These results collectively indicate that ALS-SOD1^{Mut} could robustly activate the IFN-I pathway in HeLa cells and in most of the key neuronal populations within CNS in a cell-type-specific manner.

To evaluate whether the hyper-production of cytokines by ALS-SOD1^{Mut} is mutation specific, we further characterized seven other ALS-associated SOD1 mutations (i.e., V190G, A4V, G37R, H46R, V148I, E100G,

and G127X) in both HEK293T cells and microglia. The results indicated that exogenous expression of all seven SOD1^{Mut} also robustly activated the expression of *Ifnb1*, *Tnf*, *Il6*, and *Ccl5* in microglia as compared to both EV and WT cells. No induction in gene expression was observed when using the HEK293T cell line as the model, even when they were transfected with dosage-increasing levels of SOD1^{Mut} (Figures S3E–S3G). These results further confirmed that the observed neuronal hyper-inflammatory response is a highly conserved feature across most, if not all ALS-associated SOD1^{Mut}.

Albeit statistically significant, the basal induction of IFN-I by SOD1^{Mut} was small (<10-fold), we questioned whether these observations could truly induce any physiological consequences to the host. To evaluate this, microglia were infected with CVB3, and the intracellular viral replication was measured through RT-qPCR. Ectopic expression of indicated SOD1^{Mut} significantly suppressed CVB3 replication across all three post-infection time-points (Figure 2E). Quantification of virus particles in the supernatant collected at the 16 h post-infection time-point from Figure 2E also produced similar outcomes (Figure 2F). To demonstrate that the viral resistance in SOD1^{Mut} expressing cells was due to IFN-I, supernatants from microglia expressing EV, WT, or SOD1^{Mut} were transferred to cultures of newly seeded microglia. After 24 h, the supernatant was removed and cells were infected with human *beta*-coronavirus strain OC43 (HCoV-OC43), another neurotropic RNA virus that is associated with meningitis and acute disseminated encephalomyelitis (Cheng et al., 2020; Jacomy et al., 2006; Kasereka and Hawkes, 2021; Morfopoulou et al., 2016; Nilsson et al., 2020). The conditioned media from SOD1^{Mut} but not EV and WT expressing cells strongly induced the expression of ISGs, and conferred resistance to HCoV-OC43 infection (Figure 2G). Our results demonstrated that the ISG-inducing capacity and the resistance to HCoV-OC43 are mediated by the elevated production of biologically active IFN-I proteins in the supernatant of SOD1^{Mut} expressing cells. To further substantiate this, EV, WT, or specific SOD1^{Mut} microglia were infected with CVB3 at various multiplicities of infection (MOIs). By evaluating cell death [percentage of lactate dehydrohenase (LDH) released and crystal violet staining), we observed that SOD1^{Mut} overexpressing cells significantly reduced the susceptibility of cells to CVB3 infection in all MOIs tested (Figures 2H and 2I). Taken together, these results demonstrate that neuronal hyper-IFN-I and pro-inflammatory responses triggered by ALS-SOD1^{Mut} are sufficiently robust to cause strong physiological implications, for instance, broad-spectrum resistance to infection by RNA viruses *in vitro*.

The transcription of IFN-I and pro-inflammatory genes depends on kinase TBK1 and converges on latent transcription factors (TF) such as NF-κB, IRF3, and AP-1 subunits. We, therefore, analyzed the expression and activation of these components upon SOD1^{Mut} expression to determine the mechanistic impact on the pathway. Consistent with previous data, we found only the expression of *Irf1* and *Irf7*, both ISGs, were highly upregulated, whereas the expression of other IRFs, NF-κB, and AP1 family members remained comparable in the SOD1-G85R brain compared to WT brain samples (Figure 2J). Furthermore, the ectopic expression of SOD1^{Mut} in microglia resulted in phosphorylation of TBK1 and IRF3 (Figure 2K). Transcriptional induction of *Ifnb1* and *Rsad2* by SOD1^{Mut} was completely abrogated in both TBK1 and IRF3 CRISPR-Cas9-targeted microglia (Figure 2L). In summary, these results suggest that, although, SOD1^{Mut} does not target the expression of TF, the activation of the IFN-I pathway promotes neuroinflammation in ALS.

ALS-SOD1^{Mut} triggered IFN-I responses through cGAS-STING pathway

Because the induction of IFN-I-associated genes by SOD^{Mut} are blocked in TBK1-IRF3-deficient cells, we speculated that ALS-SOD1^{Mut} interfered directly or acted upstream of the TBK1-IRF3-axis. During pathogen recognition receptor signaling, coordination of upstream sensors with their respective adaptor molecules is critical for activating the IRF3-NF-κB-AP1 enhanceosome complex to initiate the IFN-I response. Therefore, we next examined whether these components were necessary for engaging SOD1^{Mut}-dependent IFN-I induction by generating a series of CRISPR-Cas9 knockout microglia (Figure 3A). As shown in Figure 3B, SOD1^{Mut} expression in microglia-deficient in RIG-I (encoded by *Ddx58*), MDA5 (encoded by *Ifih1*), and MAVS continued to produce comparable levels of *Ifnb1* mRNA. This observation was not cell-type specific, as it was also confirmed using MAVS-deficient human astrocytes, HASTR/ci35 cells (Figure 3C). TIR-domain-containing adapter-inducing IFN-β (TRIF, encoded by *Ticam-1*)-deficient microglia also fully responded to SOD1^{Mut} expression (Figure 3D). These results indicate that ALS-SOD1^{Mut} is able activate the IFN-I response independently of both RIG-I-like receptors (RLR) and Toll-like receptors pathways.

HEK293T cells have been shown to be deficit of the cyclic GMP-AMP synthase (cGAS)-STING DNA-sensing pathway, rendering them very easy to transfect with DNA plasmids (Langereis et al., 2015). Because

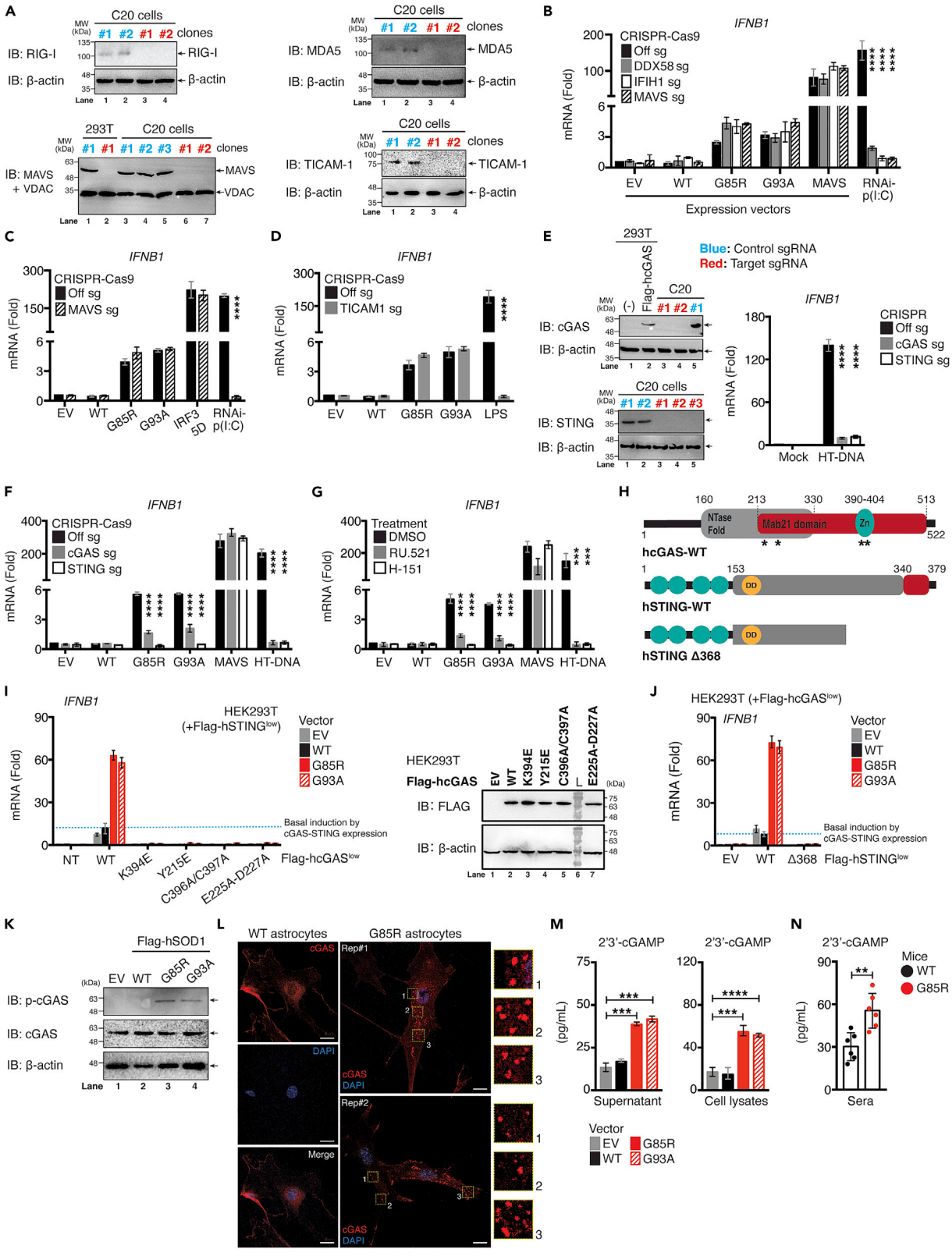
A
C20 cells
#1 #2 #1 #2 clones
IB: RIG-I
RIG-I
IB: β-actin
β-actin
293T
C20 cells
#1 #1 #1 #2 #3 #1 #2 clones
IB: MAVS + VDAC
MAVS
VDAC
IB: MDA5
MDA5
IB: TICAM-1
TICAM-1
B
IFNB1
CRISPR-Cas9
Off sg
DDX58 sg
IFIH1 sg
MAVS sg
mRNA (Fold)
EV
WT
G85R
G93A
MAVS
RNAi-p(I:C)
Expression vectors
C
IFNB1
MAVS sg
IRF3 5D
D
TICAM1 sg
LPS
E
293T
Flag-hcGAS
Blue: Control sgRNA
Red: Target sgRNA
IB: cGAS
IB: STING
CRISPR
cGAS sg
STING sg
Mock
HT-DNA
F
cGAS sg
STING sg
HT-DNA
G
Treatment
DMSO
RU.521
H-151
H
NTase Fold
Mab21 domain
Zn
hcGAS-WT
DD
hSTING-WT
hSTING Δ368
I
HEK293T (+Flag-hSTING^low)
Vector
EV
WT
G85R
G93A
Basal induction by cGAS-STING expression
NT
K394E
Y215E
C396A/C397A
E225A-D227A
Flag-hcGAS^low
HEK293T
Flag-hcGAS
IB: FLAG
IB: β-actin
J
HEK293T (+Flag-hcGAS^low)
Δ368
Flag-hSTING^low
K
Flag-hSOD1
IB: p-cGAS
IB: cGAS
IB: β-actin
L
WT astrocytes
G85R astrocytes
cGAS
DAPI
Merge
Rep#1
Rep#2
M
2'3'-cGAMP
Supernatant
Cell lysates
N
Mice
WT
G85R
Sera

Figure 3. Activation of IFN-I response by ALS SOD1-mutants is dependent on the cGAS-STING signaling pathway

(A) Knockout efficiency of *Ddx58* (RIG-I), *Ifih1* (MDA5), *Mavs*, or *Ticam-1* (TRIF) gene in C20 cells examined via western blotting.

(B) WT, DDX58, IFIH1, or MAVS-CRISPR/Cas9-deficient C20 cells either transfected with 0.01 μg Flag-SOD1 WT, G85R, G93A, or MAVS plasmids for 36 h, or 0.5 μg poly(I:C) for 8 h. *Ifnb1* mRNA measured using RT-qPCR.

(C) Similar conditions as in panel B performed using WT or MAVS-CRISPR/Cas9-deficient HASTR/ci35 cells, except human MAVS plasmid was replaced with human IRF3 5D plasmid. *Ifnb1* mRNA assessed via RT-qPCR.

(D–F) WT, TICAM, cGAS or STING-CRISPR/Cas9-deficient C20 cells either transfected with 0.01 μg Flag-SOD1 WT, G85R, G93A, or MAVS plasmids for 36 h, treated with LPS (100 ng/mL) for 4 h or transfected with HT-DNA (5.0 μg/mL) for 8 h. *Ifnb1* mRNA measured via RT-qPCR. The knockout efficiency of cGAS, or STING assessed via western blot and functional assays.

(G) WT C20 cells either treated with RU.521 (5.0 μg/mL) or H.151 (0.5 μg/mL) for 24 h. Cells were then transfected with 0.01 μg of Flag-SOD1 WT, G85R, G93A, or MAVS plasmids, or HT-DNA (1.0 μg/mL). *Ifnb1* mRNA was measured via RT-qPCR.

(H) Schematic diagram of Flag-tagged cGAS-WT and mutants (location indicated by asterisk), STING-WT and deletion mutants.

(I) HEK293T cells stably expressing low amounts of Flag-STING-WT clones were first generated. The clones were further co-reconstituted with low expression of either Flag-cGAS-WT or point mutated plasmids. After selection, the double-positive clones cells were then transfected with 0.01 μg of Flag-SOD1 WT, G85R, or G93A plasmids. *Ifnb1* mRNA was assessed via RT-qPCR. Protein expression for cGAS-WT and mutants from the 1.0 μg transfected samples were examined. Expression efficiency for each plasmid was evaluated via western blotting.

(J) Similar conditions as in I were used but replaced with Flag-cGAS-WT plasmid co-transfected with either STING-WT or deletion mutant (Δ368). *Ifnb1* mRNA was measured using RT-qPCR.

(K) Protein lysates collected from C20 cells expressing the indicated plasmids were subjected to immunoblotting with the indicated antibodies.

(L) Immunofluorescence staining of endogenous cGAS in primary astrocytes cells derived from day-10 WT, or G85R transgenic mice.

(M) Both supernatant and lysates from C20 cells overexpressed with the indicated plasmids were collected and subjected to ELISA analysis of cGAMPs.

(N) Sera was prepared from whole blood derived from SOD1 WT or G85R mice, followed by ELISA analysis of cGAMPs (day-10). All RT-qPCR of RNA samples were normalized to β-actin. Data represent the mean of three independent experiments (mean ± SEM). *p< 0.05, **p< 0.01, ***p< 0.001, ****p< 0.0001; (B–G, M, and N: unpaired Student's *t* test). See also Figure S4.

HEK293T cells do not respond to SOD1^{Mut}, we hypothesized that the cGAS-STING-axis was essential. Remarkably, we found that microglia lacking either cGAS or STING failed to respond to both Herring-testes DNA (HT-DNA, a positive control) and SOD1^{Mut}while retaining a full response to MAVS (Figures 3E and 3F). Similar observations were found when the SOD1^{Mut} vectors were expressed in microglia treated with either RU.521 (a cGAS inhibitor) or H-151 (an STING inhibitor) (Figure 3G). We then tested several cGAS and STING mutants to further elucidate this mechanism (Figure 3H). As expected, the reconstitution of cGAS catalytic domain deletions (E225A-D227A), the DNA-binding (C396/397A), phosphorylation (Y215E), and oligomerization (K394E) domain mutants in HEK293T cells failed to respond to SOD1^{Mut} compared with cGAS-WT (Figure 3I). Similarly, STING-WT robustly upregulated *Ifnb1* expression when co-expressed with cGAS-WT in HEK293T but not with the deletion mutant STING-Δ368, which lost its ability to bind TBK1 (Figure 3J). Importantly, SOD1^{Mut} overexpression resulted in phosphorylation of cGAS at residue Tyr-215 (Figure 3K). In agreement with this data, condensation of cGAS to form cytoplasmic puncta as previously described (Du and Chen, 2018) also occurred in primary astrocytes derived from SOD1-G85R, but not in WT mice (Figure 3L). Besides, we also detected the presence of secondary messenger GMP-AMP (cGAMP) in both lysate and supernatant from SOD1^{Mut} stably expressing microglia (Figure 3M). This further prompted us to examine the level of cGAMPs *in vivo*. As shown in Figure 3N, we observed a significant increase in total serum levels of cGAMPs in the G85R model. Collectively, these data showed that the ALS-SOD1^{Mut} initiated an innate immune response through the cGAS-STING pathway to promote neuroinflammation and neuronal cell death in the SOD1^{Mut}-ALS model.

IFNAR signaling is required for ALS-SOD1^{Mut} to promote neuronal inflammation

Secreted IFN-β proteins, after binding to transmembrane IFNAR, will induce the translocation of the interferon-stimulating-gene factor-3 (ISGF3) complex (comprising IRF9-STAT1-STAT2) into the nucleus to initiate the transcription of ISGs. We then investigated the contribution of IFNAR signaling to the inflammatory response in the context of SOD1-induced ALS pathology. As expected, the induction of ISGs mRNA were completely abrogated in STAT1-deficient microglia upon SOD1^{Mut} expression. Because the cGAS-TBK1-IRF3-axis remained unaffected, the lack of a positive amplification feedback loop only resulted in a partial loss of *Ifnb1* mRNA expression (Figures S4A and S4B). Furthermore, the SOD1^{Mut}-induced transcription of chemokines and NF-κB-dependent genes (*Cxcl10, Ccl3, Il6, Nos2*) were also significantly downregulated in STAT1-deficient cells (Figures S4C and S4D). Consistent with this, pre-treatment of WT microglia with IFN-β proteins further enhanced the levels of ISG and inflammatory gene expression (Figure S4E). To test the translational potential of these findings, we treated SOD1-G93A mice with vehicle, or IFNAR-neutralizing antibody weekly starting at the age of 8-weeks-old. Antibody treatment abrogated ISG expression, improved motor function, and survival (Figures S4F–S4H), demonstrating that transient

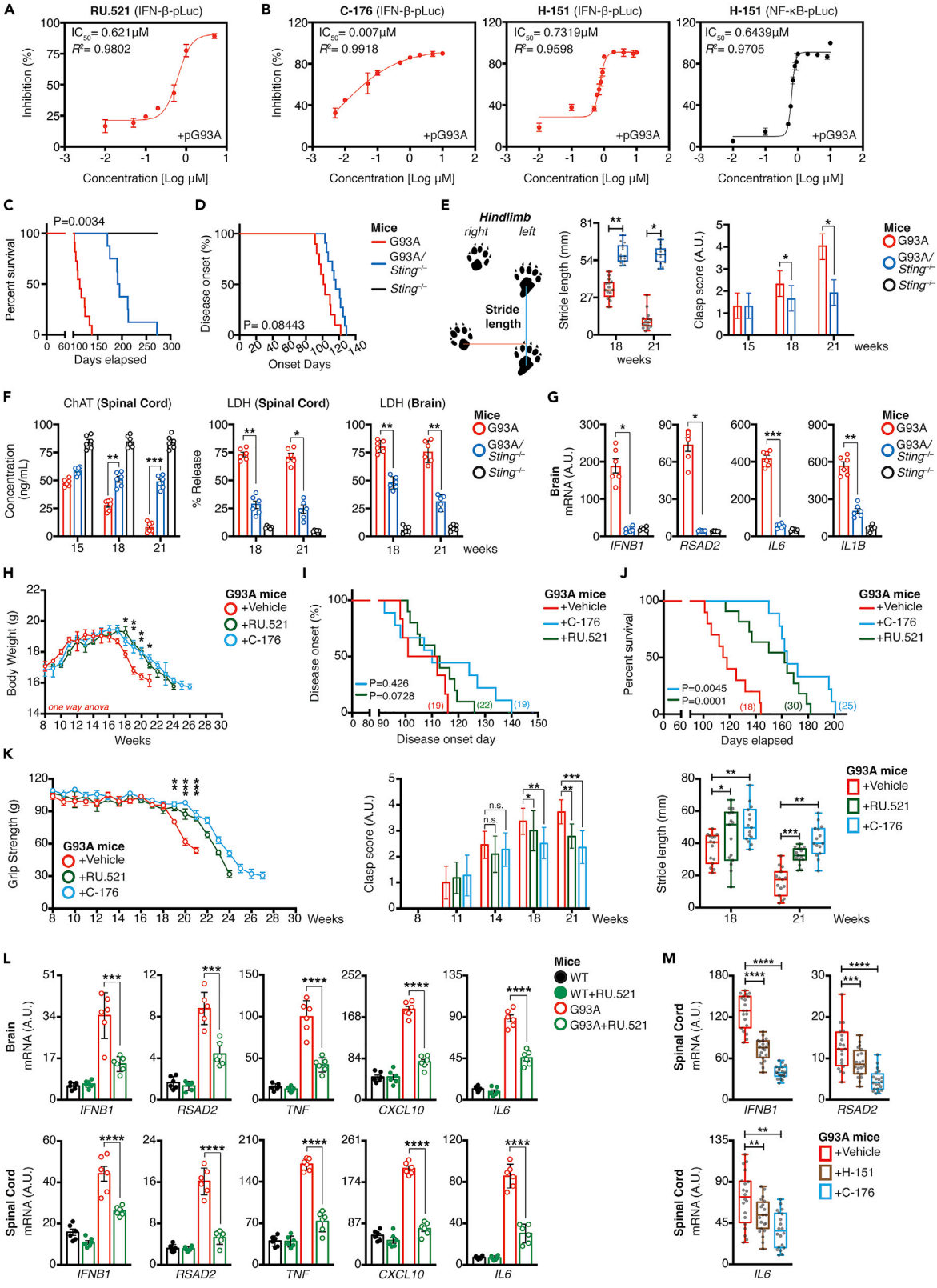
A
RU.521 (IFN-β-pLuc)
IC50= 0.621μM
R2= 0.9802
+pG93A
Inhibition (%)
Concentration [Log μM]
B
C-176 (IFN-β-pLuc)
IC50= 0.007μM
R2= 0.9918
H-151 (IFN-β-pLuc)
IC50= 0.7319μM
R2= 0.9598
H-151 (NF-κB-pLuc)
IC50= 0.6439μM
R2= 0.9705
C
P=0.0034
Percent survival
Days elapsed
D
P= 0.08443
Disease onset (%)
Onset Days
Mice
G93A
G93A/Sting−/−
Sting−/−
E
Hindlimb
right
left
Stride length
Stride length (mm)
Clasp score (A.U.)
weeks
F
ChAT (Spinal Cord)
LDH (Spinal Cord)
LDH (Brain)
Concentration (ng/mL)
% Release
G
Brain mRNA (A.U.)
IFNB1
RSAD2
IL6
IL1B
H
Body Weight (g)
one way anova
Weeks
G93A mice
+Vehicle
+RU.521
+C-176
I
Disease onset (%)
P=0.426
P=0.0728
Disease onset day
J
Percent survival
P=0.0045
P=0.0001
Days elapsed
K
Grip Strength (g)
Clasp score (A.U.)
Stride length (mm)
L
Brain mRNA (A.U.)
Spinal Cord mRNA (A.U.)
IFNB1
RSAD2
TNF
CXCL10
IL6
WT
WT+RU.521
G93A
G93A+RU.521
M
Spinal Cord mRNA (A.U.)
IFNB1
RSAD2
IL6
+H-151

Figure 4. cGAS and STING pharmacological inhibitors ameliorates ALS neuropathology in the SOD1-G93A model

(A and B) SIM-A9 cells co-transfected with luciferase reporters and 0.01 μg of the indicated SOD1 mutant plasmids in the presence of RU.521, H-151, or C-176. Estimated EC_{50} values from dose-response curves of the indicated inhibitors were measured.

(C–E) Kaplan-Meier plot of disease-onset days, survival rate, or motor performance of indicated time-point for G93A, *Sting*$^{-/-}$, or G93A/*Sting*$^{-/-}$-double-positive mice. Schematic diagram indicates how the gait performance (stride-length, *blue line*) of each mouse was measured.

(F) *In vivo* ChAT and LDH levels from brain and spinal cord homogenates isolated at the indicated time-points in G93A, *Sting*$^{-/-}$, or G93A/*Sting*$^{-/-}$-double-positive mice.

(G) Expression of the indicated mRNA *in vivo* in brain isolated from week-21 of G93A, *Sting*$^{-/-}$, or G93A/*Sting*$^{-/-}$-double-positive mice.

(H–J) Body weight of vehicle and inhibitor-treated groups were measured (H). Kaplan-Meier plot of disease-onset days, or survival time (I and J) of vehicle and inhibitor-treated groups. Number of mice used in each group as indicated.

(K) Grip strength, hindlimb grasping, or gait performance test of G93A mice after challenge with vehicle, RU.521 (500 μg), or C-176 (500 μg).

(L and M) Basal gene expression of indicated mRNA *in vivo* in brain and spinal cord isolates from G93A mice challenged with vehicle, RU.521 (500 μg, i.p.), or C-176 (500 μg, i.p.) at Week 21 analyzed by RT-qPCR. Number of dots = number of mice (biological replicates) used in each condition. All RT-qPCR of RNA samples was normalized to β-actin. Unless indicated, data represent the mean of at least three independent experiments (mean ± SEM). *p< 0.05, **p< 0.01, ***p< 0.001, ****p< 0.0001; (E–H and K–M: unpaired Student's *t* test; C, D, I, and J: Log rank Mantel-Cox test).

inhibition of the IFN response can improve the functional outcome of ALS. Collectively, these results indicated that IFNAR signaling is the key $SOD1^{Mut}$-controlled mechanism for activating the neuroinflammatory responses.

Therapeutic benefits of cGAS and STING inhibitors in a murine model of ALS

Consistent with our earlier findings (Figure 3), we observed that cGAS inhibition with pharmacological inhibitors, RU.521, potently diminished G93A-induced IFN-β reporter activities, with a 50% effective inhibitory concentration (EC_{50}) of 0.621 μM (Figure 4A), whereas two of the STING inhibitors tested—H-151 (EC_{50} of 0.7319 μM) and C-176 (EC_{50} of 0.007 μM) on IFN-β reporter activities (Figure 4B, *red curve*) and a EC_{50} of 0.6439 μM by H-151 on NF-κB reporter activities (Figure 4B, *black curve*). To this end, we hypothesized that STING inhibition would attenuate disease in SOD1-G93A mice. To evaluate this relationship, we generated genetically modified animals by crossing SOD1-G93A with *Sting*$^{-/-}$ deficient mice to obtain G93A/*Sting*$^{-/-}$ double-positive mice. Remarkably, STING-deletion, and thus cGAS/IFN-I inactivation, resulted in a pronounced 107-day extension in median survival [G93A, 145.0 ± 2.311 days; G93A/*Sting*$^{-/-}$, 252.0 ± 1.42 days (logrank Mantel p = 0.0034)] (Figure 4C), although disease onset did not differ between both groups (Figure 4D).

We then evaluated motor functions through gait performance, measuring motor limb strength and coordination in ALS models using stride analyses. Stride is defined as the distance between each successive mice paw print on a single side of a sheet of paper. As the disease progress, mice are unable to move their hindlimbs as much with each step, and therefore, the stride distance decreases. This measure also reflects the complication of front limb weakness, such that mice were unable to extend their front limbs normally, as a result, the back-to-front stride distance also declined. This was evident on weeks 18 and 21, whereas all vehicle treatment groups, continued to decline at a steady rate. We observed a drastic improvement of stride length (p< 0.05) in G93A/*Sting*$^{-/-}$-double-positive mice (Figure 4E, *left*). Analysis of hindlimb grasping score, a second method used to assess motor functions, indicated that the STING-depletion group also consistently displayed remarkable recovery in feet-clasping capability (Figure 4E, *right*). We further examined motor neuron cell survival by measuring the level of choline acetyltransferase (ChAT), an enzyme that synthesizes the neurotransmitter acetylcholine, a typical marker for healthy spinal cord motor neurons (Casas et al., 2013). As shown in Figure 4F, the number of healthy spinal cord motor neurons steadily declined between weeks 15–21; conversely, STING-deletion provided drastic protection (p< 0.01) and effectively blocked spinal motor neurons cell death in SOD1-G93A mice on weeks 18 and 21. We also observed a significant reduction in LDH release from the brain and spinal cord homogenates collected from G93A/*Sting*$^{-/-}$-double-positive mice as compared to the vehicle group (Figure 4F, p< 0.05). RT-qPCR quantification of brain mRNA confirmed the reduction of cytokine genes (Figure 4G, p< 0.05). These results indicated that the genetic ablation of the STING pathway achieved significantly greater neuro-protective efficacy and helped improve motor performance in the SOD1-G93A mutant ALS model.

Based on the promising results from G93A/*Sting*$^{-/-}$ mice, we next examined whether *in vivo* administration of cGAS, and STING inhibitors could provide therapeutic benefit on muscle performance and disease progression. To test this, we continued to monitor the motor function, weight loss, and atrophy using the rapidly progressive ALS mouse model SOD1-G93A injected either with vehicle, RU.521, or C-176, weekly

starting at 8-week of age. Beginning at 8-week of age, all SOD1-G93A mice received intraperitoneal injection of either 500 μg of C-176, RU.521, or an equivalent amount of vehicle, twice weekly for the first four weeks to achieve a maximal cumulative dose, then once per week thereafter. These treatments were given until the experimental endpoint. As shown in Figure 4H, both groups showed the same trend of initial weight gain followed by a gradually weight loss until the endpoint. However, compared to aged-matched controls, animals treated with RU.521 and C-176 maintained and/or gained weight ($p \leq 0.05$) up to week-18 and week-21, beyond the expected endpoint of disease progression. Consistently, the onset of the disease in SOD1-G93A mice also showed a marginal improvement after treatment with RU.521, and C-176; although this difference did not reach statistical significance (logrank test for survival plot: $p = 0.426$ for C-176; $p = 0.0728$ for RU.521) (Figure 4I). Conversely, the mean survival period displayed a significant increase from 50 to 78 days in treated mice (Vehicle, 117.5 $\pm$ 1.528 days; RU.521, 168.0 $\pm$ 2.363 days [log rank $p = 0.0001$]; C-176, 188.0 $\pm$ 3.672 days [log rank $p = 0.0045$]) (Figure 4J). We next evaluated whether both RU.521 and C-176 could improve the functional performance of SOD1-G93A mice, as assessed by stride length, hindlimb grip strength, and the clasping test at several age-points. Compared to aged-matched controls, animals treated with RU.521 and C-176 displayed improved motor function based on grip strength from weeks 19–27 and the differences at weeks 19 and 21 were statistically significant (One-way ANOVA, Week 19, $p = 0.0069$; Week 20, $p = 0.0009$; Week 21, $p = 0.0006$) (Figure 4K, *left*). In addition, most control-treated mice showed a complete paralysis of the hindlimbs, and hence did not manifest a feet-clasping phenotype upon tail suspension, whereas both the RU.521 and C-176-treated groups showed a marked improvement in the feet-clasping phenotype and rearing activity from weeks 14–21 (Figure 4K, *middle*). In line with this result, gait performance by measuring the footprint stride length further indicated that mice receiving either RU.521 or C-176 showed significantly better maintenance of the motor phenotype of the hindlimbs at both 18 and 21-weeks of age, compared with vehicle group, which showed gait abnormalities (i.e., shorter stride length, $p < 0.05$) (Figure 4K, *right*). This suggests that blocking cGAS and/or STING conferred protection to neuronal damaged *in vivo*. Furthermore, we also observed a significant reduction in mRNA levels of IFN-I, ISGs, pro-inflammatory, and chemokines genes in the end-stage brain and spinal cord from inhibitor-treated mice (Figure 4L). H-151, another potent, irreversible small molecule antagonist of STING (Haag et al., 2018; Vincent et al., 2017), also behaved similarly in reducing *Ifnb1*, *Rsad2*, and *Il6* mRNA expression within the spinal cord of G93A mice, albeit less robust than C-176 (Figure 4M). Nonetheless, as the disease progressed and SOD1-G93A mice reached the end stage (i.e., the length of time between disease onset and the disease endpoint), mice became weak and immobile, whereas inhibitor-treated mice showed much better health conditions. They groomed and explored their cages, illustrating marked beneficial effects of RU.521 and C-176 on muscle performance as the disease progressed. Collectively, these results demonstrated that administration of cGAS or STING inhibitors in SOD1-ALS *in vivo* model ameliorated the ongoing inflammation found in the CNS, which further contributed to improve motor function and lifespan.

ALS-SOD1^{Mut} damaged mitochondria and the released mtDNA activated the cGAS-STING pathway

cGAS is a well-known innate immune sensor that surveys the cytosol for the presence of self- and non-self-DNA (Gao et al., 2013; Härtlova et al., 2015; Sun et al., 2013). We next questioned the source of DNA that activated cGAS in SOD1^{Mut}-ALS. Pathological changes including mitochondrial abnormalities in the SOD1 model have been elucidated previously (Jaarsma et al., 2000, 2001; Pedrini et al., 2010), whereas other studies have shown that the released mtDNA from apoptotic cells could trigger an immune response (West et al., 2015), the relationship between these has not been described in SOD1^{Mut}-ALS. Thus, we examined whether SOD1^{Mut} expression could trigger the release of mtDNA to the cytoplasm. SOD1^{Mut} transfected microglia were subjected to subcellular fractionation. After confirming the purity of each fraction (Figure 5A), we found that the expression of SOD1^{Mut} in microglia and astrocytes showed a significant two- to 5-fold enrichment of mtDNA (*dloop*, *Mt-atp6*) in the cytosolic fraction compared to EV and WT (Figure 5B). Similarly, fractionation of the extracts derived from the whole brain, spinal cord, primary microglia, and astrocytes of the G85R transgenic mice also showed a significant enrichment of other mtDNA genes, including *Mt-co1* and *Mt-nd1* (Figures 5C–5E). Confocal microscopic analysis confirmed that SOD1^{Mut}-induced elevated levels of dsDNA in the cytosol. We also found that the mitochondria were more intact and were localized perinuclearly in EV or WT compared to a more fractionated and stretchy morphology in SOD1^{Mut}-expressing microglia (Figure 5F), which coincided with the dissipation of mitochondrial membrane potential in primary microglia and astrocytes of the G85R-mutated mice (Figure 5G), confirming the dysfunction and mitochondrial damage observed in SOD1-ALS pathology.

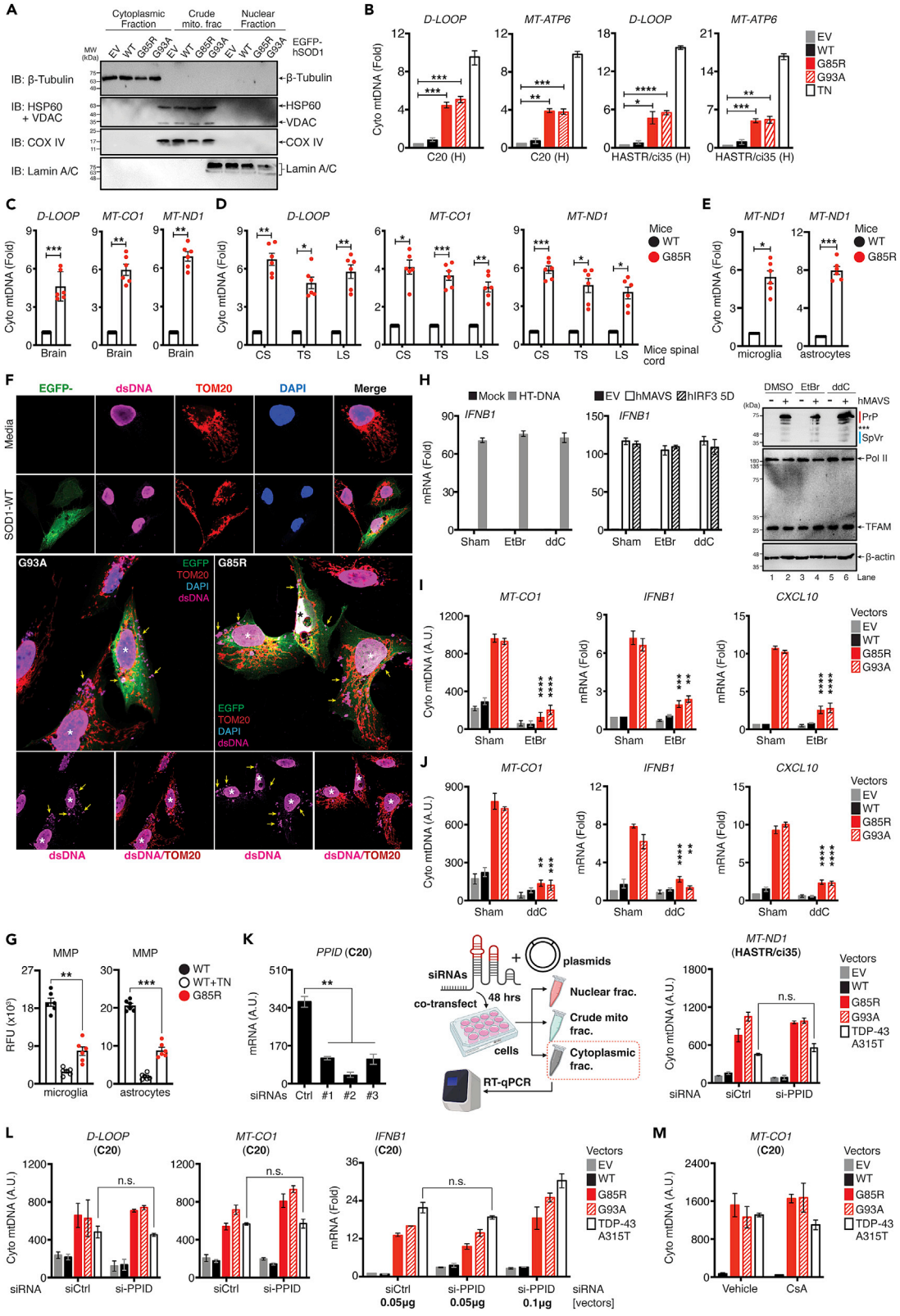
A
Cytoplasmic Fraction
Crude mito. frac
Nuclear Fraction
EGFP-hSOD1
IB: β-Tubulin
IB: HSP60 + VDAC
IB: COX IV
IB: Lamin A/C
B
D-LOOP
MT-ATP6
Cyto mtDNA (Fold)
C20 (H)
HASTR/ci35 (H)
EV
WT
G85R
G93A
TN
C
MT-CO1
MT-ND1
Brain
D
CS
TS
LS
Mice
Mice spinal cord
E
microglia
astrocytes
F
EGFP-
dsDNA
TOM20
DAPI
Merge
Media
SOD1-WT
G93A
G85R
dsDNA
dsDNA/TOM20
H
Mock
HT-DNA
IFNB1
mRNA (Fold)
Sham
EtBr
ddC
EV
hMAVS
hIRF3 5D
DMSO
hMAVS
PrP
SpVr
Pol II
TFAM
β-actin
Lane
I
CXCL10
Vectors
J
G
MMP
RFU (x10³)
WT
WT+TN
G85R
K
PPID (C20)
siRNAs
Ctrl
#1
#2
#3
plasmids
siRNAs
co-transfect
48 hrs
cells
Nuclear frac.
Crude mito frac.
Cytoplasmic frac.
RT-qPCR
MT-ND1 (HASTR/ci35)
siRNA
siCtrl
si-PPID
n.s.
TDP-43 A315T
L
D-LOOP (C20)
MT-CO1 (C20)
IFNB1 (C20)
siCtrl 0.05μg
si-PPID 0.05μg
si-PPID 0.1μg
siRNA [vectors]
M
Vehicle
CsA

Figure 5. ALS SOD1-mutants damage mitochondria and release mtDNA to activate the IFN-I response

(A and B) WT C20 and HASTR/ci35 cells were either treated with 1.0 μg/mL of tunicamycin for 8 h or transfected with indicated plasmids and 36 h after transfection, cells were subjected to fractionation and blotted with indicated antibodies (A). Total DNA extracted from cytosolic and nuclear fractions as treated in A. Cytosolic mtDNA genes was assessed via RT-qPCR (B).

(C and D) Total DNA was harvested from the cytosolic and nuclear fractions as in A from whole brain and spinal cord lysates of WT or G85R mice at Week 60. Cytosolic mtDNA genes was assessed.

(E) Primary microglia and astrocytes derived from WT or G85R mice at day-10 after birth were subjected to subcellular fractionation as in A. Cytosolic mtDNA genes were assessed.

(F) Immunofluorescence staining of dsDNA in C20 cells transfected with plasmids encoding EGFP-SOD1 WT,-G85R, or-G93A.

(G) Primary microglia and astrocytes derived from age-matched WT or G85R mice (day-10) were harvested and subjected to MMP assay.

(H) C20 cells transfected either with HT-DNA (5.0 μg/mL), or Flag-MAVS/IRF3 5D plasmids (0.1 μg each) were either Sham, ddC, or EtBr treated. *Ifnb1* mRNA was measured via RT-qPCR (*left*). Protein expression was analyzed through western blotting (*right*).[Note: MAVS in standard form (~52 kDa) are marked by asterisk (***); splicing variants, truncated forms, midi and mini-MAVS (<52 kDa) are marked by vertical *blue line* (Brubaker et al., 2014; Qi et al., 2017); MAVS in higher molecular weight (>52 kDa) are marked by vertical *red line* (Hou et al., 2011)].

(I) C20 cells transfected with indicated plasmids were either sham or EtBr (150 ng/mL) treated for 4 days. Samples were subjected to fractionation and DNA extraction, followed by RT-qPCR analysis of mtDNA genes and the indicated mRNA. Statistical analysis corresponding to the same condition in the Sham treated group.

(J) C20 cells transfected with the indicated plasmids were either sham or ddC (50 μg/mL) for 6-day. Samples were subjected to fractionation and DNA extraction, followed by RT-qPCR analysis of mtDNA gene and the indicated mRNA. Statistical analysis corresponds to the same conditions as the Sham treated group.

(K) Knockdown efficiency of the *Ppid* gene in HASTR/ci35 cells was validated (*left*). Experimental design of HASTR/ci35 cells co-transfected with indicated siRNA (10 nM) and 0.01 μg plasmids (*middle*). 48 h later, cells were subjected to fractionation described in A and quantification of mtDNA genes.

(L) Similar experimental design as in panel K using C20 cells. mtDNA genes and *Ifnb1* mRNA was quantified.

(M) C20 cells transfected with indicated plasmids were either vehicle (DMSO) or CsA (20 μM) treated. Samples were subjected to fractionation and DNA extraction, followed by measuring of *Mt-co1*. RT-qPCR of all mtDNA genes was normalized to genomic DNA, *TERT*. RT-qPCR of RNA samples was normalized to β-actin. Data represent the mean of four independent experiments (mean ± SEM). Number of dots = number of mice. *p< 0.05, **p< 0.01, ***p< 0.001, ****p< 0.0001; (B–E, G, and I–L: unpaired Student's *t* test). (RFU = relative fluorescence unit; A.U. = arbitrary unit). See also Figure S5.

Next, we examined whether the released of mtDNA was the ligand that activated IFN-I through the cGAS-STING pathway. To this end, we depleted mtDNA by treating cells with ethidium bromide (EtBr) or dideoxycytidine (ddC) to inhibit mtDNA replication (Kai et al., 2006; Kao et al., 2012; Nelson et al., 1997; Yu et al., 2007). We confirmed that the protein expression induced by the transfected plasmid and the signaling pathway remained unaffected (Figure 5H), although these treatments resulted in a significant reduction in mtDNA and a reduction in the expression of *Ifnb1* and *Cxcl10* mRNA in $SOD1^{Mut}$-transfected microglia (Figures 5I and 5J). Next, we generated TFAM-deficient microglia (Figure S5A), as we speculated that depletion of this mtDNA-associated protein may enhance the accessibility of mtDNA to activate the innate immune response. Notably, TFAM-depleted microglia enhanced detectable levels of cytosolic mtDNA upon tunicamycin treatment (a positive control for triggering mtDNA accumulation) (Sun et al., 2017; Yu-zefovych et al., 2013) or transfection with $SOD1^{Mut}$ plasmids (Figures S5B and S5C). *Ifnb1*, *Cxcl10*, and ISG expression were also enhanced in $SOD1^{Mut}$-transfected TFAM-depleted cells (Figure S5D). We further substantiated this by transfecting the pure cytosolic fraction of $SOD1^{Mut}$ cells treated with proteinase K (Figure S5E). As shown in Figure S5F, the proteinase K treated purified cytosolic fraction showed a complete absence of TFAM proteins and increased detectable levels of cytosolic mtDNA upon $SOD1^{Mut}$ expression (Figure S5G). Consequently, we observed a significant upregulation of *Ifnb1* expression compared with the untreated control fraction of $SOD1^{Mut}$-transfected cells, and such an enhancement was notably abrogated in cGAS- or STING-depleted cells (Figures S5H and S5I). Finally, while this study was in preparation, the group of Seth Masters reported a similar observation in the Transactive response DNA-binding protein-43 (TDP-43 mutants, $TDP\text{-}43^{Mut}$)-driven ALS (Yu et al., 2020). Other authors have reported that TDP-43 triggers the release of mtDNA through the mitochondrial permeability transition pore (mPTP) and activates the cGAS-STING pathway (Yu et al., 2020). Hence, we questioned whether $SOD1^{Mut}$ could also trigger the released of mtDNA through a similar mechanism. We employed the siRNA approach to deplete the expression of peptidyl-prolyl isomerase D (PPID, encoded by the *Ppid* gene), an integral constituent of the mPTP complex. After confirming the knockdown efficiency (Figure 5K, *left*), we then co-transfected both siRNA and plasmids expressing either $SOD1^{Mut}$ or $TDP\text{-}43^{Mut}$ into the human astrocyte HASTR/ci35 cell lines and subjected them to subcellular fractionation (Figure 5K, *middle*). Our results revealed that the release of mtDNA in $SOD1^{Mut}$ expressing cells remained unaffected in the cytoplasmic fraction of *Ppid*-depleted cells when compared to controls (Figure 5K, *right*). Conversely, and to our surprise, we found no significant differences in the abundance of mtDNA triggered by TDP-43 A315T in *Ppid*-depleted cells versus controls. This prompted us to question whether the observation was cell-type specific. We then performed the similar experiments using another neuronal cell lineage, C20 cells. Again,

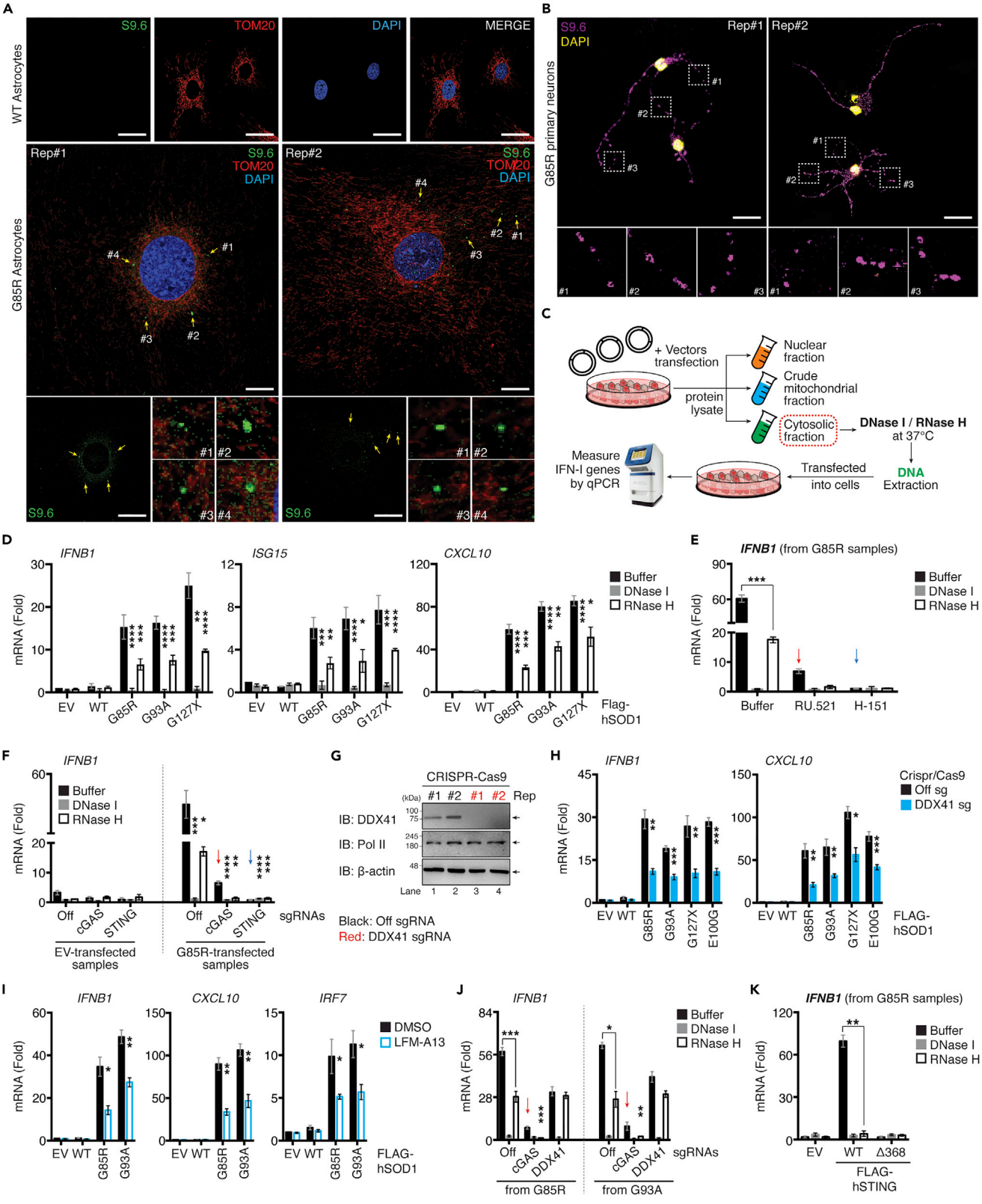
A
S9.6
TOM20
DAPI
MERGE
WT Astrocytes
G85R Astrocytes
Rep#1
Rep#2
B
G85R primary neurons
Rep#1
Rep#2
C
+ Vectors transfection
protein lysate
Nuclear fraction
Crude mitochondrial fraction
Cytosolic fraction
DNase I / RNase H at 37°C
DNA Extraction
Transfected into cells
Measure IFN-I genes by qPCR
D
IFNB1
ISG15
CXCL10
mRNA (Fold)
Buffer
DNase I
RNase H
EV
WT
G85R
G93A
G127X
Flag-hSOD1
E
IFNB1 (from G85R samples)
Buffer
RU.521
H-151
F
IFNB1
Off
cGAS
STING
sgRNAs
EV-transfected samples
G85R-transfected samples
G
CRISPR-Cas9
Rep
IB: DDX41
IB: Pol II
IB: β-actin
Lane
Black: Off sgRNA
Red: DDX41 sgRNA
H
IFNB1
CXCL10
Crispr/Cas9
Off sg
DDX41 sg
E100G
FLAG-hSOD1
I
IFNB1
CXCL10
IRF7
DMSO
LFM-A13
FLAG-hSOD1
J
IFNB1
DDX41
from G85R
from G93A
K
IFNB1 (from G85R samples)
Δ368
FLAG-hSTING

Figure 6. ALS SOD1-mutants trigger mt(RNA:DNA) hybrid release and activate IFN-I responses through the DDX41-STING axis

(A and B) Primary neurons and astrocytes extracted from WT or G85R-mice at day-10 after birth were fixed and immunostained with indicated antibodies and DAPI (blue).

(C) Schematic diagram of DNase I/RNase H treatment experiments. Pure cytosolic fraction from C20 cells transfected with 0.01 μg of Flag-SOD1 WT or SOD1-mutant vectors for 36 h were incubated with either buffer, DNase I or RNase H, followed by DNA extraction. These samples were re-transfected into cells and subjected to gene quantification.

(D) RT-qPCR analysis of the indicated mRNA from samples derived from experimental design described in panel C.

(E) WT C20 cells treated with RU.521 (5.0 μg/mL) or H-151 (0.5 μg/mL) for 24 h. Cells were then transfected with DNA extracted from EV and G85R-transfected samples as described in C. RNA was purified and *Ifnb1* mRNA was measured using RT-qPCR.

(F) WT, cGAS, or STING-deficient C20 cells were transfected with DNA extracted as described in panel C, *Ifnb1* mRNA was measured via RT-qPCR.

(G) CRISPR/Cas9 DDX41-deficient C20 cells validated by western blotting.

(H) WT or DDX41-deficient C20 cells were transfected with 0.01 μg of indicated plasmids, and the indicated mRNA was measured using RT-qPCR.

(I) WT C20 cells transfected with the indicated plasmids and treated with DMSO or LFM-A13 (100 μM). RNA was purified and *Ifnb1* mRNA was measured via RT-qPCR.

(J) DNA extracted from G85R or G93A-transfected samples and prepared as described in panel C were re-transfected into WT, cGAS, or DDX41-deficient cells for 6 h. *Ifnb1* mRNA expression was measured.

(K) DNA extracted from G85R-transfected samples prepared as described in C were re-transfected into HEK293T cells expressing either EV, Flag-tagged STING-WT, or STING Δ368. RNA was purified and *Ifnb1* mRNA was measured using RT-qPCR. All RT-qPCR of RNA samples was normalized to β-actin. Data represent the mean of three independent experiments (mean ± SEM). White scale bars correspond to 10 μm *p< 0.05, **p< 0.01, ***p< 0.001, ****p< 0.0001; (D–F and H–K: unpaired Student's *t* test). See also Figure S6.

we obtained a similar result, with concurrent robust *Ifnb1* mRNA expression in both controls and *Ppid*-depleted cells (Figure 5L). We further substantiated these findings by treating cells with cyclosporin A (CsA), a potent inhibitor of cyclophilin D and a well-established pharmacological inhibitor of the mPTP pore. Our results indicated that the abundance of the cytoplasmic fraction of mtDNA remained comparable in either the SOD1^{Mut} or TDP-43^{Mut} expressing C20 cells in the absence or presence of CsA treatment (Figure 5M), suggesting that the release of mtDNA in SOD1^{Mut}-expressing neuronal cells was not dependent on mPTP. Collectively, our data suggest that ALS-SOD1^{Mut} damaged mitochondria, and the released of mtDNA further activated neuronal innate immune responses through the cGAS-STING axis.

ALS-SOD1^{Mut} triggered the released of mt(RNA:DNA) hybrid to activate the DDX41-STING pathway

We observed a complete abrogation of IFN-I levels in STING-depleted cells, while retaining residual signals in cGAS-depleted cells (Figure 3F), which led us to speculate that another sensor functioning upstream of STING likely contributed to the SOD1^{Mut}-dependent IFN-β response. As mtDNA contains RNA hybridized to DNA, damaged mitochondria may leak these structures into the cytoplasm. Remarkably, we could detect the presence of RNA:DNA hybrid intermediates in the cytosol of primary astrocytes and motor neurons extracted from transgenic G85R but not in extracts from WT mice (Figures 6A and 6B). These prompted us to validate the S9.6 staining by subjecting the fixed G85R primary astrocytes samples to mock or enzymatic treatments before immunostaining. Notably, pre-treatment with RNase H (RNase H), an enzyme which specifically degrades the RNA strand of the RNA:DNA hybrid, led to a significant decrease of total cellular S9.6 staining, with a reduction of approximately 4-fold (Figure S6A) (p< 0.001). In comparison, treatment with RNase T1, an endoribonuclease that specifically targets single-stranded RNA, did not have an effect on total cellular S9.6 staining when compared to mock treated samples (Figure S6A), indicating that the majority of the S9.6 signals derived from immunostaining of fixed G85R primary astrocytes stemmed from the specific binding of S9.6 to mt(RNA:DNA) hybrids. Next, we assessed whether the mt(RNA:DNA) hybrid could contribute to the SOD1^{Mut}-induced IFN-I response. We treated the purified cytosolic fraction with RNase H and re-transfected them into WT microglia (Figure 6C). As shown in Figure 6D, the RNase H-treated cytosolic fraction from SOD1^{Mut}-transfected cells showed a significant reduction in *Ifnb1*, *Isg15*, and *Cxcl10* mRNA expression, these inductions were abrogated in microglia lacking cGAS or STING (Figures 6E and 6F). However, buffer-treated cytosolic fraction from SOD1^{Mut}-expressing cells continued to produce a residual expression in cGAS^{KO} cells (≈4-fold) but not in STING^{KO} microglia (Figures 6E and 6F; Red versus blue arrow), indicating that mt(RNA:DNA) hybrid contributed to SOD1^{Mut}-induced IFN-I response independent of cGAS but still required STING.

Both DDX41 and cGAS have been shown to recognize RNA:DNA intermediates (Mankan et al., 2014; Stavrou et al., 2018). Our study has excluded the latter. Hence, we asked whether DDX41 was critical for SOD1^{Mut}-induced IFN-I and thus, generated DDX41-deficient microglia (DDX41^{KO}, Figure 6G). Although the mtDNA levels are comparable with WT (Figure S6C), *Ifnb1* and *Cxcl10* mRNA expression was significantly

downregulated in DDX41^{KO} microglia upon expression of ALS-SOD1^{Mut} (Figure 6H). To further substantiate this observation, mt(RNA:DNA) derived from the fractionated cytoplasmic fraction of SOD1^{Mut}-expressing microglia were immunoprecipitated with the S9.6 antibody. Small aliquots of the pulled-down lysates were re-transfected into HeLa cells for validation through immunostaining. As shown in Figure S6B, cells transfected with the S9.6 pulled-down lysate showed cytoplasmic puncta staining but this was not observed in cells transfected with IgG-control pulled-down lysate, confirming the predominant constituent of the S9.6 pull-down product was mt(RNA:DNA). We then re-introduced the remaining lysates into WT, cGAS^{KO}, or DDX41^{KO} microglia, followed by RT-qPCR analysis. We observed that the mt(RNA:DNA)-induced *Ifnb1* mRNA expression was significantly impaired (≈10-fold, $p < 0.001$) in DDX41^{KO} cells but not in WT and cGAS^{KO} microglia (Figure S6B, *right*). Further, cells treated with LFM-A13, a molecular inhibitor of Bruton's tyrosine kinase (BTK), which phosphorylates DDX41 to induce the IFN-I response (Lee et al., 2015), also significantly downregulated the SOD1^{Mut}-induced *Ifnb1*, *Cxcl10*, and *Irf7* expression in microglia, oligodendrocytes, or motor neuron cells (Figures 6I and S6D–S6F). Furthermore, transfection of DDX41-but not in cGAS-deficient microglia with the RNase H-treated cytosolic fraction from SOD1^{Mut} cells produced a comparable amount of *Ifnb1* mRNA compared to buffer-treated controls (Figure 6J), suggesting the importance of DDX41 in sensing cytosolic mt(RNA:DNA). To determine whether cGAS or DDX41 is the primary sensor for mtDNA or mt(RNA:DNA), respectively, we treated microglia with siRNA targeting IFI16 and ZBP1, other known critical DNA sensors in non-neuronal cells (Almine et al., 2017; Takaoka et al., 2007; Unterholzner et al., 2010). Knockdown of both proteins did not influence *Ifnb1* expression derived from the buffer-treated SOD1^{Mut}-cytosolic fraction (Figures S6G and S6H). Finally, we accessed whether STING functioned downstream of DDX41 on sensing mt(RNA:DNA). Given that HEK293T still expresses DDX41, but not STING. Reconstitution of STING-WT restored *Ifnb1* expression in HEK293T cells transfected with buffer-treated but not with the RNase H-treated cytosolic fraction. No induction was observed in STING-Δ368 co-transfected cells (Figure 6K). Collectively, these findings indicate that mtDNA or mt(RNA:DNA) released from damaged mitochondria primarily activate the cGAS- or DDX41-STING pathway, respectively, to induce the IFN-I response in the SOD1^{Mut}-ALS model.

Cell-cell contact was essential for the propagation of ALS-SOD1^{Mut}-dependent IFN-I responses

Activation of IRF3 and NF-κB is the hallmark to trigger robust IFN-I and pro-inflammatory responses. To better characterize the molecular mechanisms induced by ALS-SOD1^{Mut}, we used human microglia and transduced them with an amino-terminally EGFP-tagged SOD1-G85R construct and analyzed both IRF3 and NF-κB activation by immunofluorescence microscopy. As expected, transient expression of EGFP-SOD1-G85R in the microglia led to the activation and re-localization of IRF3 and NF-κB to nuclear complexes when compared to non-SOD1^{Mut}expressing cells (Figure S7A, *asterisk*). Strikingly, we also observed the nuclear localization of IRF3 and NF-κB in microglia lacking pEGFP-SOD1-^{G85R} expression, which were located adjacent to pEGFP-SOD1^{G85R}-expressing cells (Figure S7A, *white arrows*). Notably, this phenomenon of bystander cell activation was not observed when the microglia were transfected with polyinosinic:polycytidylic acid [poly(I:C), p(I:C)], a synthetic analog of double-stranded RNA (dsRNA) acting as a molecular mimic associated with viral dsRNA produced during viral replication (Figure S7A, *right lower panel*). Because polyI:C activates the cytosolic RNA sensor RLR pathway, these results indicate that both IRF3 and NF-κB activation of surrounding cells occurs via an event that is linked to cGAS activity.

Next, we hypothesized that SOD1^{Mut}-expressing cells would be capable of propagating IFN-I to bystander cells. We employed a *trans*-well culture system that could separate donor and recipient cells. This experimental set-up could effectively block the bystander cell activation. With this aim, we established four different experimental groups involving both co-cultures or *trans*-well system: Group 1 comprised only NSC-34 motor neurons cells; Group 2 comprised WT HEK293T and NSC-34 cells in co-culture; Group 3 comprised HEK293T cells expressing STING co-incubated with NSC-34 expressing SOD1^{Mut} in the *trans*-well system; and Group 4 comprised HEK293T expressing FLAG-STING cells co-cultured together with SOD1^{Mut} expressing NSC-34 cells (Figure S7B). We observed robust transactivation of the IFN-β reporter and the induction of IFN-I associated genes in Group 4 but not in Groups 1, 2, and 3 conditions (Figures S7C and S7D), indicating that a cell-to-cell contact-dependent propagation mechanism was responsible for relaying IFN-I signals.

Next, we investigated whether a similar mechanism was responsible for the release of NF-κB-dependent pro-inflammatory cytokines. We first performed experiments based on the original set-up described in

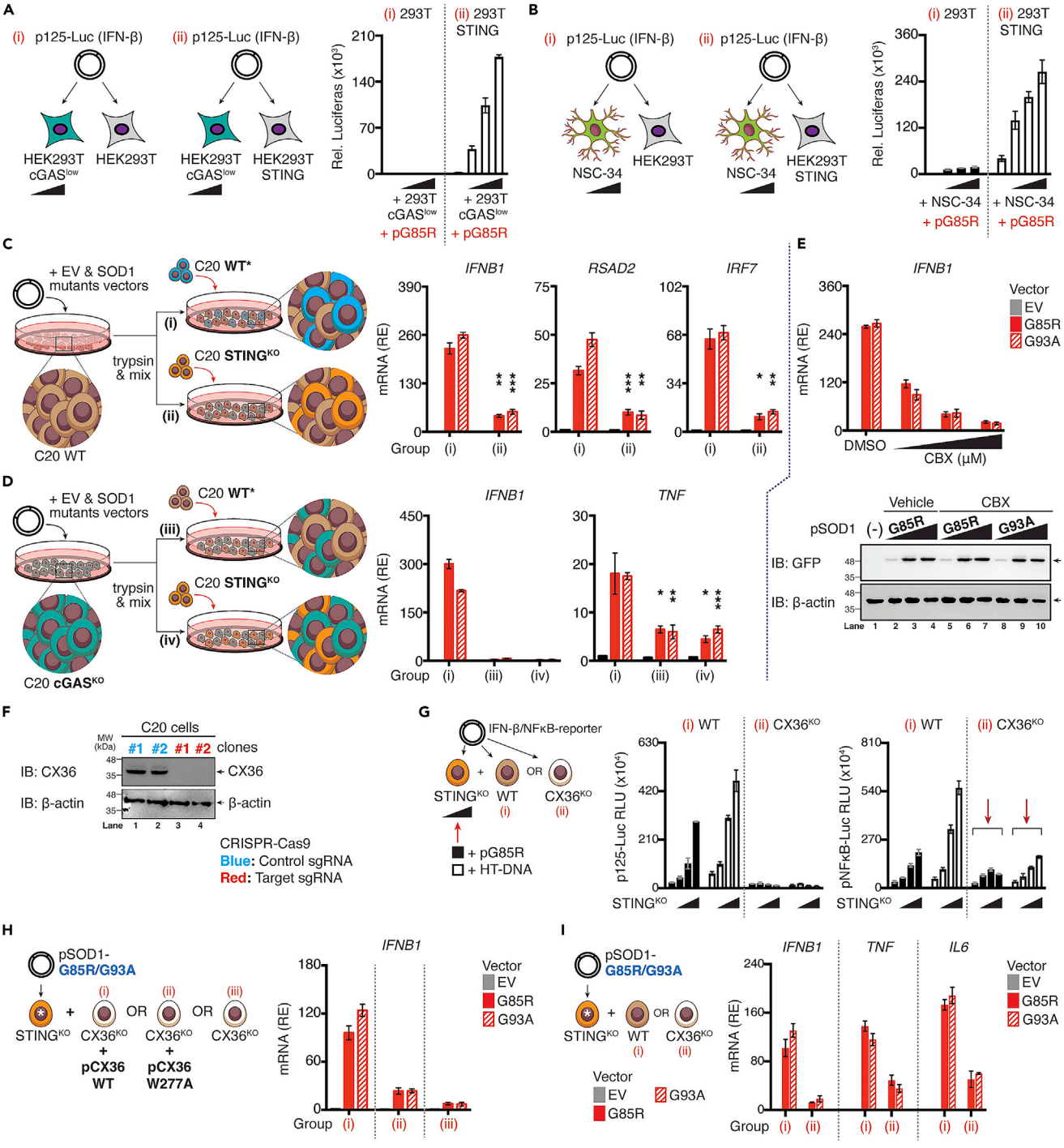

Figure 7. Connexin-36 mediate cGAMP(2′ 5′) intercellular transfer in human microglia

(A and B) HEK293T and HEK293T-STING cells were co-cultured with HEK293T cGAS^{low} or NSC-34 cells (ratio ranging from 1:0.5 to 1:0.125), followed by transfection with p125-Gluc (IFN-β), whereas transactivation of the reporter was assessed after 24 h.

(C and D) WT (C, *brown*), or cGAS-deficient C20 cells (D, *green*) expressing either EV, SOD1-WT, or mutants were co-cultured with WT [marked by asterisk (*), *blue*] or STING-deficient C20 cells (*orange*). Relative induction of indicated mRNA from each group (i, ii, iii, or iv) was measured via RT-qPCR.

(E) C20 cells expressing EV, WT, or mutants SOD1 in the absence or presence of CBX (150 μM) were subjected to RT-qPCR of *Ifnb1* mRNA (*upper*). The protein level of indicated SOD1 mutants in C20 cells after treatment with CBX was assessed via western blotting using specific antibodies (*lower*).

(F) CX36-deficient C20 cells generated through CRISPR/Cas9 system are validated by western blotting.

Figure 7. *Continued*

(G) Schematic diagram of experimental design. WT or CX36-deficient C20 cells (*white*) were co-cultured with increasing ratios of STING-deficient C20 cells (ratios ranging from 1:0.5 to 1:0.125) containing either SOD1-G85R mutants or HT-DNA (0.1 μg/mL), followed by transfection with p125-/NF-κB-pLuc. Luciferase activity was measured after 24 h.

(H) STING-deficient C20 cells expressing SOD1-G85R/93A mutants [marked with asterisk (*)] were co-cultured with CX36-deficient cells alone or reconstituted with CX36 WT or W277A mutant plasmids. Relative expression (RE) of *Ifnb1* mRNA from each designated group (i, ii, or iii) was measured with RT-qPCR.

(I) STING-deficient C20 cells expressing EV, SOD1-G85R/93A mutants [marked with asterisk (*)] were co-cultured with either WT or CX36-deficient C20 cells. After 36 h, relative expression of indicated mRNA from designated group (i or ii) were measured via RT-qPCR. All RT-qPCR of RNA samples were normalized to β-actin. Data represent the mean of at least three independent experiments (mean ± SEM). *p< 0.05, **p< 0.01, ***p< 0.001, ****p< 0.0001; (C and D: unpaired Student's *t* test). See also Figure S7.

Figure S7D, with slight modifications, whereby STING-stably expressing HEK293T cells in both Groups 3 and 4 were replaced with WT HEK293T cells (Figure S7E). These conditions were originally hypothesized to act as a negative control in parallel with the experimental conditions described in Figure S7D. Unexpectedly, we still observed the induction of *Tnf* or *Tnfaip3* (a TNFα-inducible gene) in Group 4. Furthermore, this bystander pro-inflammatory gene activation was also observed when WT HEK293T cells were co-incubated with $SOD1^{Mut}$-expressing NSC-34 cells in the *Trans*-well system (*Group 3*, Figure S7F), suggesting that the contact free bystander propagation of pro-inflammatory responses may also occur through a cGAS-STING-independent pathway. To provide additional supporting evidence, we used similar experimental conditions as those described in Figure S7E but replaced the WT HEK293T cellswith HEK293T cells expressing NF-κB luciferase reporters (Figure S7G). Switching the recipient cells also produced comparable results: NF-κB promoter transactivation was observed in both Groups 3 and 4 but not in Groups 1 and 2 (Figure S7H). To validate that this cGAS-STING-independent NF-κB activation *in trans* was not because of the migration of cells through the semipermeable membrane of the *trans*-well system, we replaced NSC-34 cells with microglia (Figure S7I). Consistently, we could still detect *Tnf*, but not *Ifnb1* expression in Group 3 (Figure S7J, *blue arrow*). Furthermore, RT-qPCR analysis also failed to detect the expression of either *Iba1* or *Cd11b* genes (microglial cell markers) in the wells containing HEK293T-cells (Figure S7J, *black bars*), which excluded that the *Tnf*-producing cells as observed in Group 3 were from migrated microglia. We then questioned whether bystander activation of NF-κB could occur via a paracrine loop. Immunofluorescence microscopy analysis of microglia treated with tumor necrosis factor receptor 1 (TNFR1) blocker indicated that nuclear NF-κB translocation could still be observed in bystander cells upon $SOD1^{Mut}$ expression (Figure S7K, *arrows*), suggesting that paracrine signaling was not the mediator of bystander activation. To investigate the role of protein secretion more broadly, we investigated whether these phenomena could be impaired when the cellular secretory pathway was abolished by the protein transport inhibitor brefeldin A (BFA). To determine whether drug treatment blocked cytokine secretion (Hong et al., 2019), using poly(I:C) as a negative control, BFA exerted no effect on bystander activation upon $SOD1^{Mut}$ expression in microglia (Figure S7L, *arrows*), suggesting that cell-cell propagation of pro-inflammatory signals was not mediated by the extracellular secretory pathway. Overall, these results collectively conveyed two messages: (1) ALS-$SOD1^{Mut}$ propagates and amplifies IFN-I signaling to bystander cells through intact physical cell-to-cell contact; and (2) Cell contact free bystander propagation of $SOD1^{Mut}$-induced pro-inflammatory cytokines also occurs via a route independent of the cGAS-STING pathway.

CX36 propagated cGAS-STING-dependent IFN-I signals to bystander cells in SOD1-ALS

To directly assess the functional role of cGAS-STING-axis in bystander activation, we next generated monoclonal HEK293T cGAS cells with low constitutive expression of cGAS ($cGAS^{low}$). This monoclonal line would require the extrinsic DNA stimulation to activate STING and that of the downstream IRF3. As shown in Figure 7A, titrating the number of HEK293T $cGAS^{low}$ cells over STING competent cells in conjunction with G85R transfection revealed a dose-dependent increase in IFN-β promoter transactivation [Group (i) versus (ii)]. This bystander STING activation phenomenon was also observed when HEK293T STING cells co-cultured with G85R-expressing NSC-34 cells that are inherently competent for cGAS (Figure 7B). We then further investigated this mechanism using a genetic approach. Amino-terminal EGFP-tagged $SOD1^{Mut}$ (G85R or G93A) expressing WT human microglia were seeded and co-cultured either together with WT (Group i), or $STING^{KO}$ human microglia (Group ii). RT-qPCR analysis revealed that the mRNA expression of antiviral genes *Ifnb1*, and ISGs (*Rsad2*, *Irf7*) was significantly downregulated when $SOD1^{Mut}$-expressing cells were co-cultured with $STING^{KO}$ as compared to WT (Figure 7C). Moreover, switching $SOD1^{Mut}$-expressing WT microglia to $SOD1^{Mut}$-expressing $cGAS^{KO}$ microglia completely abrogated *Ifnb1* mRNA expression while retaining a residual of *Tnf* gene (Figure 7D). Taken together, these

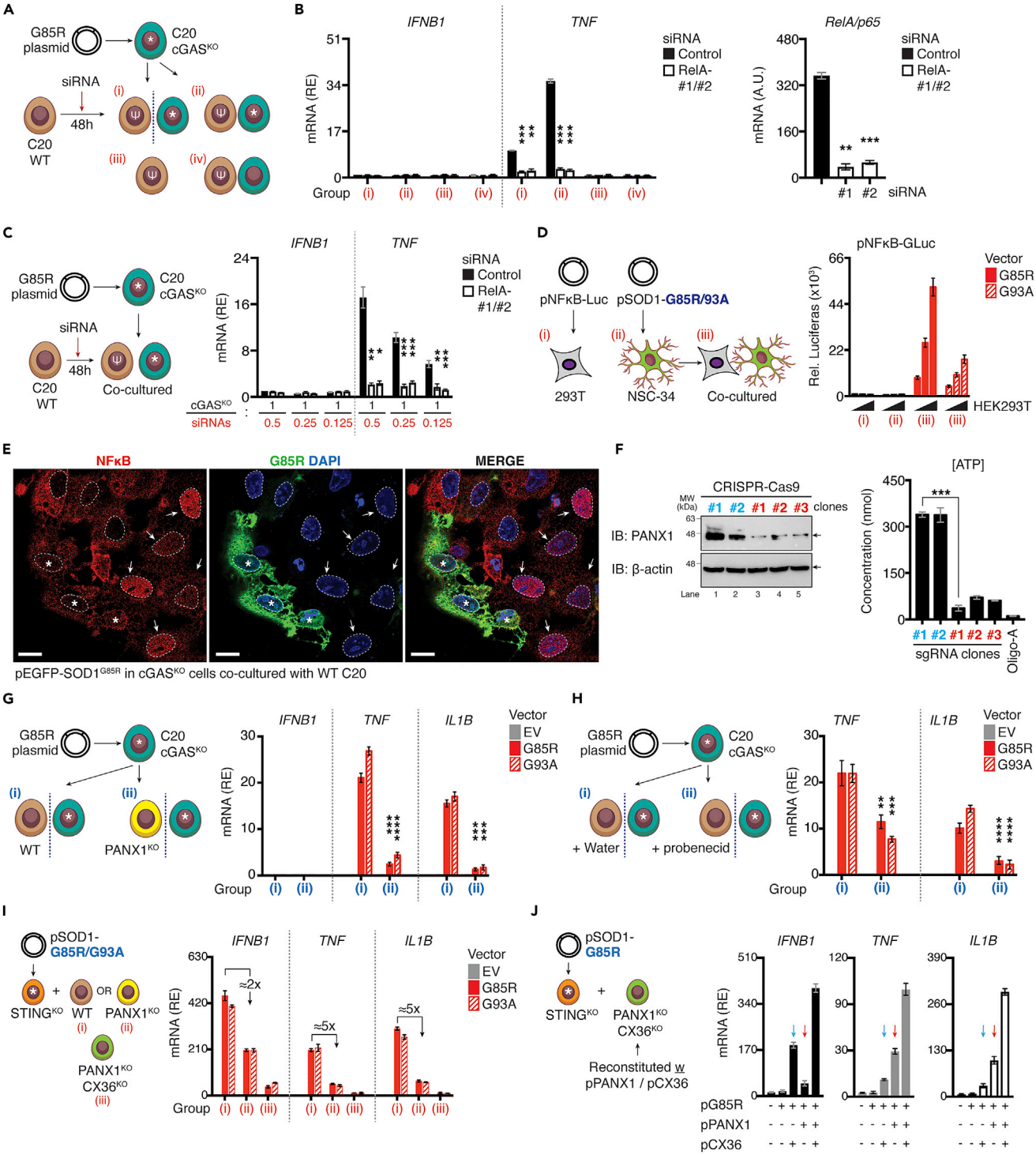

Figure 8. Pannexin-1 and connexin-36 cooperatively propagate NF-κB dependent cytokines to bystander cells

(A and B) Schematic diagram showing the experimental design. cGAS-deficient C20 cells expressing G85R plasmid [marked with asterisk (*)] were co-cultured with WT C20 cells transfected with 20 nM of indicated siRNAs [marked with epsilon (ψ)] in the presence or absence of the *trans*-well system. The expression of indicated mRNA were measured via RT-qPCR. Knockdown efficiency of *RelA* gene is shown (B, *right*).

(C) cGAS-deficient C20 cells expressing G85R plasmid [marked with asterisk (*)] co-cultured with titrated number of WT C20 cells transfected with 20 nM of the indicated siRNAs [marked with epsilon (ψ)] in increasing ratios of (1:0.5/0.25/0.125). Expression of *Ifnb1*, or *Tnf* quantified via RT-qPCR.

Figure 8. *Continued*

(D) HEK293T cells expressing NF-κB reporter plasmid and NSC-34 cells expressing SOD1 mutants were culture alone or co-cultured before the luciferase assay.

(E) Confocal analysis of pSOD1-G85R expressing cGAS-deficient cells co-cultured with WT C20 cells. EGFP-G85R stably expressing cells are marked with asterisk (*). Nuclear translocation of NF-κB in bystander cells is indicated by white arrows. Nuclear-membrane is marked by white-dotted lines.

(F) Knockout efficiency of PANX1 using CRISPR-Cas9 verified using immunoblotting. Amount of ATP within cultured supernatant were measured using an ATP-assay. Treatment with 1.0 μM oligomycin A served as the positive control.

(G) cGAS-deficient C20 cells expressing G85R or G93A plasmid (indicated as asterisk) were co-incubated with WT or PANX1-deficient cells in the *trans*-well system. Statistical analysis shown in Group (ii) was performed comparing the same condition in Group (i).

(H) Similar experimental design as in (G) was used but the cell was replaced with WT C20 cells treated with vehicle (water) or 100 μM probenecid in the *trans*-well system. Statistical analysis shown in Group (ii) was performed comparing the same condition in Group (i).

(I) WT, PANX1-deficient (*yellow*), or PANX1-CX36-double deficient (*light green*) C20 cells were co-cultured with STING-deficient C20 cells expressing SOD1-mutants [marked by asterisk (*), *orange*]. Relative induction of the indicated mRNA from designated groups (i, ii, or iii) were quantified via RT-qPCR. Fold-reduction is indicated.

(J) PANX1-CX36-double deficient (*light green*) C20 cells were reconstituted with WT PANX1 or CX36 plasmids before co-culturing with STING-deficient C20 cells expressing G85R for 36 h. Relative induction of *Ifnb1, Tnf,* or *Il1b* mRNA was measured. All RT-qPCR data were normalized to β-actin. Data represent the mean of at least three independent experiments (mean ± SEM). *p< 0.05, **p< 0.01, ***p< 0.001, ****p< 0.0001; (B, C, and F–H: unpaired Student's *t* test).

results provide direct functional evidence for cGAS-dependent STING activation of IFN-I *in trans*, in parallel with the cGAS-STING independent bystander propagation of pro-inflammatory responses.

The detection of DNA by cGAS leads to the production of secondary messenger cGAMP, which can pass through cellular gap junctions to activate the STING-dependent IFN-I pathway in bystander cells (Ablasser et al., 2013). We, therefore, evaluated the impact of carbenoxolone (CBX), an inhibitor of cellular gap junctions. WT human microglia treated with increasing doses of CBX produced significantly less *Ifnb1* mRNA upon $SOD1^{Mut}$ expression without affecting the protein levels (Figure 7E), indicating the involvement of cellular gap junctions in bystander propagation. Gap junctions formed by the connexins family represent a well-established route of cell-cell contact-dependent intercellular communication. Consequently, to investigate the mechanisms of intercellular cGAMP transfer in the ALS-$SOD1^{Mut}$ model, we simultaneously targeted CX36 ($CX36^{KO}$) or CX43/45 ($CX43\text{-}CX45^{DKO}$-double knockout) in human microglia using the CRISPR-Cas9 system (Figures 7F and S8A). $CX36^{KO}$, or $CX43\text{-}CX45^{DKO}$ cells showed normal responsiveness in *Ifnb1* mRNA expression toward LPS, poly(I:C), and IRF3 5D, indicating that IFN-I responses were intact in these cells (Figure S8B). However, co-cultured of $CX43\text{-}CX45^{DKO}$ cells with an increased number of $STING^{KO}$ microglia did not result in substantial differences of IFN-β reporter activities, as well as *Ifnb1*, *Tnf*, or *Il6* mRNA expression upon both $SOD1^{Mut}$ expression and HT-DNA transfection (Figures S8C and S8D). Conversely, $CX36^{KO}$ cells significantly reduced the levels of $SOD1^{Mut}$-dependent IFN-β reporter activity, while retaining NF-κB signals (Figure 7G, *red arrows*), as supported by FACS-single-cell analysis, in which co-culturing of fluorescence-labeled-cGAMPs pre-loaded $STING^{KO}$ cells (serving as the baseline) either with WT or $CX43\text{-}CX45^{DKO}$ cells led to a significant increase in the total number of cells positive for cGAMP-labeled fluorescence (p< 0.01). However, co-culturing with $CX36^{KO}$ had a minimal effect with the average number of cells that were cGAMP fluorescence-positive remained comparable to those found at baseline (Figure S8E, *middle*). These observations were congruent with the induction of *Ifnb1* mRNA expression (Figure S8E, *right*), suggesting that CX36 was the critical gap junction in the CNS that responsible for transferring cGAMPs to bystander cells for STING/IFN-I activation. Moreover, the reconstitution with the CX36 WT construct succeeded in restoring the $SOD1^{Mut}$-induced *Ifnb1* mRNA induction, but not of the W277A defective mutant (Siu et al., 2016) (Figure 7H). Consistently, only a fraction of pro-inflammatory genes was reduced (Figure 7I). Collectively, CX36 was essential for the inter-neuronal propagation of IFN-I responses in the ALS-SOD1 model.

CX36 and PANX1 channels cooperatively potentiated the neuronal inflammatory reaction

The activation of the NF-κB signaling pathway is required to mount an effective inflammatory response. To further delineate the molecular mechanisms that allow ALS-causing $SOD1^{Mut}$ to propagate pro-inflammatory cytokine responses to neighboring cells as observed in Figures S7E–S7H, we first asked whether these phenomena were NF-κB-dependent. To this end, we employed an siRNA approach using four experimental groups: Group (i) WT human microglia, C20, were transfected with siRNA-targeting RelA (p65, a key member of the NF-κB family) and were co-incubated with $cGAS^{KO}$ C20 cells expressing G85R in the *trans*-well system; Group (ii) Similar cell types and conditions as in Group (i) but without the *trans*-well system; Group (iii) RelA-depleted C20 cells alone, and Group (iv) RelA-depleted C20 cells co-cultured with $cGAS^{KO}$ C20 cells (Figure 8A). We failed to detect the induction of *Ifnb1* mRNA in the four experimental

groups, including Groups (i) and (ii), these results were expected as the cells lacked cGAS protein. Consistently, we still observed a mild induction of *Tnf* expression in the presence of the *trans*-well system, and a more robust induction when these were co-cultured together. However, such induction was completely abrogated in the presence of RelA-siRNA depleted C20 cells (Figure 8B). Co-culturing of RelA-depleted C20 cells on top of cGAS^{KO} C20 cells expressing G85R also revealed a dosage-reduced induction of *Tnf* mRNA expression in control cells, while drastically reduced in RelA-depleted cells (Figure 8C). Furthermore, co-incubation of NSC-34 expressing SOD1^{Mut} with an increasing number of HEK293T cells expressing the NF-κB reporter construct further showed a dosage-increment of luciferase activities (Figure 8D). Subsequently, we performed immunofluorescence staining analysis by co-culturing cGAS^{KO} C20 cells expressing EGFP-SOD1-G85R with WT C20 cells. We observed the nuclear translocation of NF-κB in bystander cells (Figure 8E). Collectively, these results suggest that ALS-associated SOD1^{Mut} cells are capable of propagating inflammatory responses to bystander cells independently of cGAS-STING and cell-cell contact, and that the expression of these inflammatory genes in bystander cells was dependent on NF-κB.

Pannexin-1 (Panx1) channels are capable of propagating signals through intercellular space. There has been growing evidence demonstrating that both Panx1 channels work cooperatively with connexin under pathological conditions, including neurodegeneration, inflammation, and epilepsy, allowing direct intercellular communication, bidirectional flow of ions, and signaling molecules like ATPs and glutamate to greatly facilitate the transmission of signals (Lohman et al., 2015; Makarenkova et al., 2018; Scemes et al., 2007; Zhou et al., 2019). To establish whether PANX1 is responsible for these phenomena, we generated PANX1-deficient microglia using the CRISPR-Cas9 system. According to protein expression detected by western blot, PANX1 sgRNA targeted pools displayed significant lower expression of PANX1 compared to control sgRNA targeted pool. Accordingly, functional analyses verified that the extracellular concentration of ATP was also drastically reduced across all clones (Figure 8F). Clone#1 cells were used in the subsequent analysis. Two experimental groups using *trans*-well system were designed as follows: Group (i) cGAS^{KO} C20 expressing SOD1^{Mut} were co-incubated with WT C20 cells and or Group (ii) cGAS^{KO} C20 expressing SOD1^{Mut} cells were co-incubated with PANX1^{KO} C20 cells. We observed that CRISPR-mediated deletion of *PANX1* significantly mitigated NF-κB-dependent gene expression in the *trans*-well culture conditions (Figure 8G). Similar findings were observed when WT C20 cells were treated with probenecid, an inhibitor of the PANX1 channel (Figure 8H), suggesting that the PANX1 channel plays a crucial role in propagating long-distance intercellular NF-κB-dependent inflammatory responses. We then attempted to establish whether PANX1 and CX36 could synergistically promote neuroinflammation in response to aberrant SOD1. To this end, three independent co-culture systems were established, whereby STING^{KO} C20 cells expressing either of SOD1^{Mut} were co-incubated with: Group (i) WT C20 cells, or Group (ii) PANX1^{KO} C20 cells, or Group (iii) PANX1-CX36-double deficient C20 cells (PANX1-CX36^{DKO}). We found that co-cultures with PANX1^{KO} cells showed a reduction in the overall inflammatory IFN-I and NF-κB signaling, while PANX1-CX36^{DKO} cells drastically diminished both (Figure 8I). Specifically, the fold-reduction in NF-κB signaling was higher than for IFN-I when PANX1 alone was depleted (Figure 8I, 5-fold vs 2-fold; Group i vs ii), indicating PANX1 possessed a stronger role over CX36 in regulating NF-κB gene expression. To provide further evidence, we reconstituted the expression of PANX1 and/or CX36 in PANX1-CX36^{DKO} C20 cells, which was followed by co-incubation with STING^{KO} cells expressing aberrant SOD1. Consistently, SOD1^{Mut} alone did not lead to the induction of any tested genes, while co-expressing SOD1^{Mut} with CX36 led to a significantly higher induction of *Ifnb1* mRNA over*Tnf*, and *Il1b* (Figure 8J, *blue arrow*). Conversely, restoring PANX1 expression with SOD1^{Mut} resulted in higher expression of NF-κB-dependent genes as compared to IFN-I (Figure 8J, *red arrow*). In summary, the *in vitro* data document a mechanism by which PANX1 and CX36 channels cooperatively enhance the long-distance intra- and intercellular propagation of IFN-I and NF-κB-dependent inflammatory response to bystander cells, with CX36 for IFN-I, and PANX1 for NF-κB signaling.

DISCUSSION

The role of neuroinflammation in worsening the progression of different ND is gaining increased recognition. These phenomena are dependent on a broader transcriptional program induced in neuronal-related cells, as well as other related cell types. Significant progress has been made in delineating how this transcriptional program is induced and regulated and a plethora of factors acting at the level of signaling pathways and TFs collectively contribute to the outcome of these responses. The mammalian genome encodes various regulatory factors that directly or indirectly controls immune gene expression in the CNS. Although

the consequences of inflammation in ALS are well-established, the underlying etiology remains unclear. IFN-I signaling has been shown to play a key role in the pathogenesis of Parkinson's (Sliter et al., 2018), Alzheimer's (Roy et al., 2020), and ALS (Wang et al., 2011). Although the mechanisms remain ambiguous, gene expression and immunohistochemical analyses of tissues derived from SOD1-G93A animals and sporadic ALS patients revealed elevated levels of ISGs (Wang et al., 2011). Only very recently, the cGAS/STING signaling pathway was shown to be associated with ALS resulting from a genetic aberration in TDP-43 (Yu et al., 2020) and chromosome nine open reading frame 72 (C9orf72) (McCauley et al., 2020); the former triggering mtDNA release and activating IFN-I via the cGAS-STING pathway, and the latter, harnessing the expansion of hexanucleotide repeat (GGGGCC) in the *C9orf72* gene leading to sub-optimal control of inflammation induced by STING-mediated IFN-I responses. Nevertheless, the mechanism underlying how STING is activated, whether via cGAS or via other sensors (if any) are involved in the activation, and if so, how this activation occurs, largely remain unexplored.

In this study, we demonstrated that cGAS/DDX41-STING-driven activation of IFN-I signaling exacerbates and contributes to progression of neurodegeneration in SOD1-driven ALS. Furthermore, we demonstrate that aberrant SOD1 damages cellular mitochondria and enhances the cytosolic release of mtDNA and RNA:DNA hybrids to initiate IFN-I activation. Using both gain-of-function and loss-of-function approaches, we provide critical insights into the biological implications of ALS-causing $SOD1^{Mut}$ both at the cellular and organism level. Unbiased transcriptome profiling of $SOD1^{Mut}$-derived brain tissues has demonstrated that the presence of $SOD1^{Mut}$ can selectively regulate the expression of a large number of immune-associated genes, all of which playing key roles in host defense against pathogens. Importantly, we have also demonstrated that the ectopic expression of $SOD1^{Mut}$ in various human neuronal, and non-neuronal cell lineages, including macrophages, induces IRF3 activation, followed by the expression of IFN-I associated genes, and NF-κB-dependent pro-inflammatory genes. Our study also demonstrated that STING-driven activation of IFN-I signaling is also elevated *in vivo* as was evident from our experiments showing that the ALS mouse model (G85R) produced elevated levels of IFN-I associated cytokine proteins. Pharmacological blockade of cGAS, STING, IFNAR, or IFNAR-dependent gene products, CCL2/MCP-1 in the rapidly progressive model (G93A) significantly ameliorated disease progression and prolonged the survival of these animals as compared to their control counterparts. However, our results showed that both cGAS and STING inhibition did not significantly delay the median time of disease onset. These observations are congruent with Yu et al., (2020), who stated that $STING^{KO}$-TDP43 double-positive mice did not demonstrate any impact on disease onset. Although inflammation is strongly associated with ALS, it is widely accepted that inflammation does not solely determine the onset of ALS. The exact mechanisms of how SOD1 and other mutated proteins trigger ALS remains unclear. Although we cannot be certain that all these effects are due only to the presence of ALS-causing $SOD1^{Mut}$, these results indeed provide compelling evidence for the *in vivo* physiological implications of $SOD1^{Mut}$ in the IFN-I signaling pathway.

In addition to identifying the physiologic functions of $SOD1^{Mut}$ both in isolated cells and *in vivo*, we further provide mechanistic insights into how $SOD1^{Mut}$ induces IFN-I gene expression. Although cGAS was required to maximize IFN-β gene expression, cGAS deficiency did not completely abrogated the *Ifnb1* mRNA abundance in $SOD1^{Mut}$-expressing microglia. However, the STING-dependent pathway was crucial for a complete abrogation. One explanation for this result is that cGAS and other DNA sensor(s) may induce redundant signaling pathways. We found that expression of ALS-linked $SOD1^{Mut}$ enhanced mitochondrial damage and stimulated cytosolic mtDNA and RNA:DNA release to activate cGAS-, or DDX41-dependent IFN-β gene expression in primary neuronal cells. As for the latter, sensing of mt(RNA:DNA) further recruited BTK to phosphorylate DDX41, and facilitated the activation of STING independent of any secondary messengers for IFN-I signaling. This is well supported by various genetic-knockout models, biochemical fractionation, and functional compensation studies using inhibitors, and enzyme treatments. Moreover, immunofluorescence staining of G85R-derived primary motor neurons and astrocytes clearly revealed the presence of these ligands. Moreover, evidence from our membrane potential ($\Delta\Psi$) and confocal experiments collectively revealed the disorganized and fragmentation of mitochondrial structure, lending support to the idea that $SOD1^{Mut}$ may act directly on this organelle, rather than indirectly via other major regulators within the cell.

TBK1 is an important signaling hub active downstream of cGAS. Recruitment of TBK1 to STING is essential to mediate IRF3 phosphorylation and nuclearization, leading to IFN-I production. Heterozygous loss-of-functions mutations in *Tbk1* gene have been implicated in familial ALS (Cirulli et al., 2015; Freischmidt et al.,

2015), whereas heterozygous deletion of the *Tbk1* gene *in vivo* significantly alleviated end-stage neuroinflammation and delayed disease progression in the SOD1 model (Brenner et al., 2019). Conversely, the basal induction of IFN-I remained unaffected, our experimental model suggested that TBK1 signaling remained intact. In the physiological setting, our observations were concordant with those of a previous study whereby a two-stage meta-analysis involving >4000 ALS patients concluded that the probability of *TBK1* mutations was extremely low and was not commonly found in ALS patients (~1.0–1.8%), despite the fact that their presence, indeed, increased the risk of developing ALS (Cui et al., 2018). Notably, it was reported that TDP-43 triggers the release of mtDNA through mPTP (Yu et al., 2020). However, we confirmed that ALS-causing $SOD1^{Mut}$ do not share such a mechanism. Unlike TDP-43, which invades mitochondria, SOD1 is ubiquitously expressed throughout the cytoplasm, nucleus, endoplasmic reticulum (ER), as well as mitochondria. Evidence also indicates that $SOD1^{Mut}$ are recruited into stress granules (Gal et al., 2016; Lee et al., 2020) and disruption of stress granules have been shown to reduce IFN-I signaling (Ng et al., 2013; Onomoto et al., 2012). Delineating these crosstalk pathways may advance our understanding of the underlying mechanisms of the IFN-I response in SOD1-ALS. Surprisingly, in our system, we observed that the depletion of mPTP does not affect the released of mtDNA by TDP-43 A315T. The underlying mechanism(s) for this discrepancy remains unclear. A potential factor could be the cell-line system used by the different studies. For example, we utilized two neuronal-related cell lines (an immortalized human microglia and astrocytes) in our system, whereas Yu et al., 2020 mainly utilized HEK293T and murine embryonic fibroblasts. Nevertheless, it has been well-characterized that HEK293T cells can serve as a natural "knockout" cell line as they do not express detectable cGAS or STING protein, and therefore, fail to activate IFN-I expression in response to DNA (Burdette et al., 2011; Sun et al., 2013). Nevertheless, it remains unclear how expression of the ALS-linked TDP-43 mutants (i.e., A315T and Q331K) in WT HEK293T cells could still activate the expression of *Ifnb1* mRNA as shown in other study (Yu et al., 2020). Future work is required to understand these discrepancies and to demonstrate how $SOD1^{Mut}$ damages the mitochondria.

Our mechanistic studies also indicate that $SOD1^{Mut}$ triggers a unique *in trans* immune signaling mechanism in microglia, where the cGAMP(2′-5′) produced by cGAS is delivered to bystander cells specifically through the gap junction CX36, which cooperatively amplifies the overall inflammatory reactions and PANX1. The mechanism whereby PANX1 propagates NF-κB-specific genes independently of cell-cell contact and cGAS/STING remains to be fully defined. At least two possibilities exist; first, PANX1 was previously shown to amplify the downstream effect after chronic exposure to key mediators of inflammation, including IL-1, and/or TNF-α through multiple feed-forward and feedback loops by promoting IL-1β production via MyD88-NF-κB activation and extracellular Ca^{2+} uptake (Yang et al., 2020). Alternatively, PANX1 has been shown to regulate ATP efflux that could serve as a paracrine and autocrine signal to activate P2X purinoceptor 7 ($P2X_7$) in neighboring cells for the inflammasome signalosome (Albalawi et al., 2017; Parzych et al., 2017; Wang et al., 2013). Occasionally, we did observe some $SOD1^{Mut}$ expressing cells with weaker IRF3/NF-κB nuclearization than in bystander cells without $SOD1^{Mut}$, although the underlying phenomenon remains ambiguous. One hypothesis we developed is that proper localization of STING to the mitochondria-ER-associated membrane is necessary to achieve robust IFN-I signaling (Barber, 2015). $SOD1^{Mut}$ damages mitochondria and disruption of STING localization weakens the signaling cascade, resulting in a weaker nuclearization of IRF3/NF-κB. As for bystander cells, activation of the IRF3/NF-kB pathway is simply based on the transfer of cGAMPs from neighboring cells. The mitochondrial-ER structure remains intact and STING localization is not affected, which leads to more robust IRF3/NF-κB nuclearization. Nonetheless, further clarification is warranted in the future.

In summary, the present study is the first demonstration that loss or inhibition of cGAS/STING signaling significantly extends lifespan and improves the functional performance of a mutant SOD1 disease model. The findings also suggest that cGAS/DDX41-STING signaling contributes to motor neuron death and eventual ALS disease progression. Hence, reducing the downstream consequences of STING activation through specific inhibitors is a promising approach for therapeutic intervention to decelerate ALS disease progression. The insights obtained from this investigation shall further advance our understanding of the physiological roles of $SOD1^{Mut}$ in STING-mediated IFN-I signaling and will contribute to expand the significance of these pathways in NDs.

Limitations of the study

This study also had limitations. First, all analyses were conducted using SOD1-G85R and G93A mice or were based on the SOD1-G85R and G93A genetic background, which have limitations in terms of modeling all

forms of ALS, particularly TDP-43, FUS, C9orf72, and other major hallmarks of sporadic and familial ALS. Another major limitation is that we did not attempt to longitudinally investigate the kinetics of the immune response in correspondence to disease progression in the CNS. Immune activation is often considered a dynamic process and may change throughout the course of the illness; therefore, a longitudinal study would have been preferred for a cross-sectional investigation. Finally, the present data obtained using murine models may imperfectly predict efficacy in humans. Our conclusions could therefore be strengthened by repeating the analyses using actual patient samples from an ALS clinic. Larger sample sizes are preferred, as this would increase the statistical power of the analysis, and hence improve the capacity to detect smaller phenotypes.

STAR★METHODS

Detailed methods are provided in the online version of this paper and include the following:

- KEY RESOURCES TABLE
- RESOURCE AVAILABILITY
  - Lead contact
  - Materials availability
  - Data and code availability
- EXPERIMENTAL MODEL AND SUBJECT DETAILS
  - Animals and experimental procedures
- METHOD DETAILS
  - Motor function test
  - Cell lines, cell culture, and transfection conditions
  - Immunopanning of murine primary neuronal and non-neuronal cells and culture conditions
  - Generation of CRISPR-Cas9-deficient cell lines
  - Mitochondria DNA subcellular fractionation, depletion, and membrane potential assay
  - ELISA, immunoblotting, and antibodies
  - Immunoprecipitation
  - Immunohistochemistry and histochemical staining
  - Confocal microscopy imaging
  - Crystal violet, cell viability and luciferase reporter assay
  - RNA isolation and quantitative RT-PCR
  - NanoString analysis
  - Flow cytometry analysis
- QUANTIFICATION AND STATISTICAL ANALYSIS

SUPPLEMENTAL INFORMATION

Supplemental information can be found online at https://doi.org/10.1016/j.isci.2022.104404.

ACKNOWLEDGMENTS

We thank Tomomi Furihata (Tokyo University of Pharmacy and Life Sciences, Japan), Neil Cashman (University of British Columbia, Canada), Takashi Fujita (Kyoto University, Japan), David Alvarez-Carbonell (Case Western Reserve University, USA), Christine Vande Velde (Université deMontréal, Canada), Leigh Anne Swayne (University of Victoria, Canada), and Nelson O. Gekara (Stockholm University, Sweden) for kindly providing valuable materials. H.Y.T. (XMUMRF/2020-C5/ITCM/0003) and K.Y.Y. (XMUMRF/2018-C2/ILAB/0001) is supported by a research grant from Xiamen University Malaysia. T.F. is supported by funding from the Japan Society for the Promotion of Science Kakenhi (#19K07214). Y.C.X is the recipient of Canadian Institutes of Health Research Doctoral Fellowship. Y.C.X. are recipients of Four-Year Doctoral Fellowships from University of British Columbia. H.L. is the recipient of fellowship from VIROGIN Biotech through Mitacs-Accelerate program.

AUTHOR CONTRIBUTIONS

Conceptualization and developed research plan: H.Y.T., Y.K.Y., and C.S.N.; Methodology and Investigation: H.Y.T, Y.K.Y., Y.C.X., H.L., T.F., and C.S.N.; Intellectual input: E.M.S.; Manuscript preparation, writing, review, and editing: H.Y.T., Y.K.Y., E.M.S., and C.S.N.

DECLARATION OF INTERESTS

The authors declared that the study was conducted in the absence of any commercial relationships that could be construed as a potential conflict of interest. The funders had no role in the study design, data collection and analysis, decision to publish, or preparation of the manuscript.

Received: September 29, 2021
Revised: February 22, 2022
Accepted: May 10, 2022
Published: June 17, 2022

REFERENCES

Ablasser, A., Schmid-Burgk, J.L., Hemmerling, I., Horvath, G.L., Schmidt, T., Latz, E., and Hornung, V. (2013). Cell intrinsic immunity spreads to bystander cells via the intercellular transfer of cGAMP. Nature *503*, 530–534. https://doi.org/10.1038/nature12640.

Albalawi, F., Lu, W., Beckel, J.M., Lim, J.C., McCaughey, S.A., and Mitchell, C.H. (2017). The P2X7 receptor primes IL-1β and the NLRP3 inflammasome in astrocytes exposed to mechanical strain. Front. Cell Neurosci. *11*, 227. https://doi.org/10.3389/fncel.2017.00227.

Almine, J.F., O'Hare, C.A.J., Dunphy, G., Haga, I.R., Naik, R.J., Atrih, A., Connolly, D.J., Taylor, J., Kelsall, I.R., Bowie, A.G., et al. (2017). IFI16 and cGAS cooperate in the activation of STING during DNA sensing in human keratinocytes. Nat. Commun. *8*, 14392. https://doi.org/10.1038/ncomms14392.

Barber, G.N. (2015). STING: infection, inflammation and cancer. Nat. Rev. Immunol. *15*, 760–770. https://doi.org/10.1038/nri3921.

Beers, D.R., Henkel, J.S., Xiao, Q., Zhao, W., Wang, J., Yen, A.A., Siklos, L., McKercher, S.R., and Appel, S.H. (2006). Wild-type microglia extend survival in PU.1 knockout mice with familial amyotrophic lateral sclerosis. Proc. Natl. Acad. Sci. U S A *103*, 16021–16026. https://doi.org/10.1073/pnas.0607423103.

Boillée, S., Yamanaka, K., Lobsiger, C.S., Copeland, N.G., Jenkins, N.A., Kassiotis, G., Kollias, G., and Cleveland, D.W. (2006). Onset and progression in inherited ALS determined by motor neurons and microglia. Science *312*, 1389–1392. https://doi.org/10.1126/science.1123511.

Brenner, D., Sieverding, K., Bruno, C., Lüningschrör, P., Buck, E., Mungwa, S., Fischer, L., Brockmann, S.J., Ulmer, J., Bliederhäuser, C., et al. (2019). Heterozygous Tbk1 loss has opposing effects in early and late stages of ALS in mice. J. Exp. Med. *216*, 267–278. https://doi.org/10.1084/jem.20180729.

Brubaker, S.W., Gauthier, A.E., Mills, E.W., Ingolia, N.T., and Kagan, J.C. (2014). A bicistronic MAVS transcript highlights a class of truncated variants in antiviral immunity. Cell *156*, 800–811. https://doi.org/10.1016/j.cell.2014.01.021.

Bruijn, L.I., Becher, M.W., Lee, M.K., Anderson, K.L., Jenkins, N.A., Copeland, N.G., Sisodia, S.S., Rothstein, J.D., Borchelt, D.R., Price, D.L., and Cleveland, D.W. (1997). ALS-linked SOD1 mutant G85R mediates damage to astrocytes and promotes rapidly progressive disease with SOD1-containing inclusions. Neuron *18*, 327–338. https://doi.org/10.1016/s0896-6273(00)80272-x.

Bruijn, L.I., Houseweart, M.K., Kato, S., Anderson, K.L., Anderson, S.D., Ohama, E., Reaume, A.G., Scott, R.W., and Cleveland, D.W. (1998). Aggregation and motor neuron toxicity of an ALS-linked SOD1 mutant independent from wild-type SOD1. Science *281*, 1851–1854. https://doi.org/10.1126/science.281.5384.1851.

Burdette, D.L., Monroe, K.M., Sotelo-Troha, K., Iwig, J.S., Eckert, B., Hyodo, M., Hayakawa, Y., and Vance, R.E. (2011). STING is a direct innate immune sensor of cyclic di-GMP. Nature *478*, 515–518. https://doi.org/10.1038/nature10429.

Casas, C., Herrando-Grabulosa, M., Manzano, R., Mancuso, R., Osta, R., and Navarro, X. (2013). Early presymptomatic cholinergic dysfunction in a murine model of amyotrophic lateral sclerosis. Brain Behav. *3*, 145–158. https://doi.org/10.1002/brb3.104.

Cashman, N.R., Durham, H.D., Blusztajn, J.K., Oda, K., Tabira, T., Shaw, I.T., Dahrouge, S., and Antel, J.P. (1992). Neuroblastoma × spinal cord (NSC) hybrid cell lines resemble developing motor neurons. Dev. Dyn. *194*, 209–221. https://doi.org/10.1002/aja.1001940306.

Chen, S., Sayana, P., Zhang, X., and Le, W. (2013). Genetics of amyotrophic lateral sclerosis: an update. Mol. Neurodegener. *8*, 28. https://doi.org/10.1186/1750-1326-8-28.

Cheng, Q., Yang, Y., and Gao, J. (2020). Infectivity of human coronavirus in the brain. EBioMedicine *56*, 102799. https://doi.org/10.1016/j.ebiom.2020.102799.

Chiò, A., Logroscino, G., Traynor, B.J., Collins, J., Simeone, J.C., Goldstein, L.A., and White, L.A. (2013). Global epidemiology of amyotrophic lateral sclerosis: a systematic review of the published literature. Neuroepidemiology *41*, 118–130. https://doi.org/10.1159/000351153.

Chiò, A., Mazzini, L., D'Alfonso, S., Corrado, L., Canosa, A., Moglia, C., Manera, U., Bersano, E., Brunetti, M., Barberis, M., et al. (2018). The multistep hypothesis of ALS revisited: the role of genetic mutations. Neurology *91*, e635–e642. https://doi.org/10.1212/WNL.0000000000005996.

Chui, R., and Dorovini-Zis, K. (2010). Regulation of CCL2 and CCL3 expression in human brain endothelial cells by cytokines and lipopolysaccharide. J. Neuroinflammation *7*, 1. https://doi.org/10.1186/1742-2094-7-1.

Cirulli, E.T., Lasseigne, B.N., Petrovski, S., Sapp, P.C., Dion, P.A., Leblond, C.S., Couthouis, J., Lu, Y.-F., Wang, Q., Krueger, B.J., et al. (2015). Exome sequencing in amyotrophic lateral sclerosis identifies risk genes and pathways. Science *347*, 1436–1441. https://doi.org/10.1126/science.aaa3650.

Crowl, J.T., Gray, E.E., Pestal, K., Volkman, H.E., and Stetson, D.B. (2017). Intracellular nucleic acid detection in autoimmunity. Annu. Rev. Immunol. *35*, 313–336. https://doi.org/10.1146/annurev-immunol-051116-052331.

Cui, R., Tuo, M., Li, P., and Zhou, C. (2018). Association between TBK1 mutations and risk of amyotrophic lateral sclerosis/frontotemporal dementia spectrum: a meta-analysis. Neurol. Sci. *39*, 811–820. https://doi.org/10.1007/s10072-018-3246-0.

Du, M., and Chen, Z.J. (2018). DNA-induced liquid phase condensation of cGAS activates innate immune signaling. Science *361*, 704–709. https://doi.org/10.1126/science.aat1022.

Dugas, J.C., Mandemakers, W., Rogers, M., Ibrahim, A., Daneman, R., and Barres, B.A. (2008). A novel purification method for CNS projection neurons leads to the identification of brain vascular cells as a source of trophic support for corticospinal motor neurons. J. Neurosci. *28*, 8294–8305. https://doi.org/10.1523/JNEUROSCI.2010-08.2008.

Endo, F., Komine, O., and Yamanaka, K. (2016). Neuroinflammation in motor neuron disease. Clin. Exp. Neuroimmunol. *7*, 126–138. https://doi.org/10.1111/cen3.12309.

Foo, L.C. (2013). Purification of rat and mouse astrocytes by immunopanning. Cold Spring Harb. Protoc. *2013*. pdb.prot074211–pdb.prot074432. https://doi.org/10.1101/pdb.prot074211.

Freischmidt, A., Wieland, T., Richter, B., Ruf, W., Schaeffer, V., Müller, K., Marroquin, N., Nordin, F., Hübers, A., Weydt, P., et al. (2015). Haploinsufficiency of TBK1 causes familial ALS and fronto-temporal dementia. Nat. Neurosci. *18*, 631–636. https://doi.org/10.1038/nn.4000.

Furihata, T., Ito, R., Kamiichi, A., Saito, K., and Chiba, K. (2016). Establishment and characterization of a new conditionally immortalized human astrocyte cell line. J. Neurochem. *136*, 92–105. https://doi.org/10.1111/jnc.13358.

Gal, J., Kuang, L., Barnett, K.R., Zhu, B.Z., Shissler, S.C., Korotkov, K.V., Hayward, L.J., Kasarskis, E.J., and Zhu, H. (2016). ALS mutant SOD1 interacts

with G3BP1 and affects stress granule dynamics. Acta Neuropathol. *132*, 563–576. https://doi.org/10.1007/s00401-016-1601-x.

Gao, P., Ascano, M., Wu, Y., Barchet, W., Gaffney, B.L., Zillinger, T., Serganov, A.A., Liu, Y., Jones, R.A., Hartmann, G., et al. (2013). Cyclic [G(2',5')pA(3',5')p] is the metazoan second messenger produced by DNA-activated cyclic GMP-AMP synthase. Cell *153*, 1094–1107. https://doi.org/10.1016/j.cell.2013.04.046.

Garcia-Mesa, Y., Jay, T.R., Checkley, M.A., Luttge, B., Dobrowolski, C., Valadkhan, S., Landreth, G.E., Karn, J., and Alvarez-Carbonell, D. (2017). Immortalization of primary microglia: a new platform to study HIV regulation in the central nervous system. J. Neurovirol. *23*, 47–66. https://doi.org/10.1007/s13365-016-0499-3.

Haag, S.M., Gulen, M.F., Reymond, L., Gibelin, A., Abrami, L., Decout, A., Heymann, M., van der Goot, F.G., Turcatti, G., Behrendt, R., and Ablasser, A. (2018). Targeting STING with covalent small-molecule inhibitors. Nature *559*, 269–273. https://doi.org/10.1038/s41586-018-0287-8.

Hammitt, L.L., Kazungu, S., Welch, S., Bett, A., Onyango, C.O., Gunson, R.N., Scott, J.A.G., and Nokes, D.J. (2011). Added value of an oropharyngeal swab in detection of viruses in children hospitalized with lower respiratory tract infection. J. Clin. Microbiol. *49*, 2318–2320. https://doi.org/10.1128/JCM.02605-10.

Hanisch, U.-K., and Kettenmann, H. (2007). Microglia: active sensor and versatile effector cells in the normal and pathologic brain. Nat. Neurosci. *10*, 1387–1394. https://doi.org/10.1038/nn1997.

Hardiman, O., Al-Chalabi, A., Chio, A., Corr, E.M., Logroscino, G., Robberecht, W., Shaw, P.J., Simmons, Z., and van den Berg, L.H. (2017). Amyotrophic lateral sclerosis. Nat. Rev. Dis. Primers *3*, 17071. https://doi.org/10.1038/nrdp.2017.71.

Harraz, M.M., Marden, J.J., Zhou, W., Zhang, Y., Williams, A., Sharov, V.S., Nelson, K., Luo, M., Paulson, H., Schöneich, C., and Engelhardt, J.F. (2008). SOD1 mutations disrupt redox-sensitive Rac regulation of NADPH oxidase in a familial ALS model. J. Clin. Invest. *118*, 659–670. https://doi.org/10.1172/JCI34060.

Härtlova, A., Erttmann, S.F., Raffi, F.A., Schmalz, A.M., Resch, U., Anugula, S., Lienenklaus, S., Nilsson, L.M., Kröger, A., Nilsson, J.A., et al. (2015). DNA damage primes the type I interferon system via the cytosolic DNA sensor STING to promote anti-microbial innate immunity. Immunity *42*, 332–343. https://doi.org/10.1016/j.immuni.2015.01.012.

Hashiguchi, K., and Zhang-Akiyama, Q.-M. (2009). Establishment of human cell lines lacking mitochondrial DNA. Methods Mol. Biol. *554*, 383–391. https://doi.org/10.1007/978-1-59745-521-3_23.

Hong, S., Hwang, I., Gim, E., Yang, J., Park, S., Yoon, S.-H., Lee, W.-W., and Yu, J.-W. (2019). Brefeldin A-sensitive ER-Golgi vesicle trafficking contributes to NLRP3-dependent caspase-1 activation. FASEB J. *33*, 4547–4558. https://doi.org/10.1096/fj.201801585R.

Hou, F., Sun, L., Zheng, H., Skaug, B., Jiang, Q.-X., and Chen, Z.J. (2011). MAVS forms functional prion-like aggregates to activate and propagate antiviral innate immune response. Cell *146*, 448–461. https://doi.org/10.1016/j.cell.2011.06.041.

Jaarsma, D., Haasdijk, E.D., Grashorn, J.A., Hawkins, R., van Duijn, W., Verspaget, H.W., London, J., and Holstege, J.C. (2000). Human Cu/Zn superoxide dismutase (SOD1) overexpression in mice causes mitochondrial vacuolization, axonal degeneration, and premature motoneuron death and accelerates motoneuron disease in mice expressing a familial amyotrophic lateral sclerosis mutant SOD1. Neurobiol. Dis. *7*, 623–643. https://doi.org/10.1006/nbdi.2000.0299.

Jaarsma, D., Rognoni, F., van Duijn, W., Verspaget, H.W., Haasdijk, E.D., and Holstege, J.C. (2001). CuZn superoxide dismutase (SOD1) accumulates in vacuolated mitochondria in transgenic mice expressing amyotrophic lateral sclerosis-linked SOD1 mutations. Acta Neuropathol. *102*, 293–305. https://doi.org/10.1007/s004010100399.

Jacomy, H., Fragoso, G., Almazan, G., Mushynski, W.E., and Talbot, P.J. (2006). Human coronavirus OC43 infection induces chronic encephalitis leading to disabilities in BALB/C mice. Virology *349*, 335–346. https://doi.org/10.1016/j.virol.2006.01.049.

Jiang, H., Xue, X., Panda, S., Kawale, A., Hooy, R.M., Liang, F., Sohn, J., Sung, P., and Gekara, N.O. (2019). Chromatin-bound cGAS is an inhibitor of DNA repair and hence accelerates genome destabilization and cell death. EMBO J. *38*, e102718. https://doi.org/10.15252/embj.2019102718.

Kai, Y., Takamatsu, C., Tokuda, K., Okamoto, M., Irita, K., and Takahashi, S. (2006). Rapid and random turnover of mitochondrial DNA in rat hepatocytes of primary culture. Mitochondrion *6*, 299–304. https://doi.org/10.1016/j.mito.2006.10.002.

Kao, L.-P., Ovchinnikov, D., and Wolvetang, E. (2012). The effect of ethidium bromide and chloramphenicol on mitochondrial biogenesis in primary human fibroblasts. Toxicol. Appl. Pharmacol. *261*, 42–49. https://doi.org/10.1016/j.taap.2012.03.009.

Kasereka, M.C., and Hawkes, M.T. (2021). Neuroinvasive potential of human coronavirus OC43: case report of fatal encephalitis in an immunocompromised host. J. Neurovirol. *27*, 340–344. https://doi.org/10.1007/s13365-020-00926-0.

Kielian, T., Barry, B., and Hickey, W.F. (2001). CXC chemokine receptor-2 ligands are required for neutrophil-mediated host defense in experimental brain Abscesses[1]. J. Immunol. *166*, 4634–4643. https://doi.org/10.4049/jimmunol.166.7.4634.

Kitamura, K., Ito, R., Umehara, K., Morio, H., Saito, K., Suzuki, S., Hashimoto, M., Saito, Y., Anzai, N., Akita, H., et al. (2018). Differentiated HASTR/ci35 cells: a promising in vitro human astrocyte model for facilitating CNS drug development studies. J. Pharmacol. Sci. *137*, 350–358. https://doi.org/10.1016/j.jphs.2018.06.013.

Krasemann, S., Madore, C., Cialic, R., Baufeld, C., Calcagno, N., El Fatimy, R., Beckers, L., O'Loughlin, E., Xu, Y., Fanek, Z., et al. (2017). The TREM2-APOE pathway drives the transcriptional phenotype of dysfunctional microglia in neurodegenerative diseases. Immunity *47*, 566–581.e9. https://doi.org/10.1016/j.immuni.2017.08.008.

Langereis, M.A., Rabouw, H.H., Holwerda, M., Visser, L.J., and van Kuppeveld, F.J.M. (2015). Knockout of cGAS and STING rescues virus infection of plasmid DNA-transfected cells. J. Virol. *89*, 11169–11173. https://doi.org/10.1128/JVI.01781-15.

Lee, D.-Y., Jeon, G.S., and Sung, J.-J. (2020). ALS-Linked Mutant SOD1 associates with TIA-1 and alters stress granule dynamics. Neurochem. Res. *45*, 2884–2893. https://doi.org/10.1007/s11064-020-03137-5.

Lee, K.-G., Kim, S.Y., Kui, L., Voon, D.C.-C., Mauduit, M., Bist, P., Bi, X., Pereira, N.A., Liu, C., Sukumaran, B., et al. (2015). Bruton's tyrosine kinase phosphorylates DDX41 and activates its binding of dsDNA and STING to initiate type 1 interferon response. Cell Rep. *10*, 1055–1065. https://doi.org/10.1016/j.celrep.2015.01.039.

Lee-Kirsch, M.A. (2017). The type I interferonopathies. Annu. Rev. Med. *68*, 297–315. https://doi.org/10.1146/annurev-med-050715-104506.

Lehmann, M.H., Torres-Domínguez, L.E., Price, P.J.R., Brandmüller, C., Kirschning, C.J., and Sutter, G. (2016). CCL2 expression is mediated by type I IFN receptor and recruits NK and T cells to the lung during MVA infection. J. Leukoc. Biol. *99*, 1057–1064. https://doi.org/10.1189/jlb.4MA0815-376RR.

Liao, B., Zhao, W., Beers, D.R., Henkel, J.S., and Appel, S.H. (2012). Transformation from a neuroprotective to a neurotoxic microglial phenotype in a mouse model of ALS. Exp. Neurol. *237*, 147–152. https://doi.org/10.1016/j.expneurol.2012.06.011.

Lohman, A.W., Leskov, I.L., Butcher, J.T., Johnstone, S.R., Stokes, T.A., Begandt, D., DeLalio, L.J., Best, A.K., Penuela, S., Leitinger, N., et al. (2015). Pannexin 1 channels regulate leukocyte emigration through the venous endothelium during acute inflammation. Nat. Commun. *6*, 7965. https://doi.org/10.1038/ncomms8965.

Makarenkova, H.P., Shah, S.B., and Shestopalov, V.I. (2018). The two faces of pannexins: new roles in inflammation and repair. J. Inflamm. Res. *11*, 273–288. https://doi.org/10.2147/JIR.S128401.

Mankan, A.K., Schmidt, T., Chauhan, D., Goldeck, M., Höning, K., Gaidt, M., Kubarenko, A.V., Andreeva, L., Hopfner, K.-P., and Hornung, V. (2014). Cytosolic RNA:DNA hybrids activate the cGAS-STING axis. EMBO J. *33*, 2937–2946. https://doi.org/10.15252/embj.201488726.

Mattei, L.M., Cotmore, S.F., Li, L., Tattersall, P., and Iwasaki, A. (2013). Toll-like receptor 9 in plasmacytoid dendritic cells fails to detect parvoviruses. J. Virol. *87*, 3605–3608. https://doi.org/10.1128/JVI.03155-12.

McCauley, M.E., O'Rourke, J.G., Yáñez, A., Markman, J.L., Ho, R., Wang, X., Chen, S., Lall, D., Jin, M., Muhammad, A.K.M.G., et al. (2020).

C9orf72 in myeloid cells suppresses STING-induced inflammation. Nature *585*, 96–101. https://doi.org/10.1038/s41586-020-2625-x.

McLaurin, J., Trudel, G.C., Shaw, I.T., Antel, J.P., and Cashman, N.R. (1995). A human glial hybrid cell line differentially expressing genes subserving oligodendrocyte and astrocyte phenotype. J. Neurobiol. *26*, 283–293. https://doi.org/10.1002/neu.480260212.

Mejzini, R., Flynn, L.L., Pitout, I.L., Fletcher, S., Wilton, S.D., and Akkari, P.A. (2019). ALS genetics, mechanisms, and therapeutics: where are we now? Front. Neurosci. *13*, 1310. https://doi.org/10.3389/fnins.2019.01310.

Morfopoulou, S., Brown, J.R., Davies, E.G., Anderson, G., Virasami, A., Qasim, W., Chong, W.K., Hubank, M., Plagnol, V., Desforges, M., et al. (2016). Human coronavirus OC43 associated with fatal encephalitis. N. Engl. J. Med. *375*, 497–498. https://doi.org/10.1056/NEJMc1509458.

Mori, M., Yoneyama, M., Ito, T., Takahashi, K., Inagaki, F., and Fujita, T. (2004). Identification of Ser-386 of interferon regulatory factor 3 as critical target for inducible phosphorylation that determines activation. J. Biol. Chem. *279*, 9698–9702. https://doi.org/10.1074/jbc.M310616200.

Narita, R., Takahasi, K., Murakami, E., Hirano, E., Yamamoto, S.P., Yoneyama, M., Kato, H., and Fujita, T. (2014). A novel function of human Pumilio proteins in cytoplasmic sensing of viral infection. PLoS Pathog. *10*, e1004417. https://doi.org/10.1371/journal.ppat.1004417.

Nelson, I., Hanna, M.G., Wood, N.W., and Harding, A.E. (1997). Depletion of mitochondrial DNA by ddC in untransformed human cell lines. Somat. Cell Mol. Genet. *23*, 287–290. https://doi.org/10.1007/BF02674419.

Ng, C.S., Jogi, M., Yoo, J.-S., Onomoto, K., Koike, S., Iwasaki, T., Yoneyama, M., Kato, H., and Fujita, T. (2013). Encephalomyocarditis virus disrupts stress granules, the critical platform for triggering antiviral innate immune responses. J. Virol. *87*, 9511–9522. https://doi.org/10.1128/JVI.03248-12.

Ng, C.S., Kasumba, D.M., Fujita, T., and Luo, H. (2020). Spatio-temporal characterization of the antiviral activity of the XRN1-DCP1/2 aggregation against cytoplasmic RNA viruses to prevent cell death. Cell Death Differ. *27*, 2363–2382. https://doi.org/10.1038/s41418-020-0509-0.

Nilsson, A., Edner, N., Albert, J., and Ternhag, A. (2020). Fatal encephalitis associated with coronavirus OC43 in an immunocompromised child. Infect. Dis. (Lond) *52*, 419–422. https://doi.org/10.1080/23744235.2020.1729403.

Onoguchi, K., Onomoto, K., Takamatsu, S., Jogi, M., Takemura, A., Morimoto, S., Julkunen, I., Namiki, H., Yoneyama, M., and Fujita, T. (2010). Virus-infection or 5'ppp-RNA activates antiviral signal through redistribution of IPS-1 mediated by MFN1. PLoS Pathog. *6*, e1001012. https://doi.org/10.1371/journal.ppat.1001012.

Onomoto, K., Jogi, M., Yoo, J.-S., Narita, R., Morimoto, S., Takemura, A., Sambhara, S., Kawaguchi, A., Osari, S., Nagata, K., et al. (2012). Critical role of an antiviral stress granule containing RIG-I and PKR in viral detection and innate immunity. PLoS One *7*, e43031. https://doi.org/10.1371/journal.pone.0043031.

Pablo, J., Banack, S.A., Cox, P.A., Johnson, T.E., Papapetropoulos, S., Bradley, W.G., Buck, A., and Mash, D.C. (2009). Cyanobacterial neurotoxin BMAA in ALS and Alzheimer's disease. Acta Neurol. Scand. *120*, 216–225. https://doi.org/10.1111/j.1600-0404.2008.01150.x.

Palomino-Segura, M., Perez, L., Farsakoglu, Y., Virgilio, T., Latino, I., D'Antuono, R., Chatziandreou, N., Pizzagalli, D.U., Wang, G., García-Sastre, A., et al. (2019). Protection against influenza infection requires early recognition by inflammatory dendritic cells through C-type lectin receptor SIGN-R1. Nat. Microbiol. *4*, 1930–1940. https://doi.org/10.1038/s41564-019-0506-6.

Papadeas, S.T., Kraig, S.E., O'Banion, C., Lepore, A.C., and Maragakis, N.J. (2011). Astrocytes carrying the superoxide dismutase 1 (SOD1G93A) mutation induce wild-type motor neuron degeneration in vivo. Proc. Natl. Acad. Sci. U S A *108*, 17803–17808. https://doi.org/10.1073/pnas.1103141108.

Parzych, K., Zetterqvist, A.V., Wright, W.R., Kirkby, N.S., Mitchell, J.A., and Paul-Clark, M.J. (2017). Differential role of pannexin-1/ATP/P2X7 axis in IL-1β release by human monocytes. FASEB J. *31*, 2439–2445. https://doi.org/10.1096/fj.201600256.

Pedrini, S., Sau, D., Guareschi, S., Bogush, M., Brown, R.H., Naniche, N., Kia, A., Trotti, D., and Pasinelli, P. (2010). ALS-linked mutant SOD1 damages mitochondria by promoting conformational changes in Bcl-2. Hum. Mol. Genet. *19*, 2974–2986. https://doi.org/10.1093/hmg/ddq202.

Pokrishevsky, E., Hong, R.H., Mackenzie, I.R., and Cashman, N.R. (2017). Spinal cord homogenates from SOD1 familial amyotrophic lateral sclerosis induce SOD1 aggregation in living cells. PLoS One *12*, e0184384. https://doi.org/10.1371/journal.pone.0184384.

Qi, N., Shi, Y., Zhang, R., Zhu, W., Yuan, B., Li, X., Wang, C., Zhang, X., and Hou, F. (2017). Multiple truncated isoforms of MAVS prevent its spontaneous aggregation in antiviral innate immune signalling. Nat. Commun. *8*, 15676. https://doi.org/10.1038/ncomms15676.

Ringer, C., Weihe, E., and Schütz, B. (2017). SOD1G93A mutant mice develop a neuroinflammation-independent dendropathy in excitatory neuronal subsets of the olfactory bulb and retina. J. Neuropathol. Exp. Neurol. *76*, 769–778. https://doi.org/10.1093/jnen/nlx057.

Rosen, D.R., Siddique, T., Patterson, D., Figlewicz, D.A., Sapp, P., Hentati, A., Donaldson, D., Goto, J., O'Regan, J.P., Deng, H.X., et al. (1993). Mutations in Cu/Zn superoxide dismutase gene are associated with familial amyotrophic lateral sclerosis. Nature *362*, 59–62. https://doi.org/10.1038/362059a0.

Roy, E.R., Wang, B., Wan, Y.w., Chiu, G., Cole, A., Yin, Z., Propson, N.E., Xu, Y., Jankowsky, J.L., Liu, Z., et al. (2020). Type I interferon response drives neuroinflammation and synapse loss in Alzheimer disease. J. Clin. Invest. *130*, 1912–1930. https://doi.org/10.1172/jci133737.

Saberi, S., Stauffer, J.E., Schulte, D.J., and Ravits, J. (2015). Neuropathology of amyotrophic lateral sclerosis and its variants. Neurol. Clin. *33*, 855–876. https://doi.org/10.1016/j.ncl.2015.07.012.

Sarkar, S., Malovic, E., Plante, B., Zenitsky, G., Jin, H., Anantharam, V., Kanthasamy, A., and Kanthasamy, A.G. (2017). Rapid and refined CD11b magnetic isolation of primary microglia with enhanced purity and versatility. J. Vis. Exp. *122*, 55364. https://doi.org/10.3791/55364.

Scemes, E., Suadicani, S.O., Dahl, G., and Spray, D.C. (2007). Connexin and pannexin mediated cell-cell communication. Neuron Glia Biol. *3*, 199–208. https://doi.org/10.1017/S1740925X08000069.

Semmler, S., Gagné, M., Garg, P., Pickles, S.R., Baudouin, C., Hamon-Keromen, E., Destroismaisons, L., Khalfallah, Y., Chaineau, M., Caron, E., et al. (2020). TNF receptor-associated factor 6 interacts with ALS-linked misfolded superoxide dismutase 1 and promotes aggregation. J. Biol. Chem. *295*, 3808–3825. https://doi.org/10.1074/jbc.RA119.011215.

Semple, B.D., Kossmann, T., and Morganti-Kossmann, M.C. (2010). Role of chemokines in CNS health and pathology: a focus on the CCL2/CCR2 and CXCL8/CXCR2 networks. J. Cereb. Blood Flow Metab. *30*, 459–473. https://doi.org/10.1038/jcbfm.2009.240.

Siu, R.C.F., Smirnova, E., Brown, C.A., Zoidl, C., Spray, D.C., Donaldson, L.W., and Zoidl, G. (2016). Structural and functional consequences of connexin 36 (Cx36) interaction with calmodulin. Front. Mol. Neurosci. *9*, 120. https://doi.org/10.3389/fnmol.2016.00120.

Sliter, D.A., Martinez, J., Hao, L., Chen, X., Sun, N., Fischer, T.D., Burman, J.L., Li, Y., Zhang, Z., Narendra, D.P., et al. (2018). Parkin and PINK1 mitigate STING-induced inflammation. Nature *561*, 258–262. https://doi.org/10.1038/s41586-018-0448-9.

Stavrou, S., Aguilera, A.N., Blouch, K., and Ross, S.R. (2018). DDX41 recognizes RNA/DNA retroviral reverse transcripts and is critical for in vivo control of murine leukemia virus infection. MBio *9*, e00923–e01018. https://doi.org/10.1128/mBio.00923-18.

Stetson, D.B., Ko, J.S., Heidmann, T., and Medzhitov, R. (2008). Trex1 prevents cell-intrinsic initiation of autoimmunity. Cell *134*, 587–598. https://doi.org/10.1016/j.cell.2008.06.032.

Stetson, D.B., and Medzhitov, R. (2006). Type I interferons in host defense. Immunity *25*, 373–381. https://doi.org/10.1016/j.immuni.2006.08.007.

Sun, B., Sundström, K.B., Chew, J.J., Bist, P., Gan, E.S., Tan, H.C., Goh, K.C., Chawla, T., Tang, C.K., and Ooi, E.E. (2017). Dengue virus activates cGAS through the release of mitochondrial DNA. Sci. Rep. *7*, 3594. https://doi.org/10.1038/s41598-017-03932-1.

Sun, L., Wu, J., Du, F., Chen, X., and Chen, Z.J. (2013). Cyclic GMP-AMP synthase is a cytosolic DNA sensor that activates the type I interferon pathway. Science *339*, 786–791. https://doi.org/10.1126/science.1232458.

Takaoka, A., Wang, Z., Choi, M.K., Yanai, H., Negishi, H., Ban, T., Lu, Y., Miyagishi, M.,

Kodama, T., Honda, K., et al. (2007). DAI (DLM-1/ZBP1) is a cytosolic DNA sensor and an activator of innate immune response. Nature *448*, 501–505. https://doi.org/10.1038/nature06013.

Taylor, J.P., Brown, R.H., and Cleveland, D.W. (2016). Decoding ALS: from genes to mechanism. Nature *539*, 197–206. https://doi.org/10.1038/nature20413.

Tiwari, A., Xu, Z., and Hayward, L.J. (2005). Aberrantly increased hydrophobicity shared by mutants of Cu, Zn-superoxide dismutase in familial amyotrophic lateral sclerosis. J. Biol. Chem. *280*, 29771–29779. https://doi.org/10.1074/jbc.M504039200.

Turner, M.R., Cagnin, A., Turkheimer, F.E., Miller, C.C.J., Shaw, C.E., Brooks, D.J., Leigh, P.N., and Banati, R.B. (2004). Evidence of widespread cerebral microglial activation in amyotrophic lateral sclerosis: an [11C](R)-PK11195 positron emission tomography study. Neurobiol. Dis. *15*, 601–609. https://doi.org/10.1016/j.nbd.2003.12.012.

Turner, M.R., and Swash, M. (2015). The expanding syndrome of amyotrophic lateral sclerosis: a clinical and molecular odyssey. J. Neurol. Neurosurg. Psychiat. *86*, 667–673. https://doi.org/10.1136/jnnp-2014-308946.

Unterholzner, L., Keating, S.E., Baran, M., Horan, K.A., Jensen, S.B., Sharma, S., Sirois, C.M., Jin, T., Latz, E., Xiao, T.S., et al. (2010). IFI16 is an innate immune sensor for intracellular DNA. Nat. Immunol. *11*, 997–1004. https://doi.org/10.1038/ni.1932.

Van Den Bosch, L. (2011). Genetic rodent models of amyotrophic lateral sclerosis. J. Biomed. Biotechnol. *2011*, 1–11. https://doi.org/10.1155/2011/348765.

Vincent, J., Adura, C., Gao, P., Luz, A., Lama, L., Asano, Y., Okamoto, R., Imaeda, T., Aida, J., Rothamel, K., et al. (2017). Small molecule inhibition of cGAS reduces interferon expression in primary macrophages from autoimmune mice. Nat. Commun. *8*, 750. https://doi.org/10.1038/s41467-017-00833-9.

Vucic, S., Westeneng, H.-J., Al-Chalabi, A., Van Den Berg, L.H., Talman, P., and Kiernan, M.C. (2019). Amyotrophic lateral sclerosis as a multi-step process: an Australia population study. Amyotroph. Lateral Scler. Frontotemporal Degener. *20*, 532–537. https://doi.org/10.1080/21678421.2018.1556697.

Wang, H., Xing, Y., Mao, L., Luo, Y., Kang, L., and Meng, G. (2013). Pannexin-1 influences peritoneal cavity cell population but is not involved in NLRP3 inflammasome activation. Protein Cell *4*, 259–265. https://doi.org/10.1007/s13238-013-2114-1.

Wang, R., Yang, B., and Zhang, D. (2011). Activation of interferon signaling pathways in spinal cord astrocytes from an ALS mouse model. Glia *59*, 946–958. https://doi.org/10.1002/glia.21167.

West, A.P., Khoury-Hanold, W., Staron, M., Tal, M.C., Pineda, C.M., Lang, S.M., Bestwick, M., Duguay, B.A., Raimundo, N., MacDuff, D.A., et al. (2015). Mitochondrial DNA stress primes the antiviral innate immune response. Nature *520*, 553–557. https://doi.org/10.1038/nature14156.

Wijesekera, L.C., and Nigel Leigh, P. (2009). Amyotrophic lateral sclerosis. Orphanet J. Rare Dis. *4*, 3. https://doi.org/10.1186/1750-1172-4-3.

Xue, Y.C., Ruller, C.M., Fung, G., Mohamud, Y., Deng, H., Liu, H., Zhang, J., Feuer, R., and Luo, H. (2018). Enteroviral infection leads to transactive response DNA-binding protein 43 pathology in vivo. Am. J. Pathol. *188*, 2853–2862. https://doi.org/10.1016/j.ajpath.2018.08.013.

Yamanaka, K., Chun, S.J., Boillee, S., Fujimori-Tonou, N., Yamashita, H., Gutmann, D.H., Takahashi, R., Misawa, H., and Cleveland, D.W. (2008). Astrocytes as determinants of disease progression in inherited amyotrophic lateral sclerosis. Nat. Neurosci. *11*, 251–253. https://doi.org/10.1038/nn2047.

Yamashita, S., and Ando, Y. (2015). Genotype-phenotype relationship in hereditary amyotrophic lateral sclerosis. Transl. Neurodegener. *4*, 13. https://doi.org/10.1186/s40035-015-0036-y.

Yang, Y., Delalio, L.J., Best, A.K., Macal, E., Milstein, J., Donnelly, I., Miller, A.M., McBride, M., Shu, X., Koval, M., et al. (2020). Endothelial pannexin 1 channels control inflammation by regulating intracellular calcium. J. Immunol. *204*, 2995–3007. https://doi.org/10.4049/jimmunol.1901089.

Yoneyama, M., Suhara, W., Fukuhara, Y., Fukuda, M., Nishida, E., and Fujita, T. (1998). Direct triggering of the type I interferon system by virus infection: activation of a transcription factor complex containing IRF-3 and CBP/p300. EMBO J. *17*, 1087–1095. https://doi.org/10.1093/emboj/17.4.1087.

Yoshihara, T., Ishigaki, S., Yamamoto, M., Liang, Y., Niwa, i., Takeuchi, H., Doyu, M., and Sobue, G. (2002). Differential expression of inflammation- and apoptosis-related genes in spinal cords of a mutant SOD1 transgenic mouse model of familial amyotrophic lateral sclerosis. J. Neurochem. *80*, 158–167. https://doi.org/10.1046/j.0022-3042.2001.00683.x.

Yu, C.-H., Davidson, S., Harapas, C.R., Hilton, J.B., Mlodzianoski, M.J., Laohamonthonkul, P., Louis, C., Low, R.R.J., Moecking, J., De Nardo, D., et al. (2020). TDP-43 triggers mitochondrial DNA release via mPTP to activate cGAS/STING in ALS. Cell *183*, 636–649.e18. https://doi.org/10.1016/j.cell.2020.09.020.

Yu, M., Shi, Y., Wei, X., Yang, Y., Zhou, Y., Hao, X., Zhang, N., and Niu, R. (2007). Depletion of mitochondrial DNA by ethidium bromide treatment inhibits the proliferation and tumorigenesis of T47D human breast cancer cells. Toxicol. Lett. *170*, 83–93. https://doi.org/10.1016/j.toxlet.2007.02.013.

Yuzefovych, L.V., Musiyenko, S.I., Wilson, G.L., and Rachek, L.I. (2013). Mitochondrial DNA damage and dysfunction, and oxidative stress are associated with endoplasmic reticulum stress, protein degradation and apoptosis in high fat diet-induced insulin resistance mice. PLoS One *8*, e54059. https://doi.org/10.1371/journal.pone.0054059.

Zhou, K.Q., Green, C.R., Bennet, L., Gunn, A.J., and Davidson, J.O. (2019). The role of connexin and pannexin channels in perinatal brain injury and inflammation. Front. Physiol. *10*, 141. https://doi.org/10.3389/fphys.2019.00141.

Zou, Z., Sun, J., Kang, Z., Wang, Y., Zhao, H., Zhu, K., and Wang, J. (2020). Tyrosine kinase receptors axl and MerTK mediate the beneficial effect of electroacupuncture in a cuprizone-induced demyelinating model. Evid. base Compl. Alternative Med. *2020*, 1–13. https://doi.org/10.1155/2020/3205176.

STAR★METHODS

KEY RESOURCES TABLE

REAGENT or RESOURCE	SOURCE	IDENTIFIER
Antibodies		
Rabbit anti-CX43	Cell Signaling Technology	Cat#3512S; RRID: AB_2294590
Rabbit monoclonal anti-VDAC (D73D12)	Cell Signaling Technology	Cat#4661; RRID: AB_10557420
Rabbit monoclonal anti-RIG-I (D14G6)	Cell Signaling Technology	Cat#3743; RRID: AB_2269233
Rabbit monoclonal anti-MDA5 (D74 × 10^4)	Cell Signaling Technology	Cat#5321; RRID: AB_10694490
Rabbit anti-SOD1	Cell Signaling Technology	Cat#2770; RRID: AB_2302392
Rabbit monoclonal anti-MAVS (D5A9E, H)	Cell Signaling Technology	Cat#24930; RRID: AB_2798889
Rodent specific anti-MAVS (Mouse/Rat)	Cell Signaling Technology	Cat#4983; RRID: AB_823566
Rabbit monoclonal anti-COX IV (3 × 10^{11})	Cell Signaling Technology	Cat#4850; RRID: AB_2085424
Rabbit monoclonal anti-STAT1 (D1K9Y)	Cell Signaling Technology	Cat#14994; RRID: AB_2737027
Rabbit monoclonal anti-STING (D2P2F)	Cell Signaling Technology	Cat#13647; RRID: AB_2732796
Rabbit monoclonal anti-TBK1/NAK (D1B4)	Cell Signaling Technology	Cat#3504; RRID: AB_2255663
Rabbit monoclonal anti-phoshoTBK1/NAK1 (Ser172, D52C2)	Cell Signaling Technology	Cat#5483; RRID: AB_10693472
Rabbit monoclonal anti-phospho-IRF3 (Ser396, 4D4G)	Cell Signaling Technology	Cat#4947; RRID: AB_823547
Mouse monoclonal anti-dsDNA [35I9 DNA]	Abcam	Cat#ab27156; RRID: AB_470907
Rabbit polyclonal anti-DDX41	ABclonal Inc.	Cat#A6576; RRID: AB_2767170
Rabbit polyclonal Lamin A/C [KO validated]	ABclonal Inc.	Cat#A0249; RRID: AB_2757062
Rabbit polyclonal anti-HSP60/HSPD1	ABclonal Inc.	Cat#A0969; RRID: AB_2757488
Rabbit polyclonal anti-IRF3 [KO validated]	ABclonal Inc.	Cat#A11118; RRID: AB_2861504
Rabbit polyclonal anti-PANX1	ABclonal Inc.	Cat#A13587; RRID: AB_2760449
Rabbit polyclonal anti-GJC1/CX45	ABclonal Inc.	Cat#A7053; RRID: AB_2767608
Rabbit polyclonal anti-cGAS	ABclonal Inc.	Cat#A8335; RRID: AB_2770305
Rabbit polyclonal anti-phospho-cGAS Y215	ABclonal Inc.	Cat#AP0946; RRID: N/A
Mouse monoclonal anti-FLAG (M2)	Sigma-Aldrich	Cat#F1804; RRID: AB_262044
Mouse monoclonal anti-O4	Sigma-Aldrich	Cat#O7139; RRID: AB_477662
Mouse monoclonal anti-CD45 (clone 30-F11)	BD Pharmingen	Cat#550539; RRID: AB_2174426
Sheep polyclonal anti-ITGB5	R&D Systems	Cat#AF3824; RRID: AB_1151977
Mouse monoclonal anti-L1, clone 324	Millipore Sigma	Cat#MAB5272; RRID: AB_2133200
Mouse monoclonal anti-DNA:RNA hybrid, clone S9.6	Millipore Sigma	Cat#MABE1095; RRID: AB_2861387
Mouse monoclonal anti-NK1.1	Thermo Fisher Scientific	Cat#MA1-70100; RRID: AB_2296673
Mouse monoclonal anti-NF-κB p65 (F-6)	Santa Cruz Biotechnology	Cat#sc-8008; RRID: AB_628017
Mouse monoclonal anti-mtTFA (F6)	Santa Cruz Biotechnology	Cat#sc-166965; RRID: AB_10610743
Mouse monoclonal anti-Pol II (A10)	Santa Cruz Biotechnology	Cat#sc-17798; RRID: AB_677355
Rabbit polyclonal anti-TOM20 (FL-145)	Santa Cruz Biotechnology	Cat#sc-11415; RRID: AB_2207533
Mouse monoclonal anti-GFAP	Santa Cruz Biotechnology	Cat#sc-33673; RRID: AB_627673
Mouse monoclonal anti-Iba1	Santa Cruz Biotechnology	Cat#sc-32725; RRID: AB_667733
Mouse monoclonal anti-CD4	Santa Cruz Biotechnology	Cat#sc-19641; RRID: AB_2009035
Mouse monoclonal anti-CD19	Santa Cruz Biotechnology	Cat#sc-; RRID: AB_667733
Mouse monoclonal anti-β-Actin (C4)	Santa Cruz Biotechnology	Cat#sc-47778; RRID: AB_2714189
Mouse monoclonal anti-β-tubulin (G8)	Santa Cruz Biotechnology	Cat#sc-55529; RRID: AB_2210962
Mouse monoclonal anti-CD68	Santa Cruz Biotechnology	Cat#sc-20060; RRID: AB_627158
Mouse monoclonal anti-VP1 Clone 31A2	Mediagnost	Cat#M47; RRID: N/A

(*Continued on next page*)

Continued

REAGENT or RESOURCE	SOURCE	IDENTIFIER
*In Vivo*MAb anti-mouse IFNAR-1	Bio X Cell	Cat#BE0241; RRID: N/A
*In Vivo*MAb anti-mouse CCL2 (MCP-1)	Bio X Cell	Cat#BE0185; RRID: N/A
Bacterial and virus strains		
CVB3	ATCC	Cat#VR-300
HCoV-OC43	ATCC	Cat#VR-1558
Chemicals, peptides, and recombinant proteins		
RPMI Medium 1640 (1X)	Gibco	Cat#11875-093
RPMI Medium 1640 D-Glucose (–)	Gibco	Cat#11879-020
Fetal Bovine serum (FBS)	Gibco	Cat#12483-020
HEPES (1M) pH 7.5	Gibco	Cat#15630-080
2-mercaptoethanol (1000X)	Gibco	Cat#21985-023
N2-supplement (100X)	Thermo Fisher	Cat#17502-048
B-27 supplement (50X), serum free	Thermo Fisher	Cat#17504044
Cyclosporin A (CsA)	Sigma-Aldrich	Cat#SML1018
Heparin-Binding EGF-Like Growth Factor	Sigma-Aldrich	Cat#E4643
LFM-A13	Sigma-Aldrich	Cat#435300
2′,3′-Dideoxycytidine (ddC)	Sigma-Aldrich	Cat#D5782
Corn oil	Sigma-Aldrich	Cat#C8267
Tween-80	Sigma-Aldrich	Cat#P4780
Dimethyl sulfoxide	Sigma-Aldrich	Cat#D8418
Dexamethasone	Sigma-Aldrich	Cat#D4902
Carbenoxolone disodium salt	Sigma-Aldrich	Cat#C4790
Brefeldin A	Sigma-Aldrich	Cat#B5936
Probenecid	Sigma-Aldrich	Cat#P3000000
DMEM	Sigma-Aldrich	Cat#D6429
DMEM Ham's:F12 Mixture	Sigma-Aldrich	Cat#51445C
Dulbecco's PBS	Sigma-Aldrich	Cat#D8662
Penicillin-Streptomycin	Sigma-Aldrich	Cat#P4333
Sodium pyruvate solution	Sigma-Aldrich	Cat#S8636
Hematoxylin solution Gill No.2	Sigma-Aldrich	Cat#GHS232
Herring testes (HT)-DNA	Sigma-Aldrich	Cat#D6898
Digitonin	Sigma-Aldrich	Cat#D141
Tunicamycin	Abcam	Cat#ab120296
RNase H	NEB	Cat#0297S
DNase I	NEB	Cat#M0303S
IFN-β-human recombinant proteins	Bio Basic Canada	Cat#RC217-16
Image-iT FX Signal Enhancer	Invitrogen	Cat#I36933
UltraPure™ Ethidium Bromide	Invitrogen	Cat#15585011
Lipofectamine 2000	Invitrogen	Cat#11668027
Lipofectamine RNAiMAX	Invitrogen	Cat#13778075
Normocin™	Invivogen	Cat#ant-nr-1
High molecular weight poly(I:C)	Invivogen	Cat#tlrl-pic
Protease inhibitor cocktail tablets	Roche	Cat#05892791001
DNAfectin™ Plus	ABM Canada	Cat#G2500
*Trans*IT-X2 Dynamic Delivery System	Mirus Bio	Cat#MIR 6004

(*Continued on next page*)

Continued

REAGENT or RESOURCE	SOURCE	IDENTIFIER
TNFR1 Blocking Peptide	Fitzgerald	Cat#33R-10641
RU.521	Cayman Chemical	Cat#31765
C-176	Cayman Chemical	Cat#25859
H-151	Cayman Chemical	Cat#25857
Fluo-cGAMP	BIOLOG Life Science Institute	Cat#C195-001
Protein G-Sepharose™ 4 Fast Flow	GE Healthcare Biosciences	Cat#17-0618
Critical commercial assays		
CyQuant™ LDH Cytotoxicity kit	Thermo Fisher	Cat#C20301
POWER SYBR® Green RNA-to-C_T™ kit	Thermo Fisher	Cat#4389986
ATP assay kit	Sigma-Aldrich	Cat#MAK190
MMP-assay kit	Sigma-Aldrich	Cat# MAK147-1KT
Universal Mycoplasma detection kit	ATCC	Cat#30-1012K
QIAGEN Plasmid Plus kit	QIAGEN	Cat#12941
RNeasy Mini-extraction kit	QIAGEN	Cat#74104
QIAmp DNA Mini Kit	QIAGEN	Cat#51304
Mouse ChAT ELISA Kit	Antibodies.com	Cat#A77879
QuicKey Mouse IgG ELISA Kit	Elabscience	Cat#E-TSEL-M0003
Mouse IgM ELISA Kit	Elabscience	Cat#E-EL-M3036
Mouse ANA (Anti-Nuclear Antibody) ELISA	MyBioSource	Cat#MBS261480
2′3′-cGAMP ELISA Kit	Cayman Chemical	Cat#501700
VeriKine mouse IFN Beta ELISA Kit, High Sensitivity	PBL Assay Science	Cat#42410-1
Deposited data		
RAW and analyzed data	This paper	GEO: GSE167974
Experimental models: Cell lines		
HeLa	ATCC	Cat#CCL-2.2; RRID: CVCL_0030
U2-OS	ATCC	Cat#HTB-96; RRID: CVCL_0042
HEK293T	ATCC	Cat#CRL-3216; RRID: CVCL_0063
THP-1	ATCC	Cat#TIB-202; RRID: CVCL_0006
RAW264.7	ATCC	Cat#TIB-71; RRID: CVCL_0493
SH-SY5Y	ATCC	Cat#CRL-2266; RRID: CVCL_0019
Neuro2a	ATCC	Cat#CCL-131; RRID: CVCL_0470
SIM-A9	ATCC	Cat#CRL-3265; RRID: CVCL_5I31
HASTR/ci35	From Dr. Tomomi Furihata (TUPLS, Japan)	Cat#N/A; RRID: CVCL_4U69; (Furihata et al., 2016; Kitamura et al., 2018)
C20	From Dr. David Alvarez-Carbonell (CWRU, USA)	Cat#N/A; RRID: N/A; (Garcia-Mesa et al., 2017)
NSC-34	From Dr. Neil R. Cashman (UBC, Canada)	Cat#N/A; RRID: CVCL_D356; (Cashman et al., 1992)
MO3.13	From Dr. Neil R. Cashman (UBC, Canada)	Cat#N/A; RRID: CVCL_D357; (McLaurin et al., 1995)
Experimental models: Organisms/strains		
Wild-type C57BL/6J background mice	The Jackson Laboratory	Cat#000664
B6.Cg-Tg (SOD1*G85R)148Dwc/J mice	The Jackson Laboratory	Cat#008248
B6.Cg-Tg(SOD1*G93A)1Gur/J mice	The Jackson Laboratory	Cat#004435

(*Continued on next page*)

Continued

REAGENT or RESOURCE	SOURCE	IDENTIFIER
B6.Cg-Tmem173tm1.2Camb/J mice	The Jackson Laboratory	Cat#025805
Oligonucleotides		
HCoV-OC43 Nucleocapsid (*N*): **F:** CGATG AGGCTATTCCGACTAGGT **R:** CCTTCCTGAGCCTTCAATATAGTAACC	Integrated DNA Technologies (IDT)	(Hammitt et al., 2011)
CVB3 *2A* gene: **F:** GCTTTGCAGACATCCGTGATC **R:** CAAGCTGTGTTCCACATAGTCCTTCA	Integrated DNA Technologies (IDT)	N/A
CVB3 *VP1* gene: **F:** ACATGGTGCGAAGAGTCTATTGAG **R:** TGCTCCGCAGTTAGGATTAGC	Integrated DNA Technologies (IDT)	N/A
Murine *IFNA4* gene: F: CTGCTACTTGGAATGCAACTC **R:** CAGTCTTGCCAGCAAGTTGG	Integrated DNA Technologies (IDT)	(Mattei et al., 2013)
Murine *IFNB1* gene: F: GCCTTTGCCATCCAAGAGATGC **R:** ACACTGTCTGCTGGTGGAGTTC Human *IFNB1* gene: F: CAACTTGCTTGGATTCCTACAAAG **R:** TATTCAAGCC TCCCATTCAATTG	Integrated DNA Technologies (IDT)	N/A
Murine *RSAD2* gene: F: TGGGGATGCTGGTGCCCACT **R:** ACCCCGGACCTGTGGCTGTT Human *RSAD2* gene: F: TTGGACATTCTCGCTATCTCCT **R:** AGTGCTTTGAT CTGTTCCGTC	Integrated DNA Technologies (IDT)	N/A
Murine *ISG15* gene: F: CAAGCAGCCAGAAGCAGACT **R:** CCCAGCATCTTCACCTTTAGG Human *ISG15* gene: **F:** CGCAGATCACCCAGAAGATCG **R:** TTCGTCGCAT TTGTCCACCA	Integrated DNA Technologies (IDT)	N/A
Murine *TNF* gene: F: GTCCCCAAAGGGATGAGAAGTT R: GTTTGCTACGACGTGGGCTACA Human *TNF* gene: **F:** CCTCTCTCTAATCAGCCCTCTG **R:** GAGGACCTGG GAGTAGATGAG	Integrated DNA Technologies (IDT)	N/A
Murine *CXCL10* gene: **F:** GCTGGGATTCACCTCAAGAA **R:** CTTGGGGACACCTTTTAGCA Human *CXCL10* gene: **F:** GTGGCATTCAAGGAGTACCTC **R:** TGATGGCCTTC GATTCTGGATT	Integrated DNA Technologies (IDT)	N/A
Human *CCL3* gene: **F:** ATGCAGGTCTCCACTGCTGCCCTT **R:** GCACTCAGCTCCAGGTCGCTGACAT	Integrated DNA Technologies (IDT)	(Chui and Dorovini-Zis, 2010)
Murine *CCL5* gene: **F:** GCTGCTTTGCCTACCTCTCC **R:** TCGAGTGACAAACACGACTGC	Integrated DNA Technologies (IDT)	N/A
Murine *IL-6* gene: **F:** ACAACCACGGCCTTCCCTAC **R:**TCTCATTTCCACGATTTCCCAG Human *IL-6* gene: **F:** ACTCACCTCTTCAGAACGAATTG **R:** CCATCTTT GGAAGGTTCAGGTTG	Integrated DNA Technologies (IDT)	N/A
Murine *IL-1B* gene:**F:** GCAACTGTTCCTGAACTCAACT **R:** ATCTTTTGGGGTCCGTCAACT Human *IL-1B* gene: **F:** CCACAGACCTTCCAGGAGAATG **R:** GTGCAGTTC AGTGATCGTACAGG	Integrated DNA Technologies (IDT)	N/A
Human *NOS2* gene: F: AGGGACAAGCCTACCCCTC **R:** CTCATCTCCCGTCAGTTGGT	Integrated DNA Technologies (IDT)	N/A
Human *IRF7* gene: F: GCTGGACGTGACCATCATGTA **R:** GGGCCGTATAGGAACGTGC	Integrated DNA Technologies (IDT)	N/A
Human *TNFAIP3* gene: F: TTGTCCTCAGTTTCGGGAGAT R: ACTTCTCGACACCAGTTGAGTT	Integrated DNA Technologies (IDT)	N/A

(*Continued on next page*)

Continued

REAGENT or RESOURCE	SOURCE	IDENTIFIER
Murine *AXL* gene: **F:** ATGGCCGACATTGCCAGTG **R:** CGGTAGTAATCCCCGTTGTAGA	Integrated DNA Technologies (IDT)	(Zou et al., 2020)
Murine *B2M* gene: **F:** ACAGTTCCACCCGCCTCACATT **R:** TAGAAAGACCAGTCCTTGCTGAAG	Integrated DNA Technologies (IDT)	N/A
Murine *AIF1* gene: **F:** TCTGCCGTCCAAACTTGAAGCC **R:** CTCTTCAGCTCTAGGTGGGTCT	Integrated DNA Technologies (IDT)	N/A
Human *IBA1* gene: **F:** CCCTCCAAACTGGAAGGCTTCA **R:** CTTTAGCTCTAGGTGAGTCTTGG	Integrated DNA Technologies (IDT)	N/A
Human *CD11B* gene: **F:** GGAACGCCATTGTCTGCTTTCG **R:** ATGCTGAGGTCATCCTGGCAGA	Integrated DNA Technologies (IDT)	N/A
Murine *SLC1A2* gene: **F:** ACAATATGCCCAAGCAGGTAGA **R:** CTTTGGCTCATCGGAGCTGA	Integrated DNA Technologies (IDT)	N/A
Murine *GFAP* gene: **F:** CGGAGACGCATCACCTCTG **R:** AGGGAGTGGAGGAGTCATTCG	Integrated DNA Technologies (IDT)	N/A
Murine *FGFR3* gene: **F:** GGAGGACGTGGCTGAAGAC **R:** GGAGCTTGATGCCCCCAAT	Integrated DNA Technologies (IDT)	N/A
Murine *AQP4* gene: **F:** CTTTCTGGAAGGCAGTCTCAG **R:** CCACACCGAGCAAAACAAAGAT	Integrated DNA Technologies (IDT)	N/A
Murine *GJB6* gene: **F:** ACCAGCATAGGGAAGGTGTG **R:** TGCAGAGTGTTGCAGACAAAG	Integrated DNA Technologies (IDT)	N/A
Murine *GJC2* gene: **F:** TCCACAATCATTCCACCTTCG **R:** CAGAAGCGCACATGAGACAG	Integrated DNA Technologies (IDT)	N/A
Murine *SOX10* gene: **F:** ACACCTTGGGACACGGTTTTC **R:** TAGGTCTTGTTCCTCGGCCAT	Integrated DNA Technologies (IDT)	N/A
Murine *SIGLEC4A* gene: **F:** CTGCCGCTGTTTTGGATAATGA **R:** CATCGGGGAAGTCGAAACGG	Integrated DNA Technologies (IDT)	N/A
Murine *MOG* gene: **F:** 'AGCTGCTTCCTCTCCCTTCTC **R:** ACTAAAGCCCGGATGGGATAC	Integrated DNA Technologies (IDT)	N/A
Murine *MBP* gene: **F:** GGCGGTGACAGACTCCAAG **R:** GAAGCTCGTCGGACTCTGAG	Integrated DNA Technologies (IDT)	N/A
Murine *HB9/MNX1* gene: **F:** CAGCACCTTCCAACTGGACCAG **R:** TTCGGCACTTCCCCAAGAGGTT	Integrated DNA Technologies (IDT)	N/A
Murine *ISL1* gene: **F:** GGTCTCTGGAACATCCCACATTGT **R:** CTGTTCCTACTCCCCATTCACT	Integrated DNA Technologies (IDT)	N/A
Murine *CHAT* gene: **F:** GCTTGAATGGAGCGAATCGTTGG **R:** CACCAGGACGATGCCATCAAAAG	Integrated DNA Technologies (IDT)	N/A
Murine *ACTB* gene: **F:** CATTGCTGACAGGATGCAGAAGG **R:** TGCTGGAAGGTGGACAGTGAGG Human *ACTB* gene: **F:** ACTGGAACGGTGAAGGTGAC **R:** GTGGACTTGGGA GAGGACTG	Integrated DNA Technologies (IDT)	N/A
MT-DNA *D-LOOP*: **F:** AATCTACCATCCTCCGTGAAACC **R:** TCAGTTTAGCTACCCCCAAGTTTAA	Integrated DNA Technologies (IDT)	N/A
MT-DNA *MT-CO1*: **F:** GACGTAGACACACGAGCATATTTCA **R:** AGGACATAGTGGAAGTGAGCTACAAC	Integrated DNA Technologies (IDT)	N/A
MT-DNA *MT-ND1*: **F:** CCACCTCTAGCCTAGCCGTTTA **R:** GGGTCATGATGGCAGGAGTAAT	Integrated DNA Technologies (IDT)	N/A
MT-DNA *MT-ATP6*: **F:** TAGCCATACACAACACTAAA GGACGA **R:** GGGCATTTTTAATCTTAGAGCGAAA	Integrated DNA Technologies (IDT)	N/A

(*Continued on next page*)

Continued

REAGENT or RESOURCE	SOURCE	IDENTIFIER
Nuclear *TERT* gene: **F**: CTAGCTCATGTGTCAAGACCC TCTT **R**: GCCAGCACGTTTCTCTCGTT	Integrated DNA Technologies (IDT)	N/A
RIG-I/DDX58 sgRNA (Human): 5′-GGATTAT ATCCGGAAGACCC-3′	Applied Biological Materials Inc.	N/A
MDA5/IFIH1 sgRNA (Human): 5′-CGAATTCC CGAGTCCAACCA-3′	Applied Biological Materials Inc.	(Ng et al., 2020)
MAVS sgRNA (Human): 5′-ATTGCGGCAGAT ATACTTAT-3′	Applied Biological Materials Inc.	N/A
GJA1 (CX43) sgRNA (Human): 5′-CTTGTCAA GGAGTTTGCCTA-3′	Applied Biological Materials Inc.	N/A
GJC1 (CX45) sgRNA (Human): 5′-ATCGTCCTT ACAGCTGTAGG-3′	Applied Biological Materials Inc.	N/A
GJD2 (CX36) sgRNA (Human): 5′-AGCACTCCA CTATGATCGGG-3′	Applied Biological Materials Inc.	N/A
PANX1 sgRNA (Human): 5′-AATCGAGATCTC CTGCGCGA-3′	Applied Biological Materials Inc.	N/A
TBK1 sgRNA (Human): 5′-AGAGCACTTCTAA TCATCTG-3′	Applied Biological Materials Inc.	N/A
IRF3 sgRNA (Human): 5′-TTGGAAGCACGG CCTACGGC-3′	Applied Biological Materials Inc.	N/A
TICAM1/TRIF sgRNA (Human): 5′-GTAGGCC ACGTCCCGCAGCG-3′	Applied Biological Materials Inc.	N/A
cGAS/MAB21L3 sgRNA (Human): 5′-ATGGC CTTTCCGTGCCA-3′	Applied Biological Materials Inc.	N/A
STING/TMEM173 sgRNA (Human): 5′-ACGGG ATGGATGGATGC-3′	Applied Biological Materials Inc.	N/A
STAT1 sgRNA (Human): 5′-TCCCATTACAGG CTCAGTCG-3′	Applied Biological Materials Inc.	N/A
TFAM sgRNA (Human): 5′-GCGTTTCTCCG AAGCATGTG-3′	Applied Biological Materials Inc.	N/A
DDX41 sgRNA (Human): 5′-AAGAGCGACAT GAGCGCGTG-3′	Applied Biological Materials Inc.	N/A
siRNAs targeting human *PPID* gene: ID: s10913, s10914, and s10915	Thermo Fisher	Cat#4390824
siRNAs targeting human *ZBP1* gene: ID: s37484, and s37485	Thermo Fisher	Cat#4390420
siRNAs targeting human *IFI16* gene: ID: s7136, and s7137	Thermo Fisher	Cat#4392420
Recombinant DNA		
p125-Luciferase reporter (IFN-β)	From Dr. Takashi Fujita (Kyoto University, Japan)	(Yoneyama et al., 1998)
p55C1B-Luciferase reporter (IRF3)	From Dr. Takashi Fujita (Kyoto University, Japan)	(Narita et al., 2014)
p55A2-Luciferase reporter (NF-κB)	From Dr. Takashi Fujita (Kyoto University, Japan)	(Narita et al., 2014)
pEF-Tak-Flag-MAVS	From Dr. Takashi Fujita (Kyoto University, Japan)	(Onoguchi et al., 2010)

(*Continued on next page*)

Continued

REAGENT or RESOURCE	SOURCE	IDENTIFIER
pEF-Flag-IRF3 5D	From Dr. Takashi Fujita (Kyoto University, Japan)	(Mori et al., 2004)
pcDNA-Flag-cGAS WT, ΔcGAMP, ΔDNA, K394E, and Y215E.	From Dr. Nelson O. Gekara (Stockholm University, Sweden)	(Jiang et al., 2019)
pEGFP-SOD1-WT, G93A, and G85R	From Dr. Neil R. Cashman (UBC, Canada)	(Pokrishevsky et al., 2017)
pcDNA-Flag-SOD1-WT, A4V, G37R, H46R, E100G, G93A, G85R, V148G, V148I, and G127X	From Dr. Christine Vande Velde (Université deMontréal, Canada)	(Semmler et al., 2020)
pGL4.32 (luc2P/NF-κB-RE/Hygro)	Promega	Cat#E8491
pRL-TK *Renilla* Luciferase Control reporter vector	Promega	Cat#E2231
Software and algorithms		
Prism version 8.0	GraphPad	https://www.graphpad.com/
Microsoft Office Home and Student 2019	Microsoft Corporation	https://www.microsoft.com/microsoft-365
Adobe Illustrator 2020	Adobe Inc.	http://www.adobe.com

RESOURCE AVAILABILITY

Lead contact

Further information and reasonable requests for resources and reagents should be directed to and will be fulfilled by the Lead Contact, Chen Seng Ng (chenseng.ng@xmu.edu.my).

Materials availability

This study did not generate new unique reagents.

Data and code availability

- NanoString gene expression profiling data that support the findings of this study have been deposited in the Gene Expression Omnibus (GEO) and are publicly available as of the date of publication. Accession numbers are listed in the Key resources table.
- This paper does not report original code.
- Any additional information required to reanalyze the data reported in this paper is available from the lead contact upon request.

EXPERIMENTAL MODEL AND SUBJECT DETAILS

Animals and experimental procedures

WT C57BL/6J (#000664), transgenic SOD1-G85R, and transgenic SOD1-G93A mice expressing high copy numbers of mutant SOD1 in a C57BL6/J background were all obtained from The Jackson Laboratory. *Sting*$^{-/-}$ (also known as*MPYS*$^{-/-}$ or *Tmem173*$^{-/-}$) and SOD1-G93A mice were crossed to generate *Sting*$^{-/-}$ G93A (G93A/*Sting*$^{-/-}$)-double-positive mice. These mice were housed under a 12-h/12-h light-dark cycle under controlled-temperature conditions (~20–22°C) and relative humidity (50%) with standard laboratory diet and water *ad libitum* unless otherwise indicated. Mice were bred and maintained in specific-pathogen free condition. Pregnant mice were individually housed in translucent plastic cages with corncob bedding. Animals were monitored weekly for changes in weight and behavior otherwise as further described in figure legends. The animals were euthanized with isoflurane at different time-points as indicated in the figure legends. Tissues including the brain, spinal cord, and other internal organs were harvested and either fixed with 4% paraformaldehyde or flash-frozen with liquid nitrogen then stored at −80°C. For the survival study, animals were inspected twice daily for health issues, and natural death was recorded for each animal. Moribund animals were euthanized, and every animal found dead was necropsied. For administration of neutralizing antibodies, and pharmacological inhibitors, WT, SOD1-G93A mice were injected with 500 μg of neutralizing antibodies (anti-IFNAR, and anti-MCP-1) or an equivalent

amount of vehicle (PBS) by intraperitoneal injection two-times per week for the first 4-weeks, three-days apart for the second injection in each week, then once a week afterwards. As for inhibitors, 8-weeksold WT, and SOD1-G93A mice were injected with 500 μg of C-176, H-151, or RU.521 or an equivalent amount of vehicle (containing 90% corn oil+10% Tween80, v/v) intraperitoneally two-times per week for the first 4-weeks and three-days apart for the second injection in each week, then once a week thereafter. No adverse effects were detected in the mice during treatment. For all experiments, adequate measures were taken to minimize any discomfort or pain. The study was performed in compliance with the ethical standards of the IACC of UBC, as well as in accordance to Malaysian laws. Mice were sibling-matched between treatment groups, all WT and SOD1 (G85R and G93A) mutant mice used in experimentation were male mice, and 8-weeksold adult mice were used in most experimentation unless otherwise as indicated in respective figure legends.

METHOD DETAILS

Motor function test

Hindlimb-clasping test

In the hindlimb-clasping test, the mouse was gently lifted by the tail, grasped near its base, and the hindlimb position was observed for 10 s and scored as follows: if the hindlimbs were consistently splayed outward, away from the abdomen, displaying normal escape extension with no sign of limb clasping, it was assigned a score of 0; if one hindlimb was retracted toward the abdomen for 50% of the time suspended and showed a loss of mobility, it received a score of 1; if both hindlimbs were partially retracted toward the abdomen for 50% of the time suspended, and show loss of mobility, it received a score of 2; and if both hindlimbs were entirely retracted and touching the abdomen for 50% of the time while suspended, followed by loss of mobility, it received a score of 3. Finally, if both forelimbs and hindlimbs exhibited clasping and were crossed for 50% of the observation period, coupled with loss of mobility, it received a score of 4.

Grip-strength test

A digital grip strength meter (Columbus Instruments) was used to automatically measure maximal hindlimb muscle grip strength. Mice were held by their tail and lowered until their hindlimb grasped the standard pull-bar connected to the digital force gauge. The tail was lowered until the body was in line with the device, followed by gently pulling away the mice from the pull-bar with a smooth steady motion until both of their hindlimbs are released from the bar. The strength of the hindlimb grip was quantified in gram force. Each mouse was given five attempts and the average of the grip strength from these attempts are recorded.

Gait analysis

At the beginning of this test, the personnel responsible for testing and scoring were blinded to animal genotype or the experimental condition until gait analysis and scoring of papers has been completed for the entire study. The forepaws and hind paws were covered with two nontoxic, water-soluble color inks (green color for forepaws and red color for hind paws). Small amounts of sterilized sunflower seeds were placed in housing cages 2-days prior to testing to facilitate habituation. Mice were then allowed to walk along an 89.0-cm-long and 39.0-cm-wide runway with a goal chamber placed at the endpoint. On the day of testing, a small quantity of sunflower seeds was placed inside the goal chamber to encourage the mice to walk through without stopping. The runway was covered with sheets of white paper. After reaching the goal chamber, the mice were retrieved and gently the feet gently wiped with water-dampened Kimtech wipers. The footprints were analyzed manually at the indicated time-points after confirming the footprints were completely dry, and the stride length (defined as the distance between two sequential footprints created by the same foot) of the hindlimbs was quantified.

Cell lines, cell culture, and transfection conditions

Both HEK293T (ATCC® CRL-3216™) and HeLa cells (ATCC® CCL-2™) were maintained at 37°C and 5% CO_2 in Dulbecco's Modified Eagle Medium (DMEM, Sigma) supplemented with 10% fetal bovine serum (FBS, Gibco, Thermo Fisher), 1x Penicillin-Streptomycin (Pen-Strep, Sigma), and 100 μg/mL Normocin (Invivogen). THP-1 monocyte cells (ATCC® TIB-202™) were maintained at 37°C and 5% CO_2 in RPMI 1640 (Gibco) supplemented with 10% FBS, 1x Pen-Strep, 0.05 mM of β-mercaptoethanol, 10 mM HEPES, and 1 mM of sodium pyruvate. Immortalized human microglia (Clone#20, C20) were a kind gift from Dr. David Alvarez-Carbonell (Case Western Reserve University) (Garcia-Mesa et al., 2017). In brief, C20 were

maintained at 37°C and 5% CO_2 in DMEM/Nutrient Mixture F12 Ham with L-glutamine (F12:DMEM, Sigma) supplemented with 1x FBS, 1x Pen-Strep, 1.0 μM dexamethasone, and 100 μg/mL of normocin. Immortalized human astrocytes (HASTR/ci35) were cultured as previously described (Furihata et al., 2016). In brief, HASTR/ci35 were seeded in sterile culture dishes pre-coated with collagen I in the presence of DMEM media containing N2 supplement (1%), 10% FBS, penicillin-streptomycin, GlutaMax-I, and blasticidin (4.0 μg/mL) and incubated at 33°C with 5% CO_2. DNA-related materials were transfected using *Trans*IT-X2 transfection reagent according to manufacturer's protocol. RNA-related materials were transfected using RNAi-MAX according to the manufacturer's protocol. All tissue culture cells were tested for *Mycoplasma* and were confirmed to be negative using Mycoplasma detection kit. All the above experiments were performed in certified BSL-2 facilities.

Immunopanning of murine primary neuronal and non-neuronal cells and culture conditions

Microglia/macrophages, oligodendrocyte lineage cells, neurons and astrocytes were purified by immunopanning from the P10 mice cerebral cortex and cultured as previously described (Foo, 2013). In brief, mouse cortices were first enzymatically (papain) and then mechanically dissociated to generate a single-cell suspension that was incubated on multiple antigen-specific antibody plated immunopanning plates to isolate microglia (secondary antibody, Jackson ImmunoResearch and CD45 antibody), oligodendrocyte lineage cells (O4 antibody), neurons (L1 antibody), and astrocytes (ITGB5 antibody). Isolated microglia/macrophages were cultured in fresh DMEM/F1 media containing 10% FBS, 1% penicillin/streptomycin, 1% L-glutamine, and 1% sodium pyruvate (Sarkar et al., 2017). Isolated oligodendrocyte lineage cells were lysed for downstream analysis immediately after immunopanning. Isolated neurons were cultured in growth medium containing 50% DMEM and 50% neurobasal with 1 mM sodium pyruvate, 2 mM L-glutamine, 1% penicillin/streptomycin, 100 μg/mL human transferrin, 60 ng/mL progesterone, 16 μg/mL putrescine, 40 ng/mL sodium selenite, 40 ng/mL thyroxine, 30 ng/mL tri-idothyronine, and B27 Supplement (Dugas et al., 2008). Isolated astrocytes were cultured in growth medium containing 50% DMEM and 50% neurobasal with 1% penicillin/streptomycin, 1 mM sodium pyruvate, 292 μg/mL L-glutamine, 1x SATO and 5.0 μg/mL of *N*-acetyl cysteine. This medium was supplemented with the astrocyte-required survival factor HBEGF (Sigma-Aldrich) at 5 ng/mL (Foo, 2013).

Generation of CRISPR-Cas9-deficient cell lines

All CRISPR-Cas9 sgRNAs constructs used in this study were custom-made and synthesized through ABM. Constructs targeted isoform-2 of each respective protein in the human lineage. Sequences for sgRNAs are provided in the Key resources table. Cells of interest were seeded and house in 37°C with CO_2 for overnight. Cells were then transfected with CRISPR-Cas9 expressing sgRNA targeting gene of interest for 48 h. Cells were then trypsinized and replated at a density of 10 cells/mL in a 96-well tissue culture plate containing 100 μL media per well. The number of cells in the plate were assessed after 24 h. Wells with only one cell were marked. On day 5, wells that were marked at the initial assessment were re-evaluated. Only wells with one colony were considered monoclonal and were marked. After these wells were identified, colony numbers were verified every week until the well reached a high confluence. Single colonies/well were expanded by transferring to a 12-well tissue culture plate. Once the 12-well plate clones had expanded, they were passaged to a 6-well plate. Knockout efficiency was validated through immunoblotting using specific antibodies and functional analyses.

Mitochondria DNA subcellular fractionation, depletion, and membrane potential assay

Isolation and purification of cytoplasmic mitochondrial DNA was adopted and modified as previously described (West et al., 2015). In brief, C20 cells were lysed in digitonin lysis buffer (150 mM NaCl, 50 mM HEPES pH 7.4, 25 μg/mL digitonin, supplemented with protease and phosphatase inhibitors cocktail, Roche) and incubated on a rotator at 4°C for 15 min. Samples were then centrifuged at speed of 4226 rpm for 10 min at 4°C. Supernatants were then transferred to fresh tubes and centrifuged three times at 13,363 rpm for 20 min at 4°C. Supernatants were transferred to fresh tubes between centrifugation steps to finally yield cytosolic fractions. The cytosolic fraction was split into two tubes (one for total DNA extraction and one for immunoblot analysis). The remaining pellet from the first spin was resuspended in ice-cold PBS to wash away the digitonin buffer. Samples were then centrifuged at 4226 rpm for five min at 4°C. The wash solution was aspirated, and samples were resuspended in NP-40 lysis buffer (150 mM NaCl, 50 mM HEPES pH 7.4, 1% NP-40, protease, and phosphatase inhibitors) and incubated on ice for 30 min. Samples were centrifuged at 7,906 rpm for 10 min at 4°C to yield the crude mitochondria fraction for immunoblot analysis. The remaining pellet was resuspended in ice-cold PBS to remove away NP-40 buffer. Samples

were divided into two tubes (one for total DNA extraction and one for cellular lysates). One tube was centrifuged at 4,226 rpm for 5 min at 4°C. The wash solution was aspirated and samples were resuspended in RIPA lysis buffer to yield nuclear fraction for immunoblot analysis. The DNA was subsequently extracted from the appropriate cytosolic and nuclear fractions using the QIAmp DNA Mini Kit (QIAGEN). The concentration of cytosolic DNA was measured via NanoDrop, and 10.0 ng were used for RT-qPCR analysis of mitochondrial DNA using gene-specific primers. The sequence of primers specifically targeting mitochondria DNA are provided in the Key resources table. Nuclear gene *TERT* was quantified from the respective nuclear fraction for normalization. To deplete mitochondria DNA, cells of interest were cultured with or without ethidium bromide or ddC for 4 days (Hashiguchi and Zhang-Akiyama, 2009). On day 4, cells were washed with sterile 1x PBS and trypsinized before counting and seeding for subsequent experiments in the absence of EtBr/ddC. Cytoplasmic mitochondria DNA was fractionated as described above. For quantification of mitochondrial membrane potential (MMP, $\Delta\Psi$), the MMP assay kit was used according to manual's instructions.

ELISA, immunoblotting, and antibodies

For western blotting, cells were harvested in ice-cold Dulbecco's phosphate-buffered saline (DPBS) using a sterile cell scraper. Cells were pelleted down by centrifugation and lysed in Modified Oncogene Science Lysis Buffer (MOSLB) (50 mM Na Pyrophosphate, 50 mM NaF, 50 mM NaCl, 5 mM EDTA, 5 mM EGTA, 100 μM Na_3VO_4, 10 mM HEPES and 0.1% Triton X-100) containing protease inhibitor cocktail (Roche), followed by centrifugation at maximum speed for 15 min and ultracentrifugation at 100,000 rpm for 5 min. The protein concentration was measured using a Bradford assay (Bio-Rad). Whole cell extract was mixed with 1x sodium dodecyl sulfate (SDS) buffer, boiled at 100°C for 5 min before being immediately transferred on ice and incubated for 5 min. Sample volume corresponding to a protein amount of 50 μg was loaded into either 8%, 10% or 15% self-cast gel using standard SDS-polyacrylamide gel electrophoresis (PAGE) protocol before being transferred onto a nitrocellulose membrane (Bio-Rad). The membranes were blocked in 5% non-fat skim milk for 30 min at room temperature (RT), followed by incubation with primary antibody diluted in blocking buffer at 4°C overnight. Membranes were washed extensively with 1x TBST (mixture of Tris-buffered saline with 0.1% Tween20), followed by incubation with a conjugated secondary antibody for 1hat RT. After washing with 1x TBST, immunoreactive bands were visualized using alkaline phosphatase buffer containing 5′-bromo-4-chloro-3′-indolylphosphate (BCIP)-Nitro Blue Tetrazolium color development substrate. The list of primary antibodies used in this study are provided in the Key resources table. For the ELISA bioassay, all ELISA assays were performed using commercialized kit according to the manufacturer's instruction. The absorbance was calculated based on a standard curve after subtracting the background.

Immunoprecipitation

For immunoprecipitation, soluble lysate was pre-cleared with protein G-sepharose beads for 1hat 4°C, and then incubated with control anti-mouse IgG or anti-S9.6 antibody plus protein G-sepharose beads at 4°C for 12 h. Beads, together with lysates were washed thrice with S9.6 immunoprecipitation buffer, thrice with S9.6 immunoprecipitation buffer containing 1 M NaCl, and thrice with S9.6 immunoprecipitation buffer, followed by elution in cytoplasmic lysis buffer containing RNase and DNase inhibitors.

Immunohistochemistry and histochemical staining

Paraffin-embedded sections (4.0 μm thick) were deparaffinized first through xylene and then with a gradually decreasing concentration of isopropanol (100%, 90% and 70%). Hematoxylin and eosin staining was performed to evaluate virus-induced brain damage. The sections were also subjected to immunohistochemical staining. Briefly, antigen retrieval was performed by heating the sections in citrate buffer pH 6.0 (Life Technologies Carlsbad, CA; 005000) for 25 minutes at 121°C. Slides then underwent peroxidase blocking using hydrogen peroxide (30 mg/mL), followed by washes with 1× TBS pH 7.6 (Tris-buffered saline, 0.05 M Tris, 0.155 M NaCl). After blocking, sections were incubated with primary antibodies overnight at 4°C. The MACH4 Universal HRP-Polymer Detection System (Biocare Medical, Pacheco CA; BRI4012H) was then used to detect the staining according to the manufacture's protocol. At the end of the procedure, all slides were also counterstained with hematoxylin solution Gill II (Sigma-Aldrich, GHS232).

Mouse brain tissues were immunoassayed using the follow primary antibodies diluted in TBS-PBS buffer (1% BSA, 1.5 M NaCl, 0.5 M pH 7.6): GFAP (1:200 dilution); Iba1 (1:200 dilution); NK1.1 (1:300 dilution); CD4 (1:500 dilution); CD8 (1:500 dilution), and CD19 (1:500 dilution). Images were taken using the Aperio

ScanScope AT (Digital slide scanner, Leica Biosystems Inc., Buffalo Grove, IL) or a Nikon Eclipse E600 microscope equipped with a SPOT Flex Model 15.2 64 Mp Shifting Pixel camera (Diagnostic Instrument Inc., Sterling Heights, MI).

Confocal microscopy imaging

For immunofluorescence staining, cells were washed in cold DPBS and fixed with 4% paraformaldehyde for 30 min at RT. After fixation, cells were permeabilized with 0.5% Triton X-100 in DPBS for 10 min, and blocked with Earle's balanced salt solution containing 0.1% Triton X-100, 5% bovine serum albumin (BSA), 5% goat serum, and 0.1% saponin for 1hat RT. Primary antibodies were incubated at 4°C overnight and secondary antibodies were incubated for 1hat RT. Cells were washed three times with PBS containing 0.1% Triton X-100 and incubated for 15 min with four drops of Image-IT Fx signal enhancer. Coverslips were washed three times with PBST (mixture of 1x phosphate-buffered saline with 0.1% Tween®20), followed by counterstaining with DAPI (4,6-diamidino-2-phenylindole, Vector Laboratories; H-1200). Images were taken using the Zeiss LSM 980 with Airyan scan 2. While some antibodies are like those described in immunoblotting section, other antibodies specifically used for immunofluorescence staining included anti-p65, anti-IRF3, and anti-DNA-RNA Hybrid, clone S9.6.

Crystal violet, cell viability and luciferase reporter assay

For the crystal violet staining, cell culture medium from mock and infected cells was aspirated before washing with sterile DPBS, followed by incubation with 0.5% crystal violet solution at RT for 30 min (on a shaking platform). Cells was then rinsed with tap water several times. Plates were then inverted and with mild tapping the residual water was removed. Plates were air-dried at RT. Finally, methanol was added into each well and incubated on a shaking platform at RT for 20 min, the optical density at 540 nm wavelength (OD_{540nm}) was measured. Lactate dehydrogenase (LDH) release assay were performed using the CyQUANT^{TM} LDH cytotoxicity assay kit (Thermo Fisher) according to manufacturer's protocol. The luciferase assay was performed with a dual luciferase reporter system (Promega) and pRL-TK (Promega) was used as the as the internal control.

RNA isolation and quantitative RT-PCR

RNA was harvested from cells using the RNeasy Mini extraction kit (Qiagen) according to the manufacturer's instructions. A total of 100 ng of purified RNA was used as a template for gene expression analysis using *POWER* SYBR Green RNA-to-C_T^{TM} One-Step kit (Thermo Fisher). All gene expression analyses were then processed using the $2^{-\Delta\Delta Ct}$ relative quantitative method and compared to control samples. Primers were all customized and purchased from Integrated DNA Technologies. The primer sequences for all RT-qPCR are provided in the Key resources table.

NanoString analysis

Total RNA was isolated from the brain and spinal cord of WT and G85R-mice, and 100 ng was used to determine the absolute levels of gene expression through an nCounter mouse neuroinflammation panel (~770 genes). Hybridization and nCounter were performed by the Molecular Genomics Core of Heart Lung Innovation research institute, UBC, according to the manufacturer's protocol (NanoString Technologies). In brief, reactions were hybridized for 20hat 65°C, after which the products were run on the nCounter preparation station for the removal of excess probes. Data were collected with the nCounter digital analyzer by counting individual barcodes. Data generated from the nCounter digital analyzer were examined using nSolver Analysis software 3.0 (NanoString Technologies). The data were normalized to the geometric means of spiked-in positive controls for assay efficiency and spiked-in negative controls to normalize background. The data were further normalized to the housekeeping genes *Gapdh*, *Hprt*, and *β-actin*, and reported as normalized RNA counts (means ± standard error of the mean [SEM]). For further analysis, differential expression of genes was performed using the Advanced Analysis module. For each gene, a single linear regression was fit using all selected covariates to predict expression. The output is shown with a non-adjusted p-value as well as Benjamini–Hochberg false discovery rate. Expression values within all heat-maps were converted either to Log-2 or Log-10 scale and presented as original normalized expression values.

Flow cytometry analysis

Trypsinized cells were maintained and stained in PBS containing 2 mM EDTA, 5% FBS. Flow cytometry was performed on FACSAria (BD Biosciences) and LSRFortessa (BD Biosciences) and was analyzed using

FlowJo software version 10 and FACS Calibur CellQuest software (BD Biosciences). Values were plotted using GraphPad Prism version 8.0.

QUANTIFICATION AND STATISTICAL ANALYSIS

Mice were randomized to groups and the analysis of mice and tissue samples was performed blinded to the treatment or the genetic background of the animals. Sample size (*N*) representing biological replicates can be found on the figure legends. No statistical methods were used to predetermine sample sizes or to test for a normal distribution. The numbers of biological replicates were chosen based on the nature of the experiments and published papers describing similar experiments. Quantification of immunohistochemistry images was performed using ImageJ (version 1.0) with the combination of Color Deconvolution Plugin (version 1.5) to generate optical density values based on the intensity of the staining as described (Xue et al., 2018). Statistical tests for each assay are indicated in the figure legends. Data are presented as means and error bars represent SEMs. No statistical method was used to determine whether the data met assumptions of the statistical approach. Prism version 8.0 (GraphPad) was used for all statistical analysis. *$p < 0.05$, **$p < 0.01$, ***$p < 0.001$ was considered statistically significant.